

**EXAMINING CONTROLS ON CHEMICAL
MASS TRANSPORT ACROSS THE
TAILINGS-WATER INTERFACE OF AN
OIL SANDS END PIT LAKE**

A Thesis Submitted to the College of
Graduate and Postdoctoral Studies in
Partial Fulfillment of the
Requirements for the Degree of
Master of Science in the Department of
Geological Sciences
University of Saskatchewan
Saskatoon

By
DANIEL JAMES FRANCIS

PERMISSION TO USE

In presenting this thesis in partial fulfillment of the requirement of a Postgraduate degree from the University of Saskatchewan, I agree that the Libraries of this University may make it freely available for inspection. I further agree that permission for copying of this thesis in any manner, in whole or in part, for scholarly purposes may be granted by the professor or professors who supervised my thesis work or, in their absence, by the Head of the Department of Geological Sciences or the Dean of the College of Graduate and Postdoctoral Studies. It is understood that any copying, publication or use of this thesis or parts thereof for financial gain shall not be allowed without my written permission. It is also understood that due recognition shall be given to me and to the University of Saskatchewan in any scholarly use which may be made of any material in my thesis.

Requests for permission to copy or to make other uses of materials in this thesis in whole or part should be addressed to:

Head

Department of Geological Sciences
University of Saskatchewan
114 Geology Building, 114 Science Place
Saskatoon, Saskatchewan S7N 5E2
Canada

Dean

College of Graduate and Postdoctoral Studies
University of Saskatchewan
116 Thorvaldson Building, 110 Science Place
Saskatoon, Saskatchewan S7N 5C9
Canada

ABSTRACT

End pit lakes (EPLs) are an important remediation technology for fluid fine tailings (FFT) generated during oil sands mining and upgrading. EPLs are created by pumping FFT into a mined-out pit and then capping them with water. The first commercial scale EPL is Base Mine Lake (BML) at Syncrude Canada Ltd.'s Mildred Lake Mine in the Athabasca oil sands region in northern Alberta, Canada. The long-term evolution of mass loading in BML has implications for the viability of EPLs as a remediation technology in the Alberta oil sands. Internal mass loading from FFT to the overlying water cap may impact water quality in EPLs. Mass loading in BML is driven primarily by advective-dispersive transport from FFT settlement. However, the influence of mixing on the upper FFT by methane (CH_4) ebullition has not been explored. This research examines the potential for CH_4 ebullition in BML and the influence it may have on mass transport. FFT porewater samples were taken from 0.5 m above the tailing-water interface (TWI) down to 40 m below the interface in 2016 and 2017. Sensors that record temperature and pressure were deployed in 2018 and 2019. Detailed FFT porewater chemistry analysis was integrated with published data to define the distribution of dissolved constituents within BML. Numerical modelling, noble gas analysis, and dissolved gas pressure analysis were used to determine the potential for CH_4 ebullition within FFT. Transport modelling that included CH_4 ebullition was carried out to simulate observed chemical depth profiles. The degree and distribution of CH_4 saturation vary spatially throughout FFT in BML. Dissolved CH_4 concentrations were at or near saturation between 1.5 to 3 m below the TWI throughout BML. Annual seasonal cycles and continually settling FFT both influence CH_4 solubility. Advective-dispersive mass transport modelling with mixing by ebullition found that different locations required different amounts of mixing to simulate geochemical tracer depth profiles. Typically, locations with greater ebullition potential and settlement required more mixing by ebullition. Dissolved CH_4 transport modelling showed that anaerobic oxidation limited flux rates from the FFT into the water cap. The results of this study refined the conceptual model for internal mass loading as well as developed a model for parameters that can influence CH_4 ebullition in an oil sands EPL.

ACKNOWLEDGEMENTS

I would like to acknowledge and thank my supervisors Dr. Matthew Lindsay and Dr. S. Lee Barbour for their invaluable guidance and support throughout this thesis. Thank you for the patience, especially through the accelerated timeline in the writing process and guidance in becoming a better writer. Thank you to my committee member Dr. Jim Hendry, and my external examiner Dr. Colin Whitfield, for their time in reviewing my thesis and their constructive feedback.

A massive thank you to my lab manager Noel Galuschik for her support and patience as I broke, borrowed (sometimes permanently), lost and then found numerous different tools, sensors and materials for all the field work. A thank you to my field assistant/manager Mattea Cowell for taking significant time out of her own research to assist in the field.

My gratitude to the entire Lindsay lab group, to Carlo Cilia for helping me get started in Saskatoon, to Sarah Rudderham, and Jared Robertson for being there to talk to about anything BML related. I would like to thank the support from the Lindsay Lab Duck hunting committee: James Schulte, Lawrence Swerhone, and Colton Vessey.

Thank you to the Syncrude Reclamation and Closure Research team, especially Wendy Kline, Mohammed Salem, Jessica Piercey and Christopher Beierling for all the support and accommodation on frequently short notice. My thank you to Rocky Johnson for being a fantastic boat operator and making field work a pleasure. My gratitude to Conetec for carrying out the FFT sample collection and their support through sample collection in 2017.

A heartfelt thanks to my family for their support, I couldn't have made it this far without you. To Mookie, my cat, you are the most effective alarm clock I ever had. Finally, Courtney, thank you for being there for me, your love and support mean the world to me.

TABLE OF CONTENTS

PERMISSION TO USE.....	ii
ABSTRACT.....	iii
ACKNOWLEDGEMENTS	iv
TABLE OF CONTENTS	v
LIST OF TABLES	vii
LIST OF FIGURES	viii
LIST OF ABBREVIATIONS	xi
CHAPTER 1: INTRODUCTION.....	1
CHAPTER 2: RESEARCH OBJECTIVES.....	4
CHAPTER 3: LITERATURE REVIEW	5
3.1 Alberta Oil Sands	5
3.2 Fluid Fine Tailings	6
3.3 Reclamation Strategies	6
3.3.1. End Pit Lakes.....	7
3.4 Internal Mass loading	8
3.5 Methane Dynamics	10
3.6 Ebullition Assessment Approaches	12
CHAPTER 4: METHODOLOGY	14
4.1 Study Site.....	15
4.2 Data Collection.....	18
4.2.1. Temperature and pressure.....	19
4.2.2. Porewater chemistry.....	20
4.2.3. Solids Content.....	22
4.2.4. Settlement rates.....	23
4.3 Methane Ebullition Potential.....	24
4.4 Transport Modelling.....	25
CHAPTER 5: RESULTS	29
5.1 Volumetric Water Content	29

5.2	Settlement	30
5.3	Temperature.....	31
5.4	Pressure.....	33
5.5	Porewater Chemistry	35
5.5.1.	<i>Dissolved Cl⁻ and B</i>	36
5.5.2.	<i>Stable Isotope of Water</i>	38
5.5.3.	<i>Dissolved Gases</i>	40
CHAPTER 6: ANALYSIS AND DISCUSSION		43
6.1	Methane Distribution.....	43
6.1.1.	<i>Dissolved Gas Saturation</i>	44
6.1.2.	<i>Methane Ebullition</i>	47
6.1.3.	<i>Long-Term Trends</i>	49
6.2	Transport of Conservative Constituents	50
6.3	Transport of Dissolved CH ₄	58
6.4	Revised Conceptual Model.....	63
CHAPTER 7: CONCLUSIONS		67
CHAPTER 8: RECOMMENDATIONS.....		69
REFERENCES.....		70
APPENDIX B: SENSOR DESIGN		93
APPENDIX C: TRANSPORT MODEL DATA.....		96

LIST OF TABLES

Table 4-1: Summary of the different parameters studied and reviewed in this study.....	14
Table 4-2: Model parameters used, and the enhanced diffusion coefficients applied to the model to simulate ebullition.....	27
Table 6-1: RMSE for each modelled profile with different simulated ebullition rates of Cl ⁻ (top) and Boron (bottom). The smaller the number the better the fit of the data.	54
Table 6-2: RMSE for each CH _{4(aq)} modelled profile with different simulated CH _{4(aq)} consumption rates. The smaller the number the better the fit of the data.....	59

LIST OF FIGURES

Figure 1-1: Initial conceptual model of processes and parameters in an oil sands EPL that affect internal mass loading from FFT to the overlying water cap (after Dompierre 2017).....	3
Figure 4-1: Satellite image of the Syncrude Canada Ltd. Mildred Lake Mine. The Athabasca River flows along the NE corner of the image.	16
Figure 4-2: FFT elevation map showing TWI elevation (masl) in 2012 after commissioning and in October 2017. Modified from Barr (2018).	17
Figure 4-3: Schematic diagram of pressure, temperature and passive gas samplers deployed in BML summer 2018 (after Dompierre et al., 2014).....	18
Figure 4-4: Fixed interval sample, (left) and fluid sampler (right; Rudderham 2019).....	Error!
Bookmark not defined.	
Figure 4-5: Results of sensitivity analysis for the three controlling parameters on CH ₄ solubility for the range of conditions observed at BML.	25
Figure 5-1: Volumetric water content profiles for 2014 and 2017 extending to 45 m (left) and 15 m (right) below the TWI.	30
Figure 5-2: Measured TWI elevations compared to modelled elevations based large strain consolidation (LSC) simulations by Carrier et al., 2007.	31
Figure 5-3: Averaged monthly temperature profiles from BML in 2018 (left) and 2019 (center), and whole lake average annual temperature cycle (right). 2013–2014 temperature data comes from Dompierre et al. (2016). The red dashed line represents the TWI.....	33
Figure 5-4: Results of summer 2018 fluid and total dissolved gas pressure campaign plotted as the difference between P _{TDG} and P _{fluid}	35

Figure 5-5: Depth profiles of Cl^- at each sampling platform extending down to 5 m. The dashed line represents TWI.....	37
Figure 5-6: Depth profiles of Boron at each sampling platform. The horizontal dashed line represents TWI.....	38
Figure 5-7: Depth profiles of $\delta^2\text{H}$ (top) and $\delta^{18}\text{O}$ (bottom) at each sampling platform normalized to the TWI. The horizontal dashed line represents the TWI.....	39
Figure 5-8: Depth profiles of $\text{CH}_{4(\text{aq})}$ (top) and $\text{CO}_{2(\text{aq})}$ (bottom) depth profiles at each sampling platform relative to the TWI. The horizontal dashed line represents the TWI.	41
Figure 5-9: Depth profiles of selected noble gas ratios. The horizontal dashed line represents the TWI.	42
Figure 6-1: Dissolved methane solubility saturation limits for average summer and winter conditions in 2014 and 2018 at BML.	45
Figure 6-2: Dissolved CH_4 concentrations plotted as a fraction of modelled solubility by sampling location and year. Horizontal dashed line represents the TWI.	46
Figure 6-3: Comparison of 2015 BML noble gas ratios with data from Jones et al., (2014).	48
Figure 6-4: Plot of calculated upwards advection based on measured TWI elevations (points) and modelled elevations (lines).	51
Figure 6-5: Plot of BML surface water elevation over time. The grey dashed lines indicate sampling times at P2NE.....	53
Figure 6-6: Mass transport model profiles and observed concentrations for Cl^- depth profiles by year and location extending to 5 m below the TWI.....	55
Figure 6-7: Mass transport model profiles and observed concentrations for boron depth profiles by year and location extending to 5 m below the TWI.....	56

Figure 6-8: Timeline of $\text{Cl}^-_{(\text{aq})}$ mass flux rate from the FFT into the water cap for the differing amounts of ebullition simulated in the transport models over the modelled period. 57

Figure 6-9: Mass transport model profiles for CH_4 depth profiles by year and location extending to 5 m below the TWI. 61

Figure 6-10: Conservative and consumptive $\text{CH}_{4(\text{aq})}$ mass flux rate over the modelled period at the TWI. The consumptive model flux shown uses a consumption rate over 1.0 m at both P1C and P3SW and 1.5 m at P2NE. 62

Figure 6-11: General conceptual model showing the main processes that affect mass transport within BML. 64

Figure 6-12: Conceptual model of the parameters affecting ebullition potential in BML. Modified from Harrison et al. (2017). 65

LIST OF ABBREVIATIONS

AOSR	Athabasca Oil Sands Region
BCR	Beaver Creek Reservoir
BML	Base Mine Lake
EPL	End Pit Lake
FFT	Fluid Fine Tailings
FTT	Froth Treatment Tailings
FIS	Fluid Interval Sampler
FS	Fluid Sampler
HDPE	High Density Polyethylene
MLSB	Mildred Lake Settling Basin
NG	Noble Gas
OCC	Oxygen Consuming Constituent
OSPW	Oil Sands Process Affected Water
P1C	Platform 1 Center
P2NE	Platform 2 Northeast
P3SW	Platform 3 Southwest
P_{fluid}	Total Fluid Pressure
P_{TDG}	Total Dissolved Gas Pressure
RMSE	Root Mean Square Error
SWIP	Southwest In-Pit
TWI	Tailings Water Interface
WCTT	Water Capped Tailings Technology
WIP	West In-Pit

CHAPTER 1: INTRODUCTION

Bitumen deposits in the Alberta oil sands of northern Alberta, Canada, host the third largest hydrocarbon reservoir in the world with proven reserves of 166 billion barrels (Alberta Government, 2018). In the Athabasca oil sands region (AOSR), these deposits are hosted in the poorly consolidated cretaceous sands of the Wabiskaw-McMurray member of the Mannville group (Hein and Cotterill, 2006; Gibson et al., 2013). Ore is extracted by open-pit mining or using in-situ methods (Kaperski and Mikula, 2011; Alberta Government, 2018). In the Fort McMurray/Fort Mackay area, the oil sands deposits are shallow enough to facilitate extraction via open-pit mining (Kaperski and Mikula, 2011).

Surface mining operations generate three principal tailings streams: (1) coarse (sand) tailings; (2) fluid fine tailings (FFT); and (3) froth treatment tailings (FTT). While both coarse tailings and FTT present challenges for reclamation, FFT are particularly problematic due to their high salinity, clay and water content, and low settlement and dewatering rates (Kaperski and Mikula 2011). These tailings add considerable complexity to remediation efforts, which much address the over 1.2 billion m³ of fine tailings currently stored in tailings ponds across the AOSR plus any future fine tailings production (Alberta Government 2019a)

Broadly, remediation strategies are centered around either aquatic or terrestrial technologies where the tailings are either water covered or form part of a soil covered landscape (Kaperski and Mikula, 2011). One aquatic reclamation technology is end pit lakes (EPLs) where tailings are placed in mined-out pits and water capped (Kaperski and Mikula, 2011). End pit lakes may be referred to as water capped tailings technology (WCTT) in some documents and reports. Ultimately, the aim of EPLs is to become self-sustaining, healthy boreal aquatic ecosystems that are integrated into the surrounding watershed. Water flowing into EPLs may be released to the surrounding landscape and, potentially, to the Athabasca River (Dompierre et al., 2016). Therefore, the success of EPLs as a remediation strategy relies on surface water quality that meets yet to be defined criteria but broadly representative of a natural boreal water body. Initial EPL cap water chemistry is similar to oil sands process-affected water (OSPW). Cap water quality is expected to improve over time due to freshwater inputs and in situ biogeochemical processes

(Dompierre et al., 2016). However, the impact of internal mass loading from FFT to the water cap is not well constrained and could adversely impact and delay improvement in water quality (Dompierre and Barbour, 2016; Dompierre et al., 2017; Lawrence et al., 2016). Mass loading is expected to be driven primarily by advective dispersive transport due to tailings settlement. However, sediment mixing is also believed to impact internal mass loading. Potential mixing processes include periodic mixing by internal seiches or lake turnover and variably continuous mixing by methane ebullition (CH₄; Dompierre et al., 2017; Hurley, 2017). Biogenic *in situ* gas generation, particularly methanogenesis, and ebullition are widely reported in tailings deposits across the AOSR and is reported in studied EPLs (Lawrence et al., 2016; Stasik and Wendt-Pothoff 2016; Holowenko et al., 2000; Siddique et al., 2012). Ebullition may affect internal mass loading as well as resuspend sediment (Dompierre et al., 2017; Kavcar and Wright, 2011). FFT porewater contains elevated constituents of concern relative to the water cap and resembles OSPW in chemistry (Dompierre et al., 2016; Risacher et al., 2018)

Developing an understanding of the processes that influence internal mass loading EPLs is critical for assessing the potential long-term evolution of water chemistry. The first, and currently only, full-scale demonstration EPL, Base Mine Lake (BML), provides a unique opportunity to study internal mass loading processes and to assess their influence on cap water chemistry. By first determining the degree and distribution of CH₄ saturation in the FFT and then incorporating it into mass transport models, we can constrain both the impact of internal mass loading on water cap quality and the impact that ebullition has on EPL development. Porewater advection dominates internal mass loading in early years, but diffusion is likely to dominate at later times concomitant with declining FFT settlement rates (Carrier et al., 2007; Kaperski and Mikula et al., 2011; Dompierre et al. 2017). Self-weight consolidation of FFT will consolidate from the bottom up, greatly reducing the hydraulic conductivity at the base of the deposit. This consolidation limits flux into the underlying formations and primarily drive porewater advection upwards into the water cap (Dompierre and Barbour, 2016; Kabwe et al., 2018). Other processes proposed to affect mass loading include sediment mixing due to internal seiches, lake turnover, and ebullition (Fig. 1-1; Dompierre and Barbour 2016, Dompierre et al., 2017; Lawrence et al., 2016). The potential impact of the various transport and geochemical processes on the mass loading of chemical species from the FFT into the water cap are currently not well constrained. Numerical modelling can be used

to simulate observed chemical gradients to investigate these processes and estimate potential mass loading under long-term scenarios with varying geochemical or physical conditions.

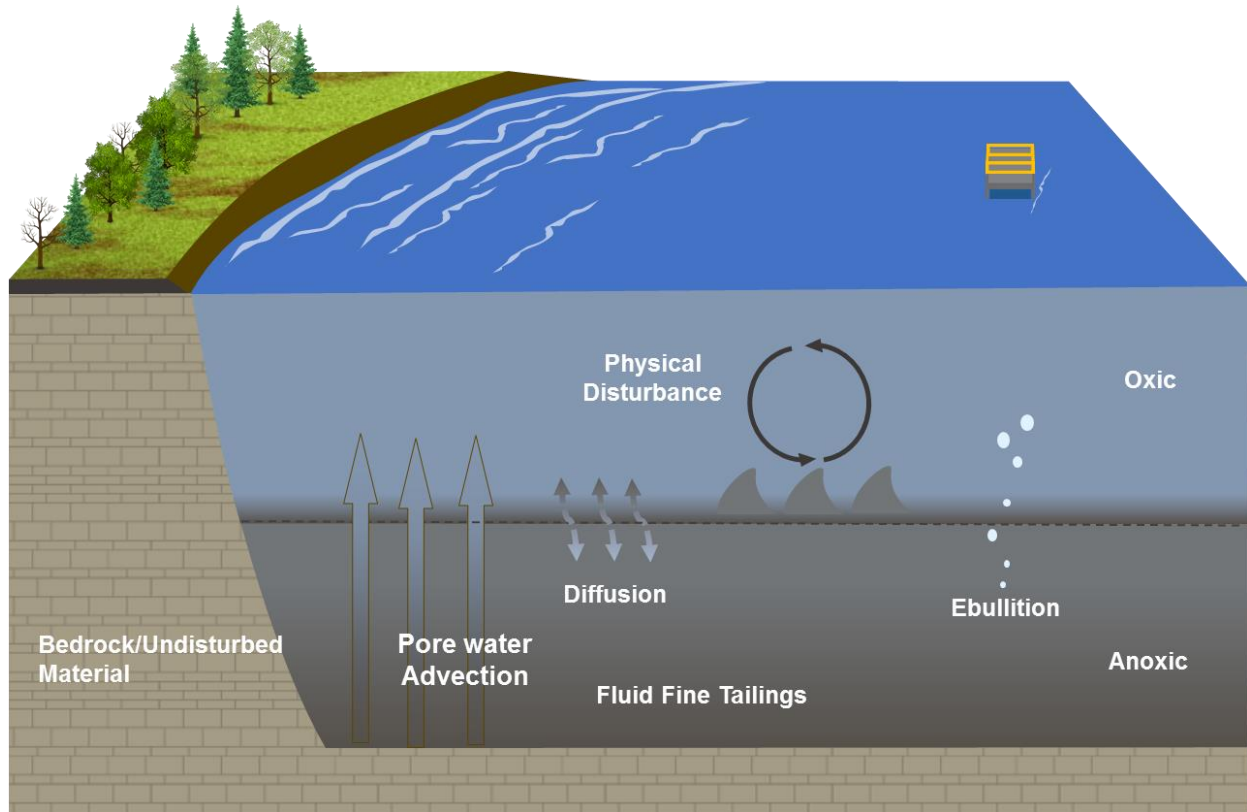


Figure 1-1: Initial conceptual model of processes and parameters in an oil sands EPL that affect internal mass loading from FFT to the overlying water cap (after Dompierre 2017).

CHAPTER 2: RESEARCH OBJECTIVES

My overall research goal is to constrain relationships between ebullition and internal mass loading of an oil sands EPL. Ebullition may alter physical properties of the FFT through mass entrainment and temporarily increase the volumetric water content in the FFT intervals over which ebullition occurs enhancing the mass loading into the water cap.

The overarching research hypothesis is that:

- CH₄ ebullition enhances FFT mixing and, therefore, increases internal mass loading in an EPL

The specific objectives are:

- define the spatial and temporal distribution of CH₄ ebullition release from an EPL considering variables including advection, water cap depth, FFT temperature, and porewater chemistry;
- develop advective-dispersive transport models for conservative constituents (i.e. Cl⁻, δ¹⁸O, δ²H, B) that consider spatial and temporal variability;
- define the magnitude of source or sink terms for the reactive species CH₄, using the conservative species transport model coupled with reactive terms; and
- estimate the long-term trends in internal mass loading from the FFT to the EPL as transport shifts from advection- to diffusion-dominated.

CHAPTER 3: LITERATURE REVIEW

3.1 Alberta Oil Sands

The Alberta oil sands comprise three separate bitumen deposits, the Peace, Athabasca and Cold Lake Oil Sands Regions which have a combined 166 billion barrels of proven reserves (Government of Alberta, 2019b). The cretaceous aged Wabiskaw – McMurray member of the Mannville group hosts oil sand ore (Hein and Cotterill; 2005). Oil sands are typically weakly cemented sandstone made of about ~10% bitumen, 5% water and 85% solids (Chalaturnyk et al., 2002). Crude oil can be extracted from these deposits by either in-situ methods, such as Steam Assisted Gravity Drainage, Cyclic Steam Stimulation and Cold Heavy Oil Production with Sand or by open-pit mining (Oil Sands Magazine 2019a, b). Recovery rates for in-situ methods vary from 40 to 60% depending on the technique and the deposit, whereas open-pit mining can approach 99% recovery. The extraction method depends on local geology ore depth. In situ methods typically require a minimum cover thicker than >200 m while open-pit mining is limited to within ~70 m of the original surface (Oil Sands Magazine 2019a, b). Although bitumen deposits are distributed over a 142, 000 km² area, only 4, 800 km² (~3.4%) of that area, located north of Fort McMurray contains deposits suitable for open-pit mining (Government of Alberta, 2019b).

Open-pit mining disturbs large areas of the northern Alberta landscape to access the deposits. This includes a diversity of land cover, ecozones includes a diverse range of ecosystems, such as forests, bogs, peatlands, and wetlands. Operators currently use truck-and-shovel methods to extract the bituminous ore. The ore is then mixed with a combination of recycled and freshwater and hydro-transported for extraction using various modified Clark Hot Water processes (Clark and Pasternack 1932; Kaperski, 2003). Bitumen is extracted from oil sands ore with hot water in a primary separation vessel and undergoes froth flotation separation. Bitumen is liberated from the water and most of the solids by attaching to bubbles and skimmed from the slurry. Froth treatment removes bitumen from the remaining water and fine solids by adding process aids like sodium hydroxide or sodium citrate, and diluents that are made of n-alkanes, iso alkanes and

monoaromatics (Masliyah et al., 2008; Gray, 2015). The bitumen extraction process generates coarse tailings, FTT and FFT.

3.2 Fluid Fine Tailings

Tailings impoundments currently store over 1,210 m³ of fluid tailings across the AOSR (Government of Alberta, 2019a). Deposited FFT are composed of about 60–70% OSPW, 20–35% solids, and 1–3% hydrocarbons (Allen, 2008; Kaperski, 1992; Kavanaugh, 2011). The solids comprise fine sand to clay-sized fine-grained quartz and clay minerals that are separated from the coarser sand-sized grains during the extraction process (Chalaturnyk et al., 2002). FFT porewater is OSPW, a mixture of water utilized in the upgrading process with connate water from the oil sands deposit. OSPW is alkaline, saline and contains organic compounds, including naphthenic acids and residual solvents used during froth treatment. (Allen, 2008; Dompierre et al., 2016; Kavanaugh, 2011). Major constituents in FFT porewater include bicarbonate (HCO_3^- ; 1200–1800 mg L⁻¹), sodium (Na; 880 ± 97mg L⁻¹), and chloride (Cl^- ; 560 ± 95 mg L⁻¹; Allen 2008; Dompierre et al., 2016; Penner and Foght, 2010; Rudderham, 2019). FFT porewater contains biogenic CH₄ (< 80 mg L⁻¹), and ammonium (NH₃-N; 11 ± 3 mg L⁻¹) which can consume dissolved oxygen via microbial oxidation (Allen, 2008; Dompierre et al., 2016; Rudderham 2019). Typically, FFT comprises a slowly settling slurry that can take many decades to dewater (Allen, 2008; Scott et al., 1985). FFT pose a long-term challenge to the closure landscape due to their due to high salinity, turbidity and high concentrations of oxygen consuming constituents (Gibson et al., 2013; White and Liber, 2018; Risacher et al., 2018).

3.3 Reclamation Strategies

Oil sands tailings reclamation is a major concern to both industry stakeholders and the Canadian public (BGC Engineering Inc., 2010). Per Alberta Government Directive 085, industry stakeholders are to reclaim disturbed areas used in oil sands mining to a self-sustaining boreal ecosystem integrated into the surrounding landscape (Alberta Government, 2016).

There are two broad categories for reclamation technologies that oil sand producers employ, terrestrial and aquatic remediation techniques. Terrestrial reclamation strategies involve creating an artificial upland landscape with tailings. FFT must be stabilized prior to placement to be

sufficiently stable and tractable to facilitate reclamation cover. Proposed strategies for terrestrial reclamation include thin lift dewatering, coagulation or flocculation, centrifugation, and mixing with other mine waste to form composite tailings (Kaperski and Mikula, 2011). Aquatic reclamation strategies are where the disturbed landscape is covered by a water cap to create a lake or pond. EPLs are a major aquatic reclamation strategy and can variably contain FFT, thickened FFT or process water. When an EPL or aquatic remediation technology involves tailings under a water cover it may be referred to as WCTT.

3.3.1. *End Pit Lakes*

End pit lakes are a reclamation strategy whereby fine tailings are pumped into a mined-out pit and capped with OSPW and freshwater. Pit lakes have been used extensively in more traditional mining settings in both metal and coal mines (Castro and Moore, 2000). Oil sands EPLs are an order of magnitude larger than pit lakes at hard-rock mines with water caps that are nearly twice as deep (CEMA, 2012; Kabwe et al., 2018). If successful, EPLs will be a key component of the closure landscape and form a major control on both the upstream and downstream hydrology of the AOSR (CEMA 2012). EPLs may be designed to receive surface drainage from the surrounding mine closure landscape and ultimately may discharge into the Athabasca River (Rudderham 2019). Between 24 and 32 EPLs have been proposed in the AOSR, eight of which are expected to have water capped FFT (Arriaga et al., 2019; Kabwe et al. 2018). To date, one commercial-scale demonstration EPL has been commissioned in the AOSR and filling of another with treated FFT, that is FFT amended with coagulants, is under way (Dompierre et al., 2016; Alberta Government, 2017).

In EPLs containing water capped FFT, it is anticipated that the FFT will settle and consolidate with time and that the water cover will improve in quality, such that a healthy ecosystem can be sustained. Numerical models predicted that self-weight consolidation through tailings settlement would be the primary driver of vertical fluid flow into the water cap (Dompierre and Barbour, 2016; Prakash et al., 2011). These models also predicted that settlement rates would decrease exponentially with time from ~ 1 to $\sim 0.1 \text{ m a}^{-1}$ over 30 years during preferential settlement of larger, heavier particles (Carrier et al., 2007).

3.4 Internal Mass loading

Internal mass loading is the chemical loading of a water body from its underlying sediments; in an EPL, the loading comes from the underlying tailings. Mass loading from the FFT to the overlying water cap is an important control on water quality within EPLs (Dompierre and Barbour, 2016; Dompierre et al., 2017). Increases in TDS due to internal mass loading can increase cap water toxicity (Liber and White, 2018). Oxygen consuming constituents such as CH₄ and ammonium in FFT porewater may indirectly cause oxygen depletion in the water cap (Chen et al., 2013; Penner and Foght, 2010; Risacher et al., 2018). These constituents have been found in tailings impoundments throughout the AOSR and are readily oxidized (Dompierre et al., 2016; Stasik et al., 2014; Stasik and Wendt Pothoff 2014, 2016). Long-term oxygen consumption in the water cap can lead to anoxia and threaten the sustainability of an EPL (Risacher et al., 2018). Due to the potentially negative impacts that internal mass loading may have on the success of an EPL, it is necessary to characterize the mass transport across the tailings water interface (TWI). Mass transport in an EPL is primarily a function of vertical advective dispersive transport upwards into the water cap as tailings consolidate in early time (Dompierre and Barbour 2016). Conservative mass transport can be described by the governing equation (Eq. 2-1) derived in detail in Dompierre (2017):

$$\frac{\partial C \cdot n}{\partial t} = \frac{\partial}{\partial z} \left[D_h \cdot n \cdot \frac{\partial C}{\partial z} \right] - \frac{\partial C \cdot q_z}{\partial z} \quad (\text{Eq. 2-1})$$

where C is the mass concentration of the solute in mass per unit volume, n is the porosity of the sediment as a fraction of pore volume to total unit volume, q_z is the vertical porewater flux, t represents time, z represents depth and D_h is hydrodynamic dispersion, the mechanical mixing due to tortuosity and concentration gradients during flow, represented as area per unit of time.

While some seepage is possible out of the bottom and sides of an FFT deposit, it is assumed that consolidation of the FFT along the pit boundaries forms a relatively low hydraulic conductivity layer limiting FFT porewater leakage in the surrounding units. This suggests that the predominant porewater release from FFT is upwards vertical advection (Kabwe et al., 2018).

Changes in FFT porewater chemistry, settlement rates, and temperature can all influence internal mass loading in an EPL. The water cap of an EPL is expected to become oxic with time, creating an oxygen gradient with underlying anoxic FFT. In BML, this gradient is centered on the TWI and down into the FFT. Generally, reducing chemical constituents increase in abundance with depth below the TWI while oxidizing constituents are greatest in the water cap (Dompierre et al., 2016; Risacher et al., 2018; Rudderham, 2019). This chemical gradient is generally confined to the uppermost 2 m of FFT.

Initial conservative transport models of mass loading within an oil sands EPL were developed by Dompierre and Barbour (2016) and Dompierre et al. (2017). These models, which were focused on BML, found that upward vertical advection, driven by FFT settlement, was the principal transport mechanism for conservative constituents such as $\delta^{18}\text{O}$, δD , temperature and Cl^- (Dompierre and Barbour, 2016; Dompierre et al., 2017). The 1-D models developed by Dompierre and Barbour (2016) and later refined by Dompierre et al. (2017) used the commercially available finite element software products CTRAN/W (GEO-SLOPE International Ltd., 2018a) and SEEP/W (GEO-SLOPE International Ltd., 2018b). The model domain was a 5 m vertical profile that extended down into the FFT deposit from the FFT-water interface. This domain was selected because it captures a geochemically-dynamic zone with a compositional transition from FFT porewater to cap water (Dompierre et al., 2016; Risacher et al., 2018). Physical properties were based on measured properties of sampled FFT or known values from literature, while various mixing mechanisms and advection rates were applied to simulate data.

Mass loading simulations using only advective-dispersive transport were unable to reproduce profiles of Cl^- , $\delta^{18}\text{O}$ and δD over the modeled period (Dompierre and Barbour, 2016; Dompierre et al., 2017). The authors subsequently incorporated a one-time mixing event by redefining the porewater chemistry to match the water cap. This periodic mixing was based on sudden TWI depth changes of up to a meter during sampling campaigns in October of 2014 (Dompierre and Barbour 2016). Best fits for $\delta^{18}\text{O}$ and δD were found with 1.1 m deep mixing events paired with a 1.46 m yr^{-1} advection rate (Dompierre and Barbour 2016). However, Cl^- profiles were better simulated with a lower advective rate of 0.73 m yr^{-1} with periodic mixing depths of over 0.5 – 0.75 m. The authors found that transient flow conditions provide the best fit

for Cl^- transport models and that varying conditions will greatly affect long term mass loading rates of conservative constituents (Dompierre et al., 2017).

Potential sources of periodic lake mixing identified during early BML development (2013–2015) included seasonal, primarily fall, lake turnover and strong wave action (Dompierre and Barbour, 2016; Lawrence et al., 2016; Hurley, 2017). However, lake turnover may have a much more limited effect on FFT mixing than previously thought due to water cap depth. Strong wave action has been shown have minimal effect of FFT resuspension potential and was instead proposed to affect already suspended sediments due to the designed water cap thickness (Lawrence et al., 2016; Hurley, 2017). Lake turnover and wave action are unlikely principal drivers of FFT mixing at the TWI; therefore, other mechanisms must be considered.

3.5 Methane Dynamics

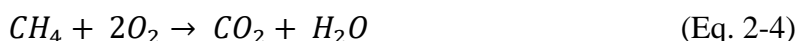
Methanogenesis, the in-situ biodegradation of labile organics, commonly occurs in oil sands tailings impoundments (Dompierre et al., 2016; Holowenko et al., 2000; Lawrence et al., 2016; Mikula, 2011; Penner and Foght, 2010; Risacher et al., 2018; Siddique et al., 2014; Stasik et al., 2014; Stasik and Wendt-Pothoff, 2016). Methanogenic microbes in oil sands tailings breakdown the labile components of unrecovered naphtha and paraffinic solvents used in bitumen extraction (Siddique et al. 2007; Siddique et al., 2018; Stasik and Wendt-Pothoff, 2016). Broadly, methanogenesis follows one of two pathways, acetoclastic (Equation 2-2) or hydrogenotrophic (Equation 2-3) methanogenesis, as shown below (Bethke et al., 2011):



Microbes that use either acetoclastic or hydrogenotrophic pathways are present in FFT stored in oil sands EPLs (Rudderham, 2019). However, the acetoclastic pathway likely dominates in fine tailings deposits as intermediate microbial organisms breakdown residual naphthas to produce acetate, which is used by methanotrophs (Siddique et al., 2014; Stasik and Wendt-Pothoff, 2014; 2016). Isotopic signatures of dissolved CH_4 (i.e., $\delta^{13}\text{C}\text{-CH}_4$, $\delta^2\text{H}\text{-CH}_4$) in FFT porewater from this EPL reveal that acetoclastic is currently the dominant pathway (Goad, 2017). However, as labile

carbon availability declines over time CH_4 production rates are expected to decrease, and the relative importance of the hydrogenotrophic pathway may become important (Rudderham, 2019).

Dissolved CH_4 is an important oxygen consuming constituent (OCC) in oil sands tailings ponds and limit dissolved oxygen concentrations in EPLs (Holowenko et al., 2000; Ramos-Padron et al., 2011; Risacher et al., 2018). Methane ebullition may resuspend tailings, increase water cap turbidity, influence internal mass loading and contribute CH_4 to the water cap (Kavcar and Wright, 2011; Lawrence et al., 2016). Atmospheric $\text{CH}_{4(g)}$ flux from EPLs may be a significant source of greenhouse gases in the Athabasca oil sands region (Holowenko et al., 2000; Yeh et al., 2010). The presence of $\text{CH}_{4(aq)}$ can drive anoxia throughout tailings ponds (Penner and Foght, 2010; Holowenko et al., 2000) via the following overall stoichiometric equation (Eq.2-4; Risacher et al., 2018):



Previous studies have shown that $\text{CH}_{4(aq)}$ is an important electron donor in oil sands tailings ponds and is easily oxidized by methanotrophs (Holowenko et al., 2000; Chen et al., 2013; Siddique et al., 2014). Aerobic methanotrophs have been found in tailings ponds and EPLs across the AOSR (Risacher et al., 2018; Saidi-Mehrabad et al., 2013).

Dissolved CH_4 concentrations within the water cover are commonly below detection limits due to $\text{CH}_{4(aq)}$ oxidation by methanotrophs. Risacher et al. (2018) and Arriaga et al. (2019) found that $\text{CH}_{4(aq)}$ was negatively correlated with oxygen suggesting $\text{CH}_{4(aq)}$ oxidation is coupled with O_2 consumption. Current literature indicates that relatively high $\text{CH}_{4(aq)}$ concentrations ($>84\mu\text{mol}$) in EPLs may inhibit the oxygen consuming capabilities of $\text{NH}_4^+_{(aq)}$, another OCC, and enhance the long-term impacts of OCC's in EPLs (Arriaga et al., 2019; Roy et al., 1996; Risacher et al. 2018). Water cap $\text{CH}_{4(aq)}$ concentrations range from $4.0\mu\text{g L}^{-1}$ in the epilimnion increasing with depth to 1.5 mg L^{-1} in the hypolimnion while concentrations rapidly increased with depth in the FFT up to an average of $59\pm 10\text{ mg L}^{-1}$ (Arriaga et al., 2019; Risacher et al., 2018; Rudderham, 2019). The sudden increase in $\text{CH}_{4(aq)}$ coincided with the approximate boundary between oxic and anoxic waters which was at the TWI until 2016 when the lowermost hypolimnion of the studied EPL experienced anoxia for part of the year (Risacher et al., 2018; Arriaga et al., 2019)

3.6 Ebullition Assessment Approaches

Multiple methods have been used to study ebullition in saturated and unsaturated sediments (Amos et al., 2005; Brennwald et al., 2005; Jones et al., 2014; Khurana et al., 2016; Scandella et al., 2011; 2017; Sirhan et al., 2019). The release of exsolved gases by ebullition requires that the porewater is saturated with the respective dissolved gas and exceeds the confining pressure. Temperature (T), pressure (P) and salinity control CH₄ solubility (Duan and Mao, 2006). Increased temperature and decreased pressure will lower CH₄ solubility and most likely to result in ebullition events if the porewater is at or near CH₄ saturated (Duan and Mao, 2006; Harrison et al., 2017; Scandella et al., 2011; 2017; Sirhan et al., 2019).

Ebullition of exsolved gases requires that the buoyancy of the bubbles exceed the overlying yield stress of the confining sediment to rise through the column (van Kessel and van Kesteren, 2002). Bubble release tends to occur as a chain of bubbles, creating a channel in the sediment from the depth of ebullition (Scandella et al. 2011; 2017). These channels may persist and be reactivated due to variations in properties that affect the yield stress of the overlying sediments (i.e. hydrostatic pressure fluctuations) or increased CH₄ exsolution, creating more bubbles. The channel depth and width are a function of the overlying pressure, sediment strength and CH₄ concentrations (Scandella et al. 2011; 2017; Sirhan et al., 2017).

Dissolved noble gas (NG) ratios are potential indicators of gas generation and consumption in porous sediments (Amos et al., 2005; Jones et al., 2014; Brennwald et al., 2005). Noble gases are chemical non-reactive species that exhibit mass-dependent trends in partitioning between aqueous and gas phases where heavier gases have higher solubilities than lighter ones (Brennwald et al., 2005; Holocher et al., 2002; Jones et al., 2014). Since meteoric waters represent the principal source of NGs in a near-surface system, they are potentially useful tracers of gas transport in systems where biogenic gas generation and consumption occur (Jones et al., 2014). For example, methanogenesis and ebullition within a shallow unconfined aquifer preferentially stripped lighter NGs from groundwater impacted by a crude oil spill (Jones et al., 2014; Amos et al., 2005). This trend occurs due to the lower solubility in water and higher partitioning coefficients on the light NGs into the gas phase (Jones et al., 2014).

Another approach for determining the potential for ebullition is to calculate the difference of total dissolved gas pressure (P_{TDG}) and total fluid pressure (P_f) at a given location (Khurana et al.,

2016; Roy and Ryan, 2013). The P_{TDG} is the sum of the partial pressures for all dissolved gases, whereas P_f includes the atmospheric pressure acting on the water surface plus the pressure imposed by the overlying fluidized sediment column (Manning et al., 2003; Roy and Ryan 2013). When a solution is equilibrated with the atmosphere, the P_{TDG} equals barometric pressure. Any in-situ processes that produce or consume dissolved gas will affect P_{TDG} (Ryan and Roy 2013). Exsolution and ebullition occur when P_{TDG} exceeds P_f (Fendinger et al., 1992; Khuruna et al., 2016). Total dissolved gas pressure values include the partial pressures of all dissolved gases, whereas gas saturation is determined for individual gases. Consequently, total dissolved gas pressures may be more indicative of ebullition potential than saturation values for individual dissolved gases. For example, in oil sands tailings ponds where dissolved gases may variably include $CO_{2(aq)}$, $CH_{4(aq)}$, ΣH_2S or O_2 among others (Risacher et al., 2018; Rudderham 2019).

CHAPTER 4: METHODOLOGY

An integrated approach was used to in this study by focusing on two key types of activity: the development of geochemical data sets by combining previously published data with new FFT sampling; and the development of new numerical models of conservative species-based mon models previously developed by Dompierre and Barbour (2016) and Dompierre et al. (2017).

Initial work focused on developing an understanding of the distribution and degree of CH₄ saturation across FFT within an EPL. Chemical transport models simulated observed depth profiles of conservative species in the FFT. These models were also used to evaluate newly proposed mixing mechanisms.

Data was collected from both published literature and sampling campaigns carried out in 2015 through 2019. FFT properties such as temperature and pressure measurements were collected for CH₄ solubility calculations, while solids content data were required for transport modelling. Depth profiles of Cl⁻ and CH₄ across the tailings/water interface (TWI) and into the deeper tailings across were collected from 2015-2017. Water cover depth measurements provide information about advection rates from self-weight consolidation. A summary of the data collected for this study and data obtained from published sources is presented below (Table 4-1).

Table 4-1: Summary of the different parameters studied and reviewed in this study.

Year	Temp.	$P_{\text{fluid}}/P_{\text{TDC}}$	B	Cl ⁻	δD	$\delta^{18}\text{O}$	CH ₄	CO ₂	Noble Gases
2014	✓ ^a	-	-	-	-	-	-	-	-
2015	-	-	✓ ^b	✓ ^{b,c}	✓ ^a	✓ ^a	-	-	✓
2016	-	-	✓	✓ ^d	✓	✓	✓ ^d	✓	-
2017	-	-	✓	✓ ^d	✓	✓	✓ ^d	✓	-
2018	✓	✓	-	-	-	-	✓	✓	-
2019	✓	✓	-	-	-	-	✓	✓	-

^a Dompierre and Barbour (2016)

^b Dompierre et al. (2016)

^c Dompierre et al. (2017)

^d Rudderham (2017)

4.1 Study Site

This research focused on Base Mine Lake (BML), which is located 35 km north of Fort McMurray, Alberta at Syncrude's Mildred Lake mine. This EPL has a 7.8 km² surface area and was created by depositing approximately 186 Mm³ of FFT between 1998 and 2012 into the mined-out West In-pit (WIP). During this time, WIP was used as a settling basin to recycle OSPW to reuse in the bitumen extraction process. The FFT was pumped in from the southern portion of Mildred Lake Settling Basin (MLSB) and Southwest In-Pit (SWIP) into the northeast and southwest of WIP, respectively, at various times. During filling, a 3 to 5 m water cap dominated by OSWP was present as WIP was a reservoir for the recycle water circuit in bitumen upgrading (Dompierre 2017). BML was commissioned in 2012 as the first commercial-scale demonstration EPL in the AOSR.

The design water cap surface elevation of 308 masl was reached in May 2013 by pumping in freshwater from nearby Beaver Creek Reservoir. This water surface elevation has since been maintained by balancing pumping out cap water for reuse in the bitumen extraction process and pumping in freshwater from BCR during ice free months (Fig. 4-1; Dompierre et al. 2017). Water cap surface elevation fluctuates by ≤ 0.5 m on an annual basis. The initial catchment area that discharges into BML is small (6.6 km²) but this area will increase as surrounding reclamation landforms are constructed and integrated into the catchment. Concurrent to increasing catchment area, freshwater volumes pumped in from BCR will decrease. Groundwater seepage into BML is estimated to be negligible relative to other inputs including pumping (5–10 Mm³), precipitation (~3 Mm³) and FFT self-weight consolidation (4.15 Mm³), and also compared to outputs (–10.0 Mm³; Dompierre et al., 2016; Dompierre 2017; Kabwe et al., 2018). In 2015, the BML chemical mass balance was dominated by porewater advection during FFT settlement and dewatering (Dompierre et al., 2017).

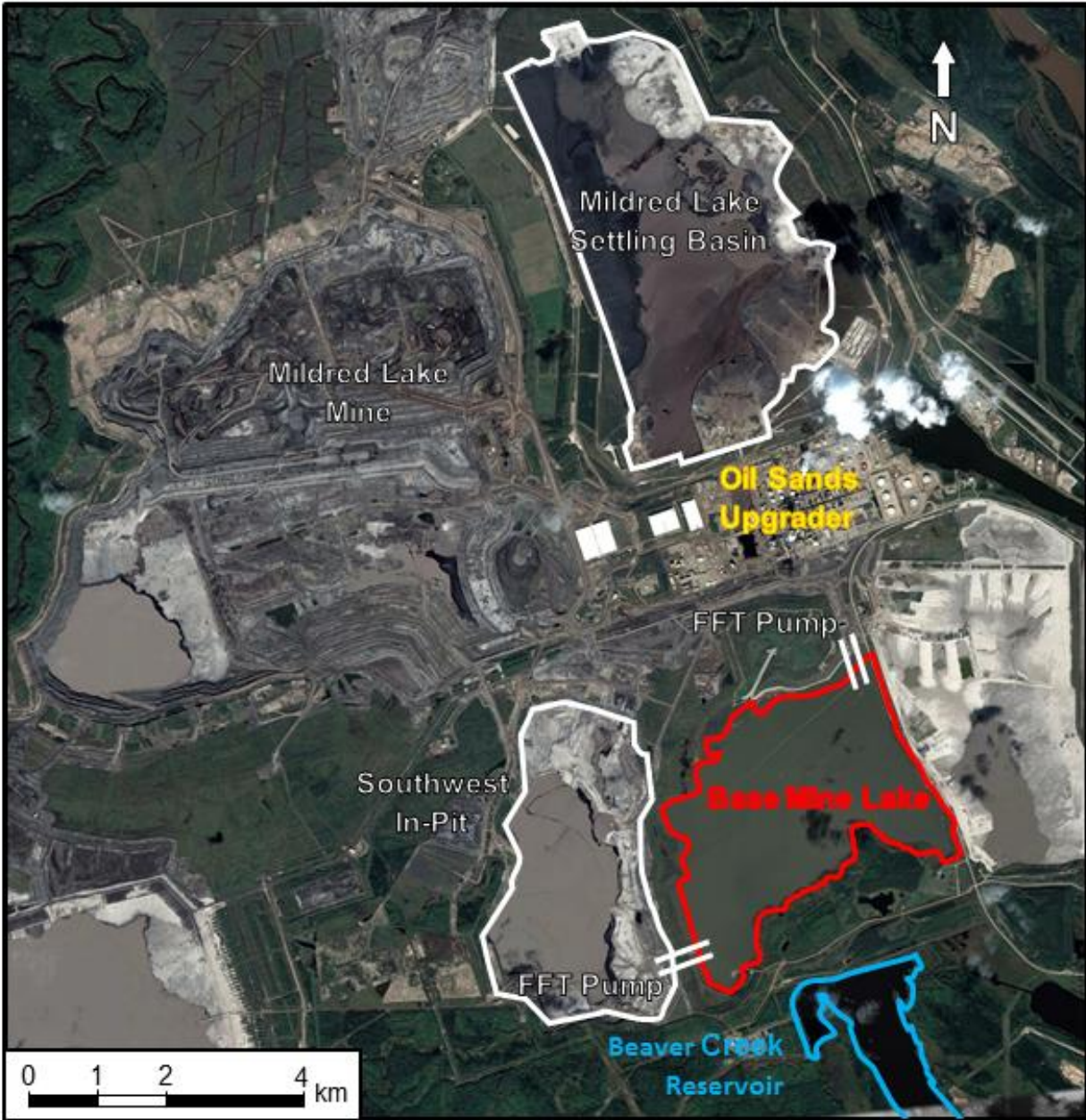


Figure 4-1: Satellite image of the Syncrude Canada Ltd. Mildred Lake Mine. The Athabasca River flows along the NE corner of the image.

An initial water cap depth of 5 m was selected to prevent FFT resuspension by wave action during storm events or fall turnover (Lawrence et al., 2016). Due to tailings self-weight consolidation, where the FFT settles from the bottom up, the water cover thickness increased to between 8 and 12 m by 2017 (Dompierre et al., 2016; Barr Engineering, 2017). At commissioning

FFT thickness averaged 45 m and decreased to an average of ~40 m in 2016 but can vary from ~15 m to ~50 m depending on the topography of the pit bottom (Barr Engineering, 2017). Three sampling platforms – Platform 1 Center (P1C), Platform 2 Northeast (P2NE) and Platform 3 Southwest (P3SW) – are positioned along SW-NE transect of BML (Fig 4-2). Many sampling programs and long-term studies utilize these platforms (e.g. Dompierre et al., 2014; 2016; Dompierre and Barbour 2016; Risacher et al. 2018; Rudderham 2019; White and Liber 2019). Rates of tailings settlement within FFT vary across BML. Between commissioning in late 2012 and 2017, annual sonar surveys carried out by Barr Engineering (2018) show greater settlement in the northeast corner (6–7m) compared to the southwest (4–5 m; Dompierre and Barbour, 2016).

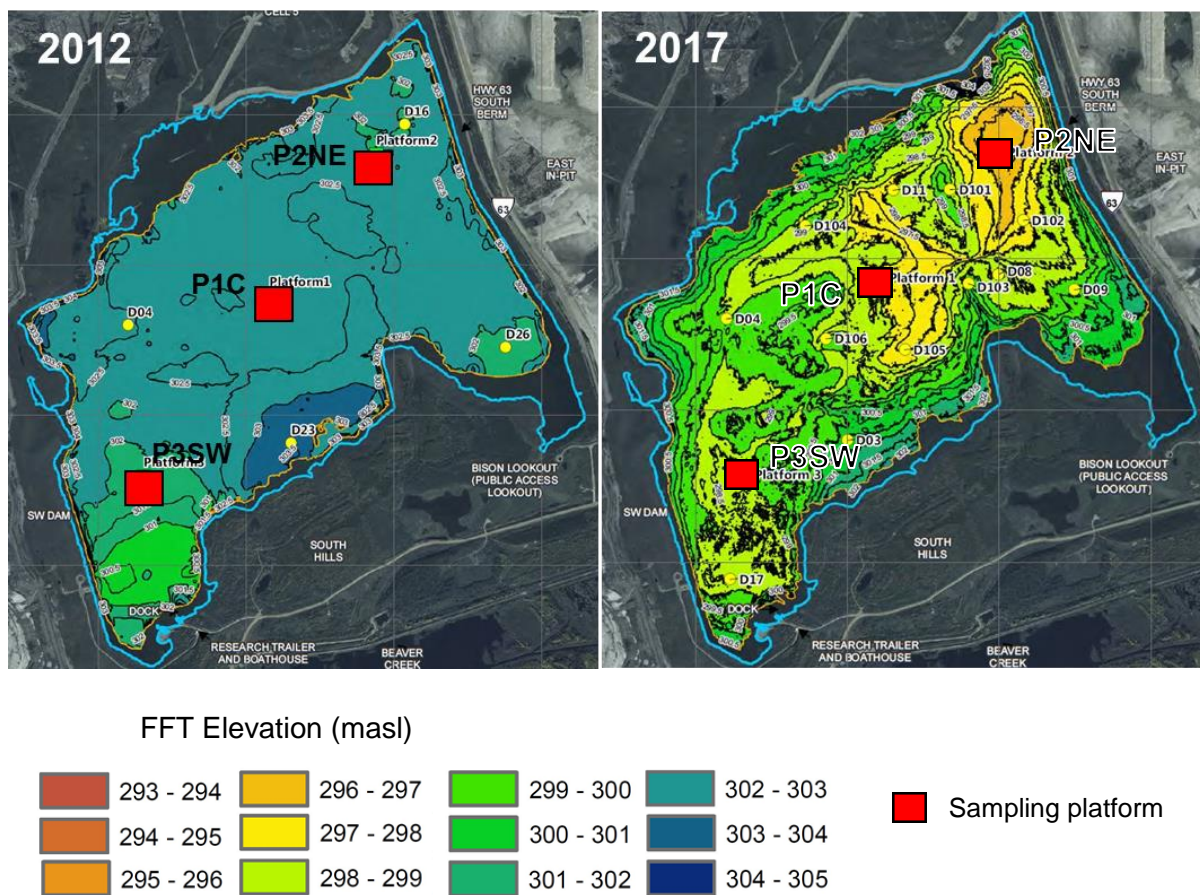


Figure 4-2: FFT elevation map showing TWI elevation (masl) in 2012 after commissioning and in October 2017. Modified from Barr (2018).

4.2 Data Collection

Data collected for this project was part of a much larger overall study on various aspects of BML FFT. Previously published data includes temperature and geochemical profiles from 2015 (Dompierre et al., 2014; 2016; 2017; Dompierre and Barbour 2016) as well as geochemical profiles in 2016 and 2017 (Rudderham 2019). New temperature and pressure data were collected in 2018 and 2019.

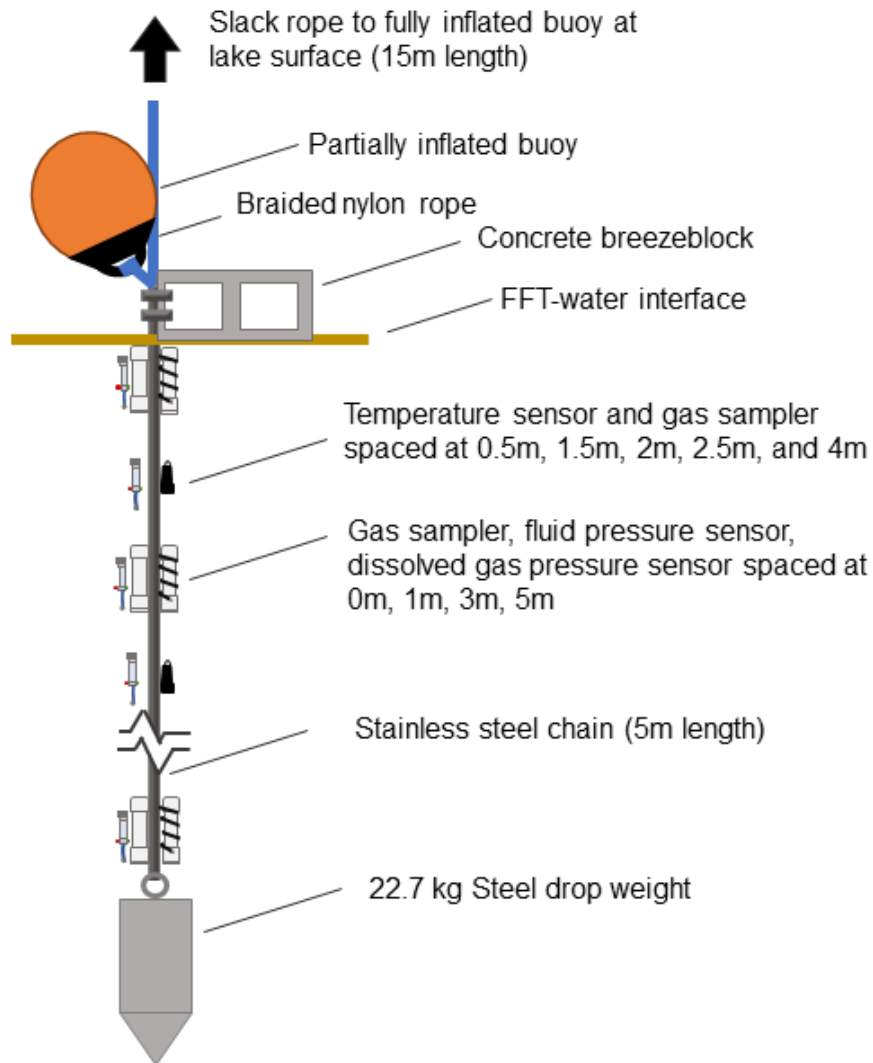


Figure 4-3: Schematic diagram of pressure, temperature and passive gas samplers deployed in BML summer 2018 (after Dompierre et al., 2014).

4.2.1. *Temperature and pressure*

Early temperature profiles and annual changes were retrieved from Dompierre et al. (2014), where a comprehensive temperature survey of ~40 m FFT in BML was carried out from September 2013 to March 2014 utilizing thermistors with data loggers on weighted chains (Dompierre et al., 2014). Data collection abruptly ended with the breakup of ice cover removing the thermistor strings from the FFT during ice movement.

In this study, continuous temperature and pressure surveys were carried out at the three platforms over two ice-off periods in 2018 and 2019: August 8th, 2018 to October 10th, 2018 and May 29th, 2019 to October 10th, 2019. An additional, temperature/pressure survey was carried out at only P3SW from February 4th, 2019 to March 11th, 2019 due to restricted ice access. Pressure/temperature (Solinst m30 Levelloggers) and temperature (HOBOWare Pro V2) recording sensors were deployed over the upper 5 m of FFT on a modified array similar to the previous thermistor deployment as used by Dompierre et al. (2016; Figure 4-3; Table 4-1). Both types of sensors were configured to record hourly during the deployment period. The pressure/temperature sensors recorded absolute pressure (kPa) at a resolution of $10^{-4} \pm 0.147$ kPa and temperature (°C) at a reported resolution of 0.003 ± 0.05 °C (Solinst Canada Ltd., 2018). The pressures were referenced to a concurrently recording barometric pressure sensor (Solinst Barologger Edge) on the shoreline and on P1C in the center of BML. The barometric sensor recorded pressure with a reported accuracy of 0.05 kPa. The temperature sensors had a reported a resolution of 0.02 ± 0.2 °C (Onset Computer Corporation, 2010). The sensor arrays were deployed within 0.5 m of the TWI, this was verified by the on-board sonar range finder (accurate to within 0.1 m), and by comparing recorded P_{fluid} to calculated pressure values based on solids content. Fluid pressure data from P2NE during the 2019 deployment suggests that the sensors did not reach the intended depths and were disturbed during the sensor deployment. The data suggest that many sensors clustered at approximately 0.75m to 1.25m below the TWI while the bottom-most sensor was only at 3.5m below the TWI.

Fluid and dissolved gas pressures were measured in summer 2018 with Solinst m30 Levelloggers using custom fabricated housing at 0 m, 1 m, 3 m and 5 m intervals below the FFT-water interface (Fig. 4-3). Dissolved gas pressure was recorded using a sand packed watertight housing with gas permeable tubing. These values were compared with theoretical fluid pressures

values based on depth below the water surface and solids content data. The P_{fluid} at a specific depth can be calculated by multiplying the density of solids by volume fraction of solids and adding that to the remaining volume fraction multiplied by the density of water. Passive sampling of dissolved gases was taken concurrently with 30 mL syringes fitted with gas permeable membranes placed adjacent to pressure sensors and left to equilibrate for the duration of the deployed period.

4.2.2. Porewater chemistry

Samples for geochemical analysis were collected via methods previously described in Dompierre et al. (2016) and Rudderham (2019) at all three sampling platforms. Briefly, high-resolution sampling across TWI used a fixed interval sampler (FIS; Fig. 4-4), which is an array of 20 pneumatically controlled 250 mL piston samplers spaced at 10 cm vertical intervals. The FIS was lowered to the FFT-water interface with ~ 4 intervals above the TWI to provide high-resolution geochemical data of the uppermost FFT where known sharp geochemical gradients are present (Dompierre et al., 2016; Rudderham, 2019). Samples from greater depths were obtained using a fluid sampler (FS; Fig. 4-4), which is a single pneumatically controlled 4 L piston sampler (Dompierre et al., 2016). Sampling campaigns were carried out in 2015, 2016, and 2017. Samples were collected at 0.5, 1, 2 and 4 m intervals with increasing depth below the lowest FIS piston depth. Temperature and pH were recorded on the sampling boat immediately following collection. Sub-samples for dissolved gas analysis were collected into amber glass serum bottles (FIS) or IsoJars (FS), sealed and frozen until analysis. Samples were transferred into 250 mL high density polyethylene (HDPE) bottles and stored on ice for up to eight hours until they could be transported to an onsite laboratory for analysis.

Porewater was extracted by centrifuging FFT samples at $8500 \times g$ for 30 minutes. The supernatant was collected, filtered and preserved according to standard methods, and stored in clean HDPE bottles at 5°C until analysis (Dompierre et al., 2016; Rudderham, 2019). Briefly, Cl^- concentrations were quantified by ion chromatography (IC; detection limit 0.05 mg L^{-1}) on samples passed through $0.45 \mu\text{m}$ polyethersulfone (PES) filter membranes. Dissolved B concentrations were quantified by inductively coupled plasma-mass spectrometry (ICP-MS; detection limit $0.05 \mu\text{g L}^{-1}$) on samples passed through $0.2 \mu\text{m}$ (2015, 2016) or $0.1 \mu\text{m}$ (2017) PES filter membranes and acidified to $\text{pH} < 2$ with trace metal grade HNO_3 . Stable isotopes of water were analyzed using a vapour equilibration method developed by Wassenaar et al. (2008) for

deuterium ($\delta^2\text{H}$) and oxygen-18 ($\delta^{18}\text{O}$). These isotope samples were collected, filtered and stored according to the method described for IC analyses. Prior to analysis, 10 mL of sample was transferred to a double sealed Ziploc bag with dry air. The water and air were left to equilibrate for approximately one hour. A syringe was used to transfer equilibrated water vapour to a Picarro L-2120-I Cavity Ring down Spectrometer for analysis.

Dissolved CO_2 and CH_4 gas samples were analyzed for FFT samples collected in 2016 and 2017 using the FIS and FS. Subsamples from the FIS were immediately transferred into 120 mL amber serum bottles using 60 mL catheter syringes and quickly crimp sealed with a blue butyl septum stopper and aluminum ring. Subsamples from the FIS were directly extruded into 500 mL IsoJars. The lids were screwed tight and sealed with vinyl adhesive tape. Samples were stored in on ice for up to ten hours before being transferred to a freezer and stored at $-20\text{ }^\circ\text{C}$ until analysis.

After 2017, no further porewater geochemistry sampling campaigns were conducted, dissolved gas sampling methods were adjusted to reflect this. Passive gas sampling through deployment of samplers on a weighted chain were used in both 2018 and 2019 but sampler design changed between years due to water entry into the syringes in 2018. The passive gas samplers in both years were spaced every 0.5 m starting at the TWI down to 5 m below the TWI (Fig. 4-3). In 2018 15 mL syringes were fitted with a gas permeable/water impermeable (Masterflex® silicone) tube 0.15 m in length to allow gas diffusion from FFT porewater into the syringe. The tubing was fitted with an HDPE stopper and sealed with silicone. The syringes were wrapped in a Ziploc bag and bound in electrical tape to create a seal. The samplers were deployed with temperature and pressure sensors during summer 2018. Upon retrieval, most syringes had visible water (i.e., water entry pressure exceeded) in them rendering them unsuitable for gas chromatography analysis.

In 2019, the gas sampler design was revised to follow the method of Goad (2017) where plastic 30 mL syringes were filled with tap water and fitted with Masterflex® silicone tubing that was sealed with silicone. The syringes were placed in a perforated PVC pipe housing to protect the syringe from damage. The samplers were deployed on the sensor array described in section 4.2.1 (Fig. 4-3) on May 28th 2019 and recovered October 16th 2019. Upon recovery to the surface the tubing on the syringe was removed and a luer lock needle was attached to inject the water into an evacuated 60 mL serum bottle. The bottles were prepared by being evacuated for 5 minutes in an anoxic chamber and sealed with a 13 mm blue butyl stopper crimped with an aluminum ring.

The samples were stored in coolers with ice packs and brought back to the University of Saskatchewan where they were stored in a freezer (-4°C) until analysis.

Dissolved gas analysis was carried out using a headspace equilibration method per Goad 2017. Prior to analysis, these samples were thawed in a refrigerator at 4°C and placed on a shaker for at ambient laboratory temperature for 12 to 24 hours prior to analysis. High-purity $\text{He}(\text{g})$ was injected into the bottles and IsoJars using a gas-tight syringe and the same volume – either 1 or 3 cc – was again draw into the syringe. Headspace CH_4 and CO_2 concentrations were quantified on a gas chromatograph fitted with a PoraPLOT column and thermal conductivity detector. Following analysis, the samples were again frozen, opened and headspace volumes were determined by water addition. This was achieved by weighing the containers before and after adding DI water to completely fill the headspace. The added DI water was decanted and gravimetric water contents were then measured to determine the water volume within the initial sample.

Samples for dissolved noble gas analysis were collected in 2015 using a modified version of the method per Jones et al. (2014). Briefly, FFT samples were collected into a copper tube using the FIS. The top of the copper tube was attached with a compression fitting to the bottom of the FIS and a cable-actuated ball-valve was attached to the bottom. The FFT samples were drawn through the copper tube from the desired depth and sealed with the ball valve to maintain *in situ* pressures. Upon retrieval to the surface, the copper tubing was immediately crimp sealed. The samples were then shipped to the Noble Gas Laboratory at the Swiss Federal Institute of Technology (Zurich, Switzerland) where analyses followed established methods (Beyrele et al., 2000; Kipfer et al., 2002; Huber et al., 2006; Jones et al., 2014).

4.2.3. *Solids Content*

Subsamples of FFT taken during geochemical sampling campaigns were subjected to a modified Dean-Stark hot water extraction method to determine bitumen, water, and solids contents (Dean and Stark, 1920; Dompierre and Barbour (2016).

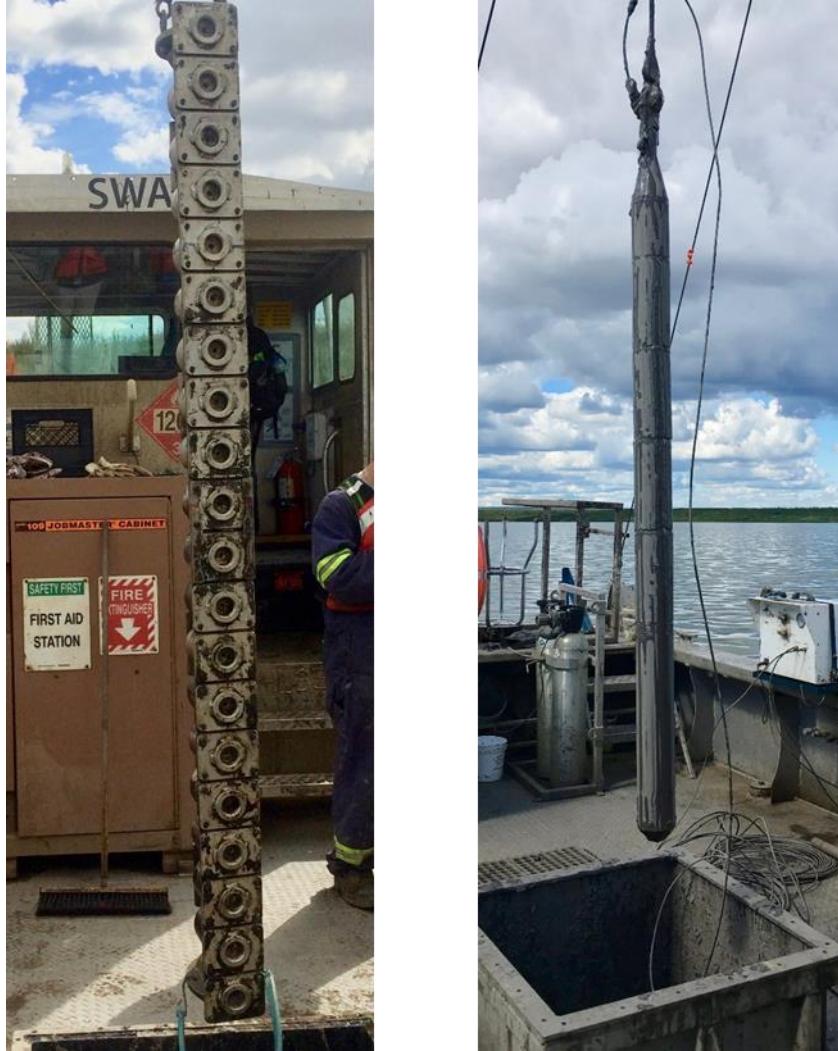


Figure 4-4: Fixed interval sample, (left) and fluid sampler (right; Rudderham 2019).

4.2.4. *Settlement rates*

Porewater advection can be calculated from tailings settlement by the displaced elevation. Therefore, high-resolution measurements of the FFT surface elevation were obtained from annual sonar surveys performed between 2013 and 2017 by Barr Engineering (2018). These sonar surveys were conducted with a Lowrance 200-KHz sonar transducer, recording units, and GPS, with a resolution of up to 0.1 m; data is processed using Lowrance sea bottom mapping software to determine the FFT-water interface elevation (Barr Engineering, 2017). Water surface elevation was determined using a Trimble Real Time Kinetic or supplied by Syncrude (Barr Engineering, 2017). Data from these surveys were supplemented by point measurements of TWI elevations

during sampling from both sonar and solids content data during FFT geochemical sampling (Dompierre et al., 2016; Rudderham; 2019).

4.3 Methane Ebullition Potential

Methane solubility was calculated using the published model of Duan and Mao (2006) for calculating CH₄ solubility in a saline solution. This model uses temperature, fluid pressure, and salinity to calculate solubility. Fluid pressures were calculated for each location using barometric pressure, water cap elevation, TWI elevation and FFT solids content data (Dompierre and Barbour, 2016; Barr Engineering 2018). Temperature and salinity values are based on data from sampling campaigns and published values (Dompierre et al., 2014; Dompierre and Barbour 2016). When compared to calculations using Henry's Law, the results are somewhat similar at lower pressures but deviate with increasing pressure or decreasing temperature. To determine which parameters have a greater influence on CH₄ solubility, sensitivity analyses were carried out, systematically varying each parameter by the maximum and minimum observed at BML (Fig. 4-5).

The CO_{2(aq)} solubility limit was calculated using the Van't Hoff equation (Eq. 4-1) to first establish the K_H for the given conditions for each sample, then Henry's law was used to calculate the theoretical solubility at the conditions for each sample:

$$K_H = K_{H\theta} \times e^{-C\left(\frac{1}{T} - \frac{1}{T_\theta}\right)} \quad (\text{Eq. 4-1})$$

where K_H is the equilibrium constant for the given conditions, $K_{H\theta}$ is the equilibrium constant at known conditions, T is temperature at the given condition and T_θ is the temperature for the known conditions. The constant C (K) is a tied to the species, CO₂.

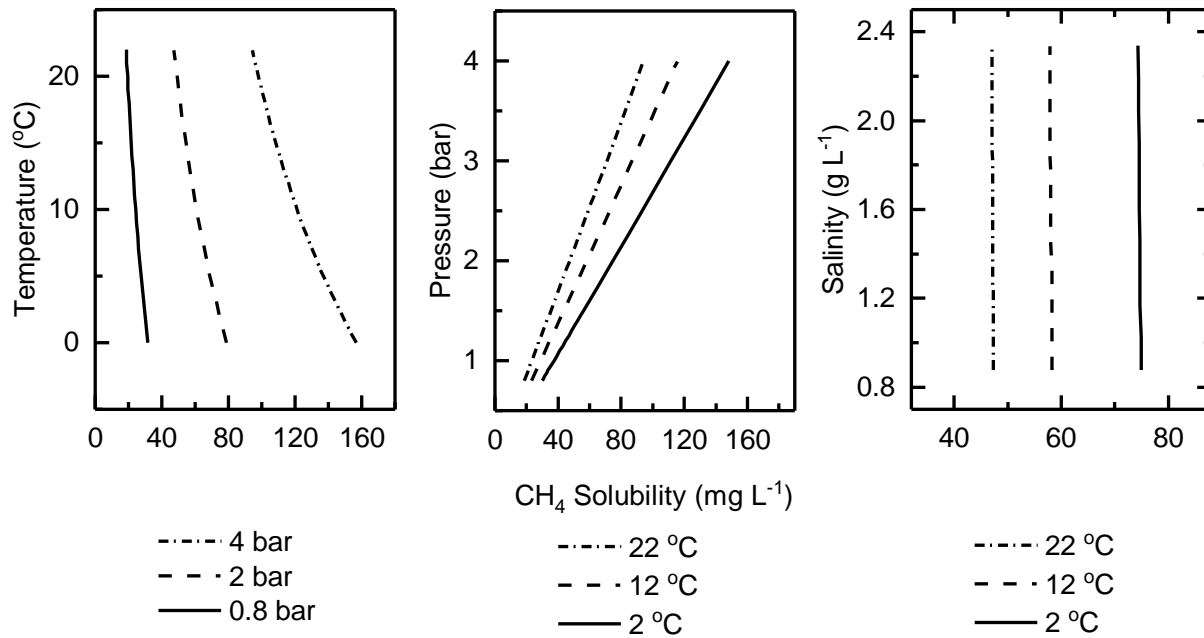


Figure 4-5: Results of sensitivity analysis for the three controlling parameters on CH₄ solubility for the range of conditions observed at BML.

4.4 Transport Modelling

One-dimensional mass-transport modelling utilized CTRAN/W and SEEP/W, a commercially available finite element modelling software (GEO-SLOPE International Ltd., 2018 a, b). The transport models developed in this study were similar to those developed by Dompierre and Barbour (2016) and Dompierre et al. (2017), with three key differences. First, separate simulations were run for each platform location rather than undertaking a single simulation to represent all of the FFT profiles. This model refinement was undertaken in order to more accurately represent the different observed rates of settlement at each platform and the impact this had on the Cl⁻ and B concentration profiles (Figs. 5-1, 5-5, 5-6). Next, as previously described, enhanced mixing was attributed to CH₄ ebullition and applied as an enhanced depth varying coefficient of diffusion rather than by periodic mixing of a specified depth of the FFT. Finally, the rates of advection were tied to the evolution of the observed settlement rate rather than set as average constant flow rates (Dompierre and Barbour, 2016; Dompierre et al., 2017).

The models simulate conservative mass transport in a saturated medium via two mechanisms: i) advective dispersive transport of solute in FFT porewater and ii) FFT porewater mixing with BML surface water. This mixing is by variably continuous ebullition represented by enhanced diffusion coefficients in the tailings. As such, the model builds off of equation (2-1) as described earlier in this work and derived in detail in Dompierre, 2017.

The model domain was set up per Dompierre and Barbour 2016, described as follows: a vertical 10 m column of water overlying a 5m column of FFT divided into five 1 m sections. The model mesh was set to 0.05 m. The model period was set to start at the beginning of May 2013, as this would coincide with the timing of published models and the onset of freshwater pumping into BML. The model was run through to the end of 2019, but profiles were selected that coincided with the sampling dates for geochemical profiles in 2015, 2016, and 2017.

Boundary conditions were applied to the bottom and top of the FFT portion of the model. The bottom of the domain had two boundary conditions; the first was upwards porewater advection as a water flux ($\text{m}^3 \text{d}^{-1} \text{m}^{-2}$). Advection for each model location was based on FFT elevation data provided by Barr Engineering from annual sonar surveys for the modelled location (Barr Engineering, 2017). The second lower boundary condition was a constant solute concentration representing the deeper FFT porewater concentrations, which have been shown to be relatively constant at depth (Rudderham, 2019). Upper boundary conditions were applied to the TWI at the top of the FFT column as previous modelling work due to the observed sharp gradients and the relatively consistent values in conservative constituents throughout the water cap relative to the FFT (Dompierre and Barbour 2016; Dompierre et al., 2017). The boundary conditions applied were a constant head of 10m to represent an average head of the water cap and a constant conservative constituent concentration representative of the water cap.

Material properties for the models are retrieved from recently published data in Dompierre et al. (2016); Dompierre and Barbour, (2016); Dompierre (2017) and Dompierre et al., (2017). These material properties include diffusion coefficients, volumetric water content, dispersivity, and saturated conductivity. It is expected that the uppermost FFT will remain consistent in material properties over time due to self-weight consolidation working as a bottom-up process (Dompierre and Barbour, 2016).

Unknown parameters will be constrained through successive modelled profiles to identify possible values for those parameters, i.e. enhanced diffusion coefficients for conservative depth profiles to represent mixing from ebullition. Due to changes in temperature from seasonal cycles (Dompierre et al., 2014) and pressure from FFT settlement (Barr 2018), which both affect CH₄ solubility and, therefore, exsolution, mixing by CH₄ ebullition is not expected to be consistent. Therefore, a variable amount of diffusion coefficient enhancement on an annual basis will be applied. This was achieved by creating a simplified alternating mixing profile where it is expected that CH₄ ebullition will be much greater during the warm periods in the FFT and lower during the cold months. A variable diffusion coefficient add-in for the modeling software was created to represent high intensity bubbling the summer months and low/no bubbling in winter months. The FFT D_h was enhanced by 2.5, 10x, and 25x the published values (Table 4-1; Dompierre and Barbour, 2016)

The selected conservative constituent for used in the modelling were Cl⁻ (mg L⁻¹), δ¹⁸O (‰), δ²H (‰), and Boron (µg L⁻¹). The first three were selected based on use in previous modelling work at BML and due to their prevalence in other modelling research in conservative mass transport modelling (Dompierre and Barbour, 2016; Dompierre et al., 2017; Hendry et al., 2014; 2013). Boron was selected as an additional constituent due to available data from earlier campaigns and its use as a conservative tracer (McCance et al., 2018; Ruecker et al., 2017; Wolf et al., 2012).

Table 4-2. Model parameters used, and the enhanced diffusion coefficients applied to the model to simulate ebullition. The enhanced diffusion coefficients were only applied to the upper 2 m of the model domain

Depth Interval (m)	Volumetric Water Content ^a	Diffusion Coefficient (m ² s ⁻¹)			
		1×	2.5×	10×	25×
0–1	0.86	8.6×10 ⁻¹⁰	2.1×10 ⁻⁹	8.6×10 ⁻⁹	2.1×10 ⁻⁸
1–2	0.85	8.2×10 ⁻¹⁰	1.2×10 ⁻⁹	4.9×10 ⁻⁹	9.9×10 ⁻⁹
2–3	0.84	7.9×10 ⁻¹⁰	7.9×10 ⁻¹⁰	7.9×10 ⁻¹⁰	7.9×10 ⁻¹⁰
3–4	0.83	7.7×10 ⁻¹⁰	7.7×10 ⁻¹⁰	7.7×10 ⁻¹⁰	7.7×10 ⁻¹⁰
4–5	0.82	7.4×10 ⁻¹⁰	7.4×10 ⁻¹⁰	7.4×10 ⁻¹⁰	7.4×10 ⁻¹⁰

^aDompierre and Barbour (2016)

After developing advection-dispersive models, reactive transport simulations were conducted by incorporating source/sink terms for key reactions affecting CH₄ fluxes. Reactive terms are modelled as decay rate (s⁻¹), a q mass flux (g m⁻² d⁻¹) or as Q mass rate (g d⁻¹) to pull

the advective-dispersive curve previously generated to match the data of the reactive species. The models were run to coincide with depth profiles sampled in 2016, 2017 and 2019.

Based on research by Rudderham (2019), two key reactions were included. First, CH₄ production leading to porewater saturation occurs approximately 1.5 to 3 m below the TWI depending on location and year. Second, CH₄ oxidation occurs within the upper 1.5 m of FFT immediately below the TWI. Methane production was simulated by setting a lower boundary condition in the model to a CH₄ concentration representing porewater saturation with respect to CH₄. If the CH₄ concentrations are normalized relative to this value then this boundary condition is represented by a C/Co of unity, or the maximum value. The CH₄ oxidation was modelled by applying a CH₄ consumption rate across the upper 1 to 2 m of the profile. The consumption rate represents oxidation of CH_{4(aq)}. The following equation (Eq. 4-1) results when the consumption term is applied as a single reaction term, R (g d⁻¹ m⁻²), to the transport equation described in section 3.1.

$$\frac{\partial C \cdot n}{\partial t} = \frac{\partial}{\partial z} \left[D_h \cdot n \cdot \frac{\partial C}{\partial z} \right] - \frac{\partial C \cdot q_z}{\partial z} + R \quad (\text{Eq. 4-1})$$

The CH₄ consumption rate was varied until a reasonable fit was obtained between the model and the field observations. The mass release rate from the FFT into the water cap was then calculated from the model.

CHAPTER 5: RESULTS

This section will present and compare results from current field programs with previously published data from BML. Solids content, presented as volumetric water content, will be compared with data from 2014 and recent work in 2017 (Dompierre and Barbour 2016). The changes in TWI elevation over time will be compared with predictive consolidation models to develop an understanding of the nature of settlement in BML. An annual temperature cycle is developed based off of data from the 2018 and 2019 sensor deployments. The influence of seasonal cycles is investigated by comparing changes between 2018–2019 and published data from 2013–2014. Results from deployment of pressure sensors in 2018 and 2019 will be presented comparing the dissolved gas pressure and fluid pressure. New data from recent field programs in 2016, 2017, and 2019 will supplement published geochemical data for dissolved ions, gases and stable isotopes (Dompierre et al., 2016; Rudderham 2019).

5.1 Volumetric Water Content

Volumetric water content (VWC) was calculated from gravimetric solids content using the relationship between the masses and the densities of the three principal FFT constituents (i.e., bitumen, solids, and water). Calculated VWC for 2017 samples was generally consistent with 2014 results (Dompierre and Barbour, 2016). In 2014, VWC sharply decreased with depth from 0.87 ± 0.02 (standard deviation) at the TWI to 0.79 ± 0.03 at 2.0 m under the TWI. VWC decreased slightly with increasing depth to 0.77 ± 0.05 remainder of the 15 m the sampled profile in 2014 (Dompierre and Barbour, 2016).

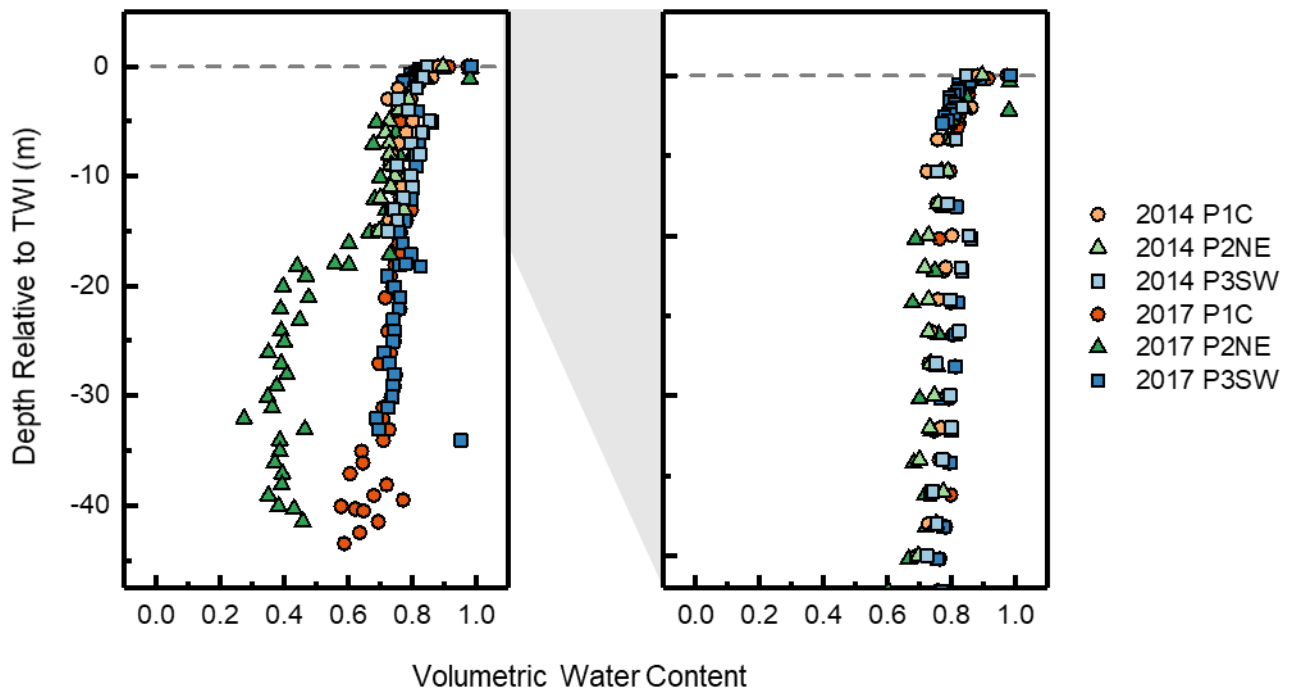


Figure 5-1: Volumetric water content profiles for 2014 and 2017 extending to 45 m (left) and 15 m (right) below the TWI.

At P1C, P3SW and over the upper 15 m of P2NE VWC averaged 0.77 ± 0.05 and values were generally consistent from 2014 to 2017. In contrast, P2NE VWC decreased to less than 0.41 ± 0.09 at depths more than 15 m below the TWI (Fig. 5-1). This decrease in VWC is attributed to sand mixed with the FFT in the lower part of the deposit in the NE portion of BML, which was identified in previous solids content surveys (Barr Engineering, 2018). As the VWC profiles in the upper 15m of FFT are not changing over time, this may indicate that shallow FFT are not dewatering, which is to be expected based on predicted bottom up consolidation (Fig. 5-2; CEMA; 2012, Dompierre and Barbour, 2016; Kabwe et al., 2018).

5.2 Settlement

Results from annual TWI elevation surveys, FFT geochemical sampling campaigns, and temperature/pressure sensor deployments indicate settling at a decreasing rate. From October 2012 to October 2019, TWI elevation dropped by 6.5 m at P2NE, 4.7 m at P1C, and 4.2 m at P3SW (Fig. 5-2). The results indicate that FFT near P2NE is settling at a greater rate than predicted by

consolidation models which may be due to more recently deposited tailings near the pump from MLSB (Carrier et al., 2007; Barr Engineering, 2018). Nevertheless, FFT settlement rates have decreased over time at all platforms. The largest decrease was at P1C, where settlement was 0.3 m from 2017 to 2019 compared to 2.3 m from 2012 to 2014.

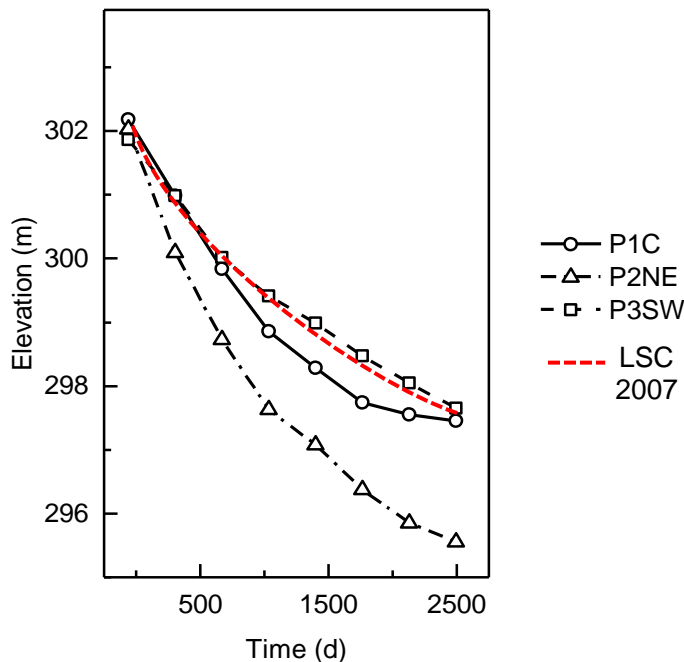


Figure 5-2: Measured TWI elevations compared to modelled elevations based large strain consolidation (LSC) simulations by Carrier et al., 2007.

Since settlement begins immediately after deposition, FFT age (timing of deposition) likely influences the different rates of observed settlement within BML. For example, locations and depth intervals where FFT deposition occurred earlier during the BML filling period (i.e. 1994 – 2012) will have undergone a greater degree of settlement. Therefore, shallow portions of the FFT deposit, which were deposited towards the end of the filling period are still undergoing early stage FFT settlement as predicted by consolidation modelling (Carrier et al., 2007). While the base of the deposit is also the oldest, laterally, the last tailings to be pumped in BML were in the NE corner near P2NE (Dompierre, 2017). These younger FFT may influence the greater settlement observed.

5.3 Temperature

Results from 2018 and 2019 show that seasonal FFT temperature variations are greatest at the TWI, with seasonal temperature variations diminishing with depth until they remain relatively

constant at depths greater than 5 m below the TWI. Average annual temperature ranges decreased from 7.5 °C at the TWI to 2.5 °C at 2.5 m below the TWI, to less than 0.5 °C by 5.5 m deep (Fig 5-3). Comparison of 2013–2014 and 2018–2019 data revealed that average FFT temperatures decreased by up to 2 °C in the upper 5 m of the deposit (Dompierre et al., 2016). In 2013–2014, temperatures measured at the TWI ranged from an annual lake average maximum of 11.8 °C September 2013 to a minimum 8.0 ± 0.2 °C in April 2014 (Dompierre and Barbour 2016). Temperatures at the TWI in 2018–2019 ranged from a minimum of 5.7 ± 0.2 °C in March, 2018, to a maximum 13.8 ± 0.2 °C in August, 2019. Consistent with previous findings, FFT was warmer than the overlying water cap from November through June and cooler than the overlying water cap from July through October (Dompierre et al., 2014; Dompierre and Barbour 2016, Risacher et al., 2018). In 2018, differences between locations at a given depth were greater than lateral variations in temperatures in 2013–2014, with differences up to 3.5 °C at 5.5 m below the TWI between P2NE and P3SW (Fig. 5-3).

Natural ground temperatures at this site are approximately 3° C and consequently it would be expected that in the very long term the tailings would gradually cool to similar temperatures at depth (Dompierre 2017). However, at depths greater than 5 m below the TWI, the temperature profiles were similar from 2018–2019 were slightly cooler than earlier measurements made at P1C and P3SW suggesting that FFT cooling at the top of the deposit is slow and restricted to a shallow interval (Dompierre and Barbour, 2016; Dompierre et al., 2014).

When comparing the average of the measured FFT temperature profiles from 2018–2019 with previously published annual temperature data, the seasonal cycles persists, heating and cooling the water cap which influences the temperatures in the upper FFT (Fig. 5-3; Dompierre and Barbour, 2016). At a given depth, monthly temperature variations increased from <1 °C in 2013–2014 to between 1 and 2 °C in 2018–2019 (Fig. 5-3). Over time the depth that the seasonal cycling influences is increasing as settlement slows with time, limiting convective temperature flow (Dompierre and Barbour, 2017).

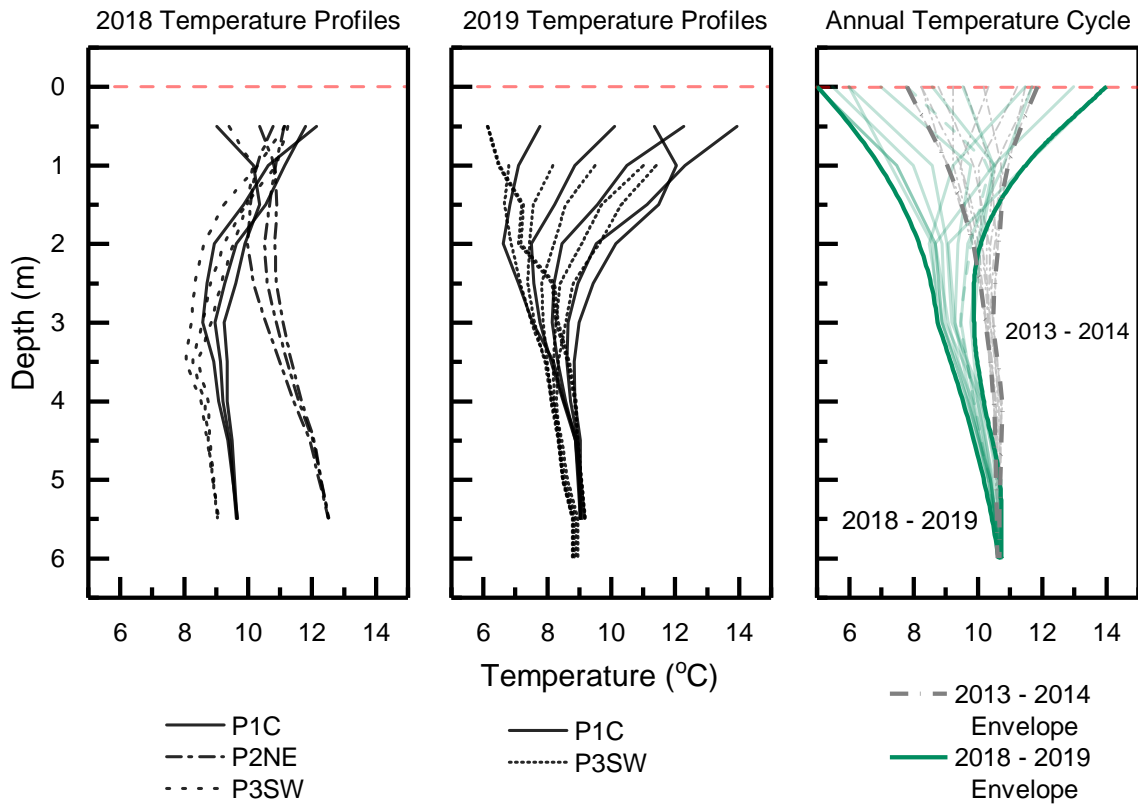


Figure 5-3: Averaged monthly temperature profiles from BML in 2018 (left) and 2019 (center), and whole lake average annual temperature cycle (right). 2013–2014 temperature data comes from Dompierre et al. (2016). The red dashed line represents the TWI.

5.4 Pressure

The fluid pressure (P_{fluid}), at any depth, represents the total weight (per unit area) of the overlying water and solids since the effective stress at these depths is still zero. Effective stress is the difference between total stress and pore-pressure and represents the development of particle to particle stress transfer. The measured P_{fluid} at a given depth equalized rapidly to formation fluid pressures and remained relatively constant following deployment at a given depth, except P2NE in 2019, where the sensors were disturbed during deployment. In contrast, the dissolved gas pressure ($P_{\text{T DG}}$) measured within the samplers increased following deployment from an initial atmospheric pressure as gas pressure within the samplers begins to equalize with the gas pressure within the FFT. The observed $P_{\text{T DG}}$ values gradually approached and, in some cases, exceeded P_{fluid} . The slower response time for the $P_{\text{T DG}}$ sensors is related to the time required for dissolved

gas to diffuse from FFT through the sensor housing and across the semi-permeable membrane. It is expected that differences in the rate of rise in P_{TDG} are due to differences in the dissolved gas concentrations. These differences in dissolved gas concentrations would ultimately be reflected in the differences between P_{fluid} and P_{TDG} at various depths and locations once the P_{TDG} values had stabilized. Therefore, the time required for the difference between P_{fluid} and P_{TDG} to stabilize depended on location and depth in 2018. In general, the rates of rise in P_{TDG} were more rapid at P2NE than at P1C and P3SW.

In 2018, the values of P_{TDG} within the sensors deployed at P1C (1 and 5 m), P2NE (1, 3, and 5 m), and P3SW (5 m) reached a consistent pressure differential reflecting equilibration of the P_{TDG} sensor with dissolved gas pressures (Fig. 5-4). The remaining sensors at P1C (3 m) and P3SW (1 m, 3 m) were still changing upon retrieval. Less than 10 d was required to achieve a stable reading at P2NE, while sensors deployed at P3SW were still changing after more than 55 d. Upon retrieval, sensors deployed at P2NE and P1C exhibited P_{TDG} values in excess of P_{fluid} at all three depths.

In 2019 the differential pressure between ($P_{TDG} - P_{fluid}$) had not reached a constant value upon retrieval. These differential pressures were less negative at P1C than P3SW, and at both locations the highest P_{TDG} values were associated with the sensors deployed at 3 m depth. Pressure differentials were less negative at P1C than P3SW, and the sensor at 3 m below the TWI at both locations had the highest values (Fig. 5-4). Despite apparent differences in P_{TDG} sensor response times between 2018 and 2019, similar differential pressures were observed upon retrieval in both years. A calculation of rates of gas diffusion into the sensors with time highlighted that the longer diffusion path length created in the 2019 sensor housing design substantially increased equilibration times (Appendix B).

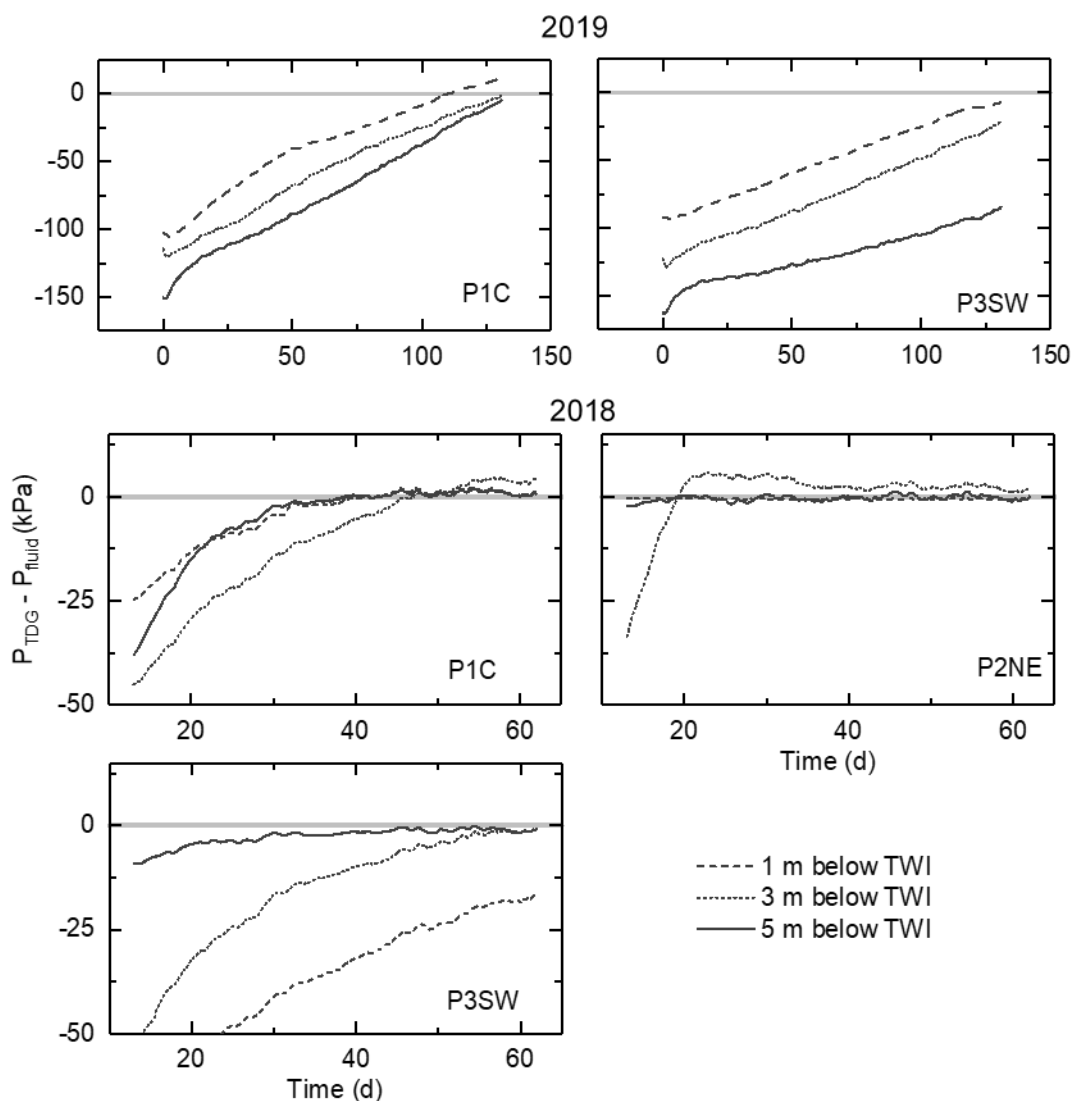


Figure 5-4: Results of summer 2018 fluid and total dissolved gas pressure campaign plotted as the difference between P_{TDG} and P_{fluid} .

5.5 Porewater Chemistry

Most of the geochemical constituents considered in this study (i.e., Cl^- , B, δ^2H , $\delta^{18}O$, CH_4) exhibited the lowest concentrations or, most negative signature in the case of isotopes, values in the water cap. The values sharply increase immediately below the TWI, and remain variably elevated with depth below the TWI. These observations are generally consistent with previously reported values for chemical constituents in BML (Rudderham, 2019, Dompierre et al., 2016). In contrast, the concentrations of dissolved atmospheric NGs (ie., Ne, Ar, Xe, Kr) decreased with

depth below the TWI. The concentration gradients within the FFT decreased with depths until the concentrations became relatively constant at depths 1.0 to 2.5 m below the TWI, depending on the constituent and year studied. Dissolved Cl^- and B concentrations and values of $\delta^2\text{H}$ and $\delta^{18}\text{O}$ are generally consistent with past studies of OSPW and FFT porewater (Dompierre et al., 2016; Allen, 2008; Mackinnon, 2004; Farrell et al., 2004; Kaperski, 2001). Lower concentrations of conservative constituents in the water cap compared to FFT porewater is attributed to dilution of the lake water primarily by pumped in freshwater and precipitation and pumped out lake water for use in upgrading. The values of Cl^- , B, $\delta^2\text{H}$, and $\delta^{18}\text{O}$ within the FFT at depth likely reflect depositional porewater composition whereas $\text{CH}_{4(\text{aq})}$ concentrations likely reflect *in situ* methanogenesis (Arriaga et al., 2019; Rudderham 2019; Risacher et al., 2018). Depletions of non-reactive NGs within FFT is attributed to transport processes (Jones et al., 2014).

5.5.1. Dissolved Cl^- and B

Vertical Cl^- concentration gradients are highest immediately below the TWI and then diminish with depth until they are relatively constant with depth below depths of 0.5 to 2.0 m below the TWI. Dissolved Cl^- concentrations within the water cap decreased from 2013 to 2017, while Cl^- concentrations in the FFT remained relatively consistent between years (Appendix A; Dompierre et al., 2016, 2017). Dissolved Cl^- concentrations reached a maximum between 0.25 and 2.5 m below the TWI depending on location (Fig 5-5; Dompierre et al., 2016). The average concentration of Cl^- in the water cap decreased from 450 mg L^{-1} in 2015 to 420 mg L^{-1} in 2017 due to aforementioned freshwater inputs. FFT porewater Cl^- concentrations range from water cap values near the TWI to between 390 and 1018 mg L^{-1} up to 40 m under the TWI. Over these intervals Cl^- concentrations had an average of $546 \pm 47 \text{ mg L}^{-1}$ in 2016 and $612 \pm 123 \text{ mg L}^{-1}$ in 2017, consistent with median value of 560 mg L^{-1} for 2015 reported by Dompierre et al. (2016). Depth profiles for 2015 reveal a “bulge” in concentrations from 0.5 to 1.0 m below the TWI (Fig. 5-5). This zone of slightly elevated concentrations is not present at P1C and P2NE in 2016, but persists at P3SW from 2015 to 2017. Since bitumen upgrading recycles OSPW, including from WIP, shallow, FFT deposited near the end of BML filling should exhibit higher porewater salinity (Allen, 2008; Dompierre et al., 2016). Over time, transport by upward moving water and diffusion should remove this narrow zone of elevated Cl^- concentrations. However, P3SW has a lower

measured settlement may be insufficient to have this effect on Cl^- concentration profiles. This bulge is also shown in Boron depth profiles at P1C and P3SW, though it is less apparent.

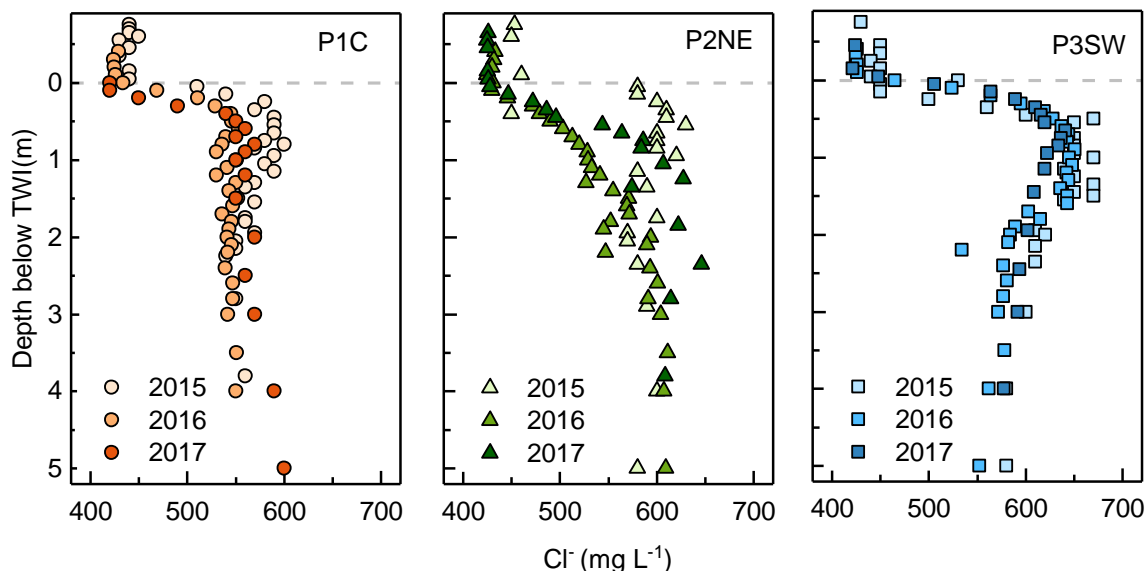


Figure 5-5: Depth profiles of Cl^- at each sampling platform extending down to 5 m. The dashed line represents TWI.

The depth profiles of B were similar to those of Cl^- and generally consistent from 2015 to 2016. Dissolved B concentrations for 2017 samples exhibited similar depth profiles and trends among locations but were approximately 30% higher at all three locations (Fig. 5-5). In 2015 and 2016 dissolved B concentrations in the water cap exhibited a median value of $1717 \pm 255 \mu\text{g L}^{-1}$ increasing across the TWI to a mean of $3240 \pm 941 \mu\text{g L}^{-1}$ between 1.5 m below the TWI and the bottom of the sampled profile (Fig. 5-6). In 2017, the average BML FFT porewater mean B concentration was $3710 \pm 790 \mu\text{g L}^{-1}$. At depths greater than 2.5 m below the TWI, a wider range of B concentrations was observed. Elevated concentrations may be due to changes in sample handling procedures between 2016 and 2017. Concentrations increased with depth at all three locations from the TWI to 5 m below the TWI. Boron concentration depth profiles exhibit a bulge in elevated values in the shallow FFT in 2015, consistent with Cl^- profiles.

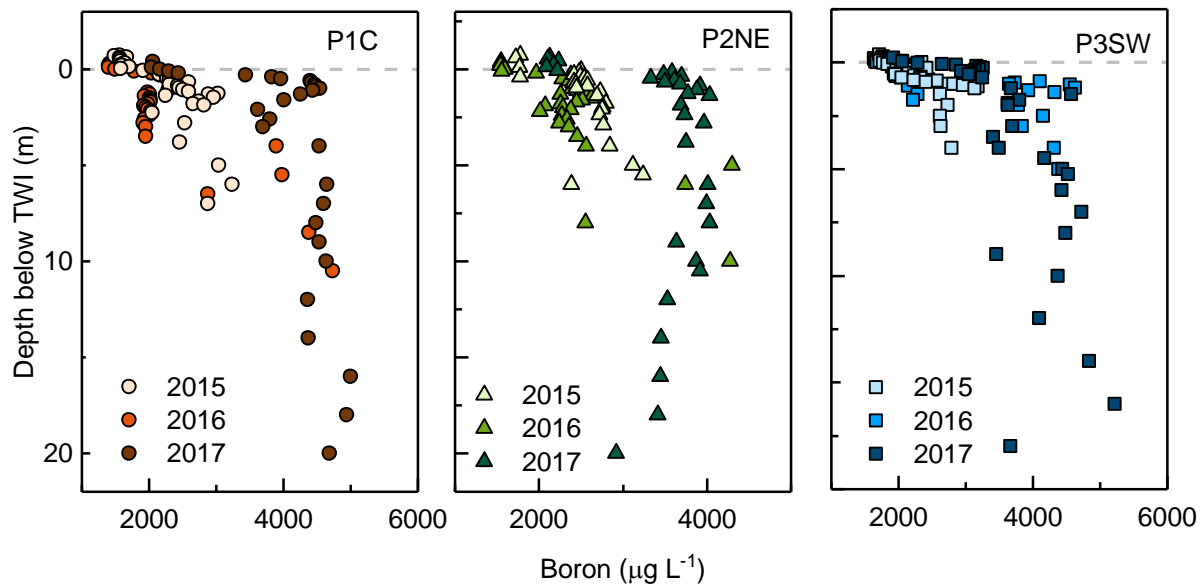


Figure 5-6: Depth profiles of Boron at each sampling platform. The horizontal dashed line represents TWI.

5.5.2. Stable Isotope of Water

Depth profiles of $\delta^2\text{H}$ were highly variable among locations and with depth. Mean water cap values were -113.5 ± 1.7 ‰ with a minimum value of -117.0 ‰; while mean FFT porewater values were slightly less negative at -112.5 ± 2.0 ‰ and a maximum of -109.2 ‰. Depth profiles for $\delta^{18}\text{O}$ showed similar variability to those for $\delta^2\text{H}$. Water cap $\delta^{18}\text{O}$ values averaged -12.4 ± 0.4 ‰ over both years with a minimum of -11.5 ‰. FFT porewater values were similar, averaging -12.3 ± 0.3 ‰ with a maximum of -11.5 ‰. Generally, gradients were more prominent in published 2015 profiles. Depth profiles from 2016 and 2017 exhibit less distinct changes with depth where values are similar above and below the TWI.

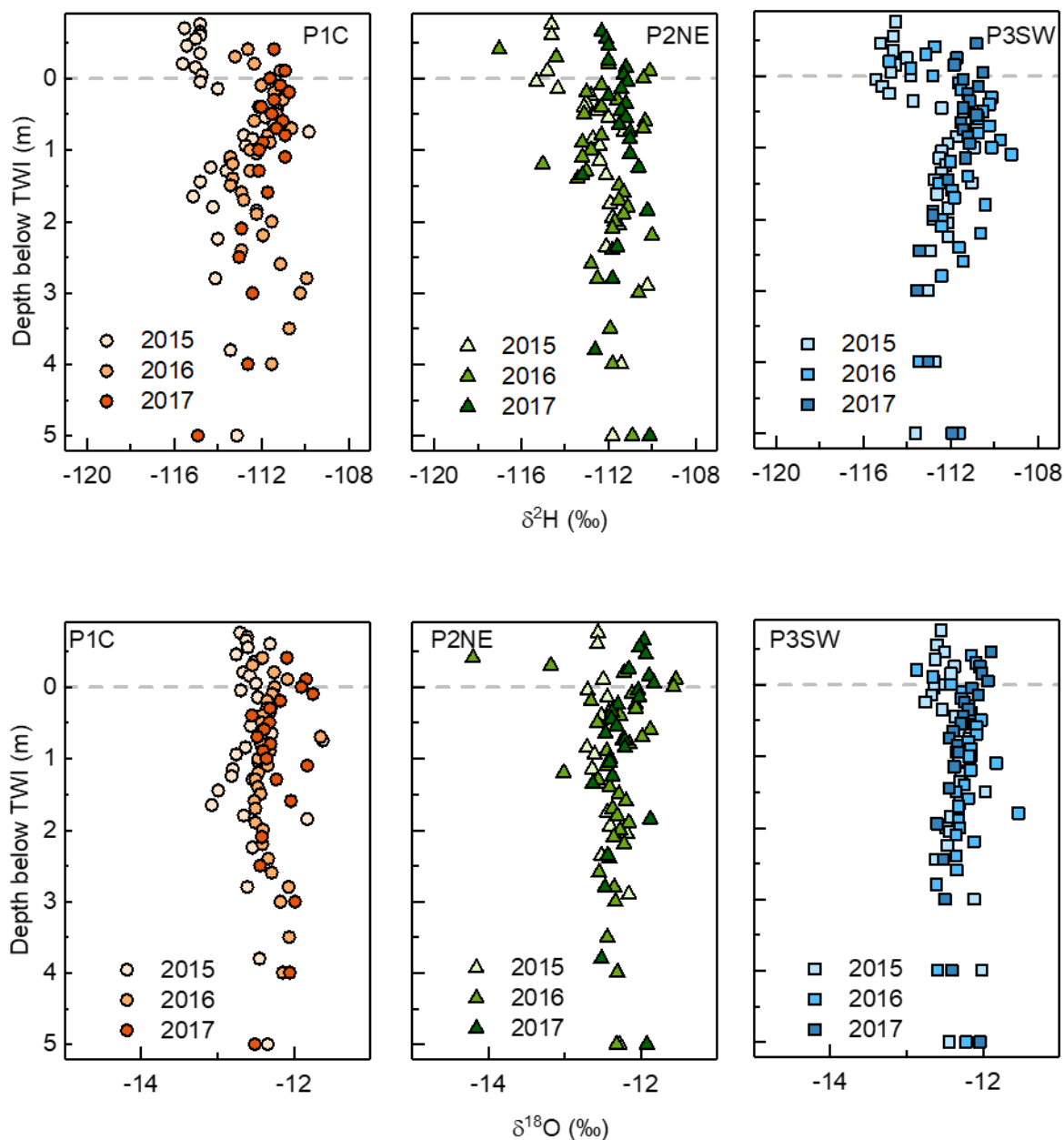


Figure 5-7: Depth profiles of $\delta^2\text{H}$ (top) and $\delta^{18}\text{O}$ (bottom) at each sampling platform normalized to the TWI. The horizontal dashed line represents the TWI.

The presence of $\text{CH}_{4(\text{aq})}$ can affect $\delta^2\text{H}$ measurements (Hendry et al., 2011). However, stable water isotopes may also be affected by changes in the water balance over time including increased evaporation, decreased freshwater inputs, and ongoing FFT dewatering. Freshwater pumping from BCR has decreased by over half since 2013 and the total water cap volume has increased from 24.39 Mm^3 in October 2012 to over 62.16 Mm^3 in October 2016 (Barr Engineering 2017). This

increase in volume means that the influence of depleted local meteoric waters on the water cap decreases over time.

5.5.3. Dissolved Gases

Dissolved CH₄ concentrations sharply increased with depth across the TWI, from below 2 mg L⁻¹ immediately above the water cap, to approximately 45 mg L⁻¹ at 1.5 m below the interface. From 1.5 to 5 m below the TWI, CH_{4(aq)} concentrations exhibit greater spatial and temporal variability. Over this depth interval, P2NE exhibited the highest mean CH_{4(aq)} concentrations (59 ± 10 mg L⁻¹), while P3SW exhibited the lowest mean values (37 ± 13 mg L⁻¹). Mean porewater CH_{4(aq)} concentrations at P1C (47 ± 10 mg L⁻¹) were between the other locations. Deeper CH_{4(aq)} concentrations varied among locations and over time. From 2.5 to 7.5 m below the TWI at P1C, mean CH_{4(aq)} concentrations decreased over time from 45 ± 11 mg L⁻¹ in 2016 to 25 ± 10 mg L⁻¹ in 2019. In contrast, CH_{4(aq)} concentrations at P3SW increased from 45 ± 12 mg L⁻¹ in 2016 to 56 ± 3.8 mg L⁻¹ in 2019 over the same depth interval. Depth profiles obtained at P2NE extended only 4 m below the TWI where concentrations exhibited a wider range from 35 mg L⁻¹ to 79 mg L⁻¹. Despite this spatial and temporal variability, CH_{4(aq)} concentrations remained consistent in the uppermost 2.5 m between all years (Fig. 5-8).

Consistent with CH_{4(aq)}, dissolved CO_{2(aq)} concentrations increase sharply with depth from below 10 mg L⁻¹ at the TWI to approximately 65 mg L⁻¹ at 2.0 m below the TWI. Depth profiles exhibit spatial and temporal variability below 2 m under the TWI with the highest concentrations observed in 2016 in all locations. A large increase in CO_{2(aq)} concentrations over a 1 m interval was observed in varying years at all three locations (Fig 5-8). The lowest and highest location-averaged concentrations were observed at P1C (30 ± 18 mg L⁻¹) and P2NE (average 81 ± 47 mg L⁻¹), respectively, whereas P3SW fell between these values (66 ± 44 mg L⁻¹).

Noble gas concentrations and ratios in FFT porewater decreased with depth below the TWI. Noble gases were highly depleted relative to air saturated water (ASW) at BML. Depth profiles show depletion with depth from the water cap across the TWI down to 2.0 m deep (Fig. 5-9). Relatively light NGs (e.g. Ne, Ar) exhibited greater depletion than heavier NGs (e.g. Kr, Xe; Appendix A)

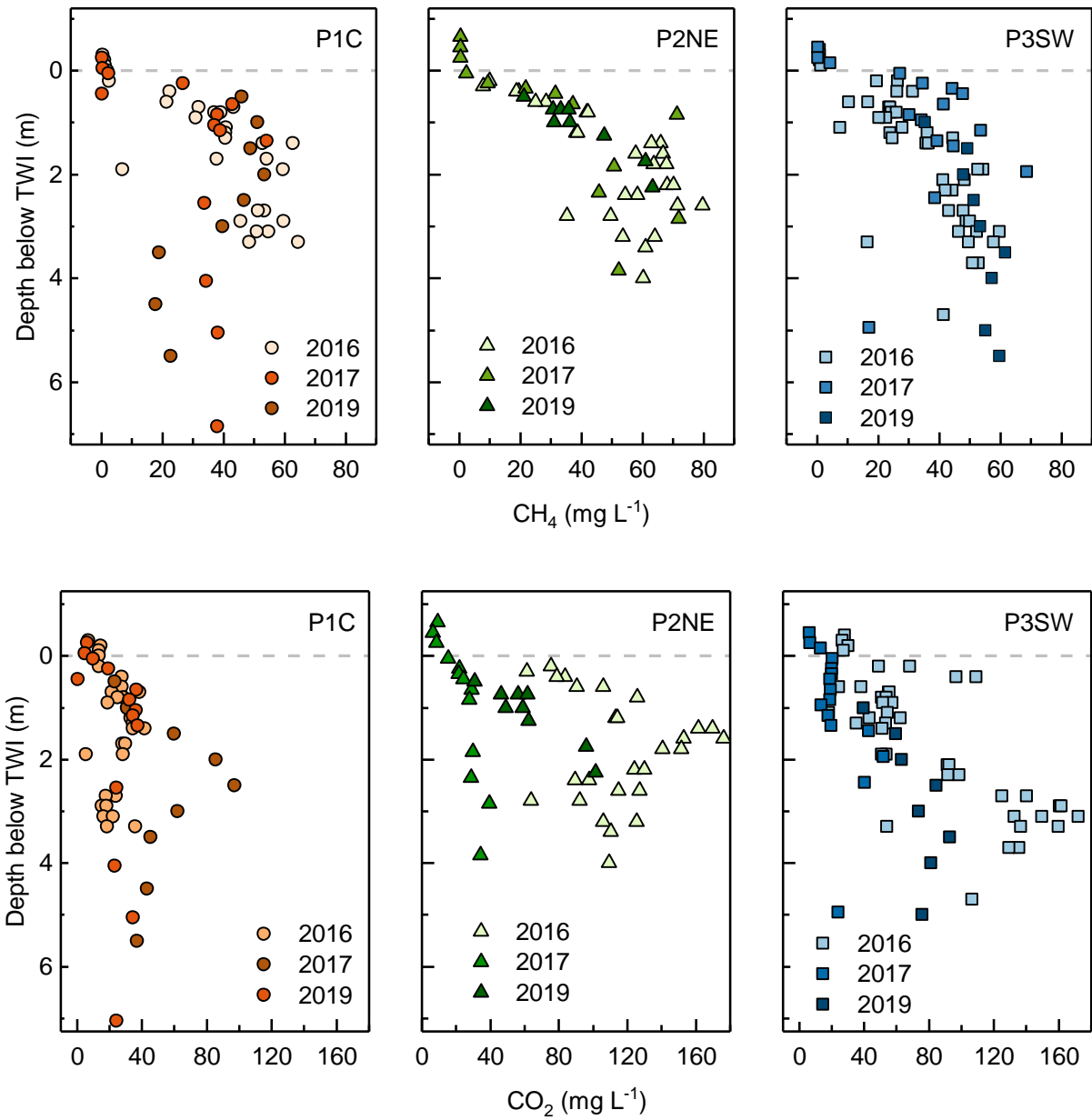


Figure 5-8: Depth profiles of CH_{4(aq)} (top) and CO_{2(aq)} (bottom) depth profiles at each sampling platform relative to the TWI. The horizontal dashed line represents the TWI.

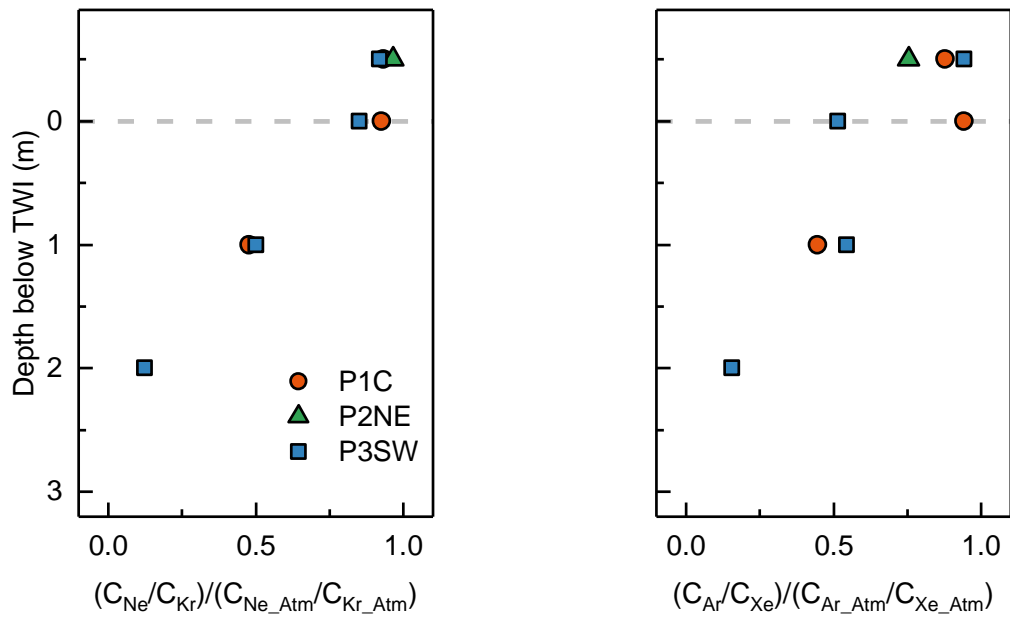


Figure 5-9: Depth profiles of selected noble gas ratios. The horizontal dashed line represents the TWI.

CHAPTER 6: ANALYSIS AND DISCUSSION

This section will examine CH₄ dynamics in BML including distribution, saturation, ebullition potential and potential long-term trends. It will also investigate the influence of ebullition on the conservative mass transport from the FFT in the water cap. Reactive transport models of CH_{4(aq)} are carried out to investigate the influence of consumptive or productive processes on CH_{4(aq)} flux. Finally, two conceptual models are presented, one describes the processes affecting internal mass loading in BML, the other summarizes the interactions of the different parameters and processes influencing CH₄ dynamics in FFT.

6.1 Methane Distribution

The depth profiles of CH_{4(aq)} from the FFT into the water cap are consistent with previous studies focused on BML (Arriaga et al., 2019; Rudderham, 2019; Risacher et al., 2019). Minimal concentrations of CH_{4(aq)} near the TWI and into the water cap are attributed to advective dispersive transport from porewater tailings settlement and CH₄ oxidation, while elevated FFT concentrations at depth are consistent with methanogenesis (Rudderham, 2019; Stasik et al., 2014; Stasik and Wendt-Pothoff, 2016; Foght et al., 2017).

Changes in sampling techniques may account for some of the observed variations in CH₄ concentrations between years. The headspace equilibration method used in 2016 and 2017 may have been impacted by entrained CH₄ bubbles or gas loss during sample collection. The passive *in situ* diffusion method used in 2019 is not affected by these factors. Despite using different methods, the magnitude and spatial trends in CH_{4(aq)} concentrations at individual locations were consistent among all years. Although the passive *in situ* diffusion method produced smoother depth profiles, the results indicate that both methods produce similar results.

Methane production in FFT is controlled by the availability of diluent hydrocarbons (HCs), which include *n*-alkanes, iso-alkanes and monoaromatics associated with residual naphthenic and paraffinic solvents (Kong et al., 2019). Since these compounds are biogenically degraded over time, CH₄ production is likely more prevalent in FFT deposited toward the end of BML filling

(Rudderham, 2019; Siddique et al., 2014; Stasik and Wendt-Pothoff, 2014; 2016). FFT from MLSB is enriched in diluent HCs compared to FFT from SWIP due to the coeval storage with diluent rich FTT in MLSB prior to pumping. The greater available diluent HCs in MLSB sourced tailings could explain the higher concentrations of $\text{CH}_{4(\text{aq})}$ in FFT at P2NE and lower concentrations in FFT at P3SW.

6.1.1. *Dissolved Gas Saturation*

Porewater CO_2 concentrations were approximately were undersaturated through the measured profile (Appendix A-2). The degree of saturation increased with depth away from the TWI up to approximately 2 m where it did not exceed 9% of the saturation concentration. Consequently, CO_2 exsolution was unlikely to drive ebullition within the FFT. Calculated CH_4 saturation thresholds were higher in 2018 compared to 2014 due to the thicker water cap and slightly cooler temperatures in the upper FFT (Fig. 6-1). Resulting CH_4 concentration profiles highlight decreasing temporal variability with depth, corresponding with lower variations in seasonal temperature (Fig. 5-3). The solubility converges to a single value corresponding to the lower limit of seasonal FFT temperature fluctuations by 4 m below the TWI, while solubility continues to increase with depth. The warmest temperatures correspond with the lowest solubilities in each modelled period, consistent with findings from the sensitivity analysis (Fig. 4-5).

Sensitivity analysis of the parameters affecting CH_4 solubility using conditions at BML indicate that temperature and pressure have the greatest effect on CH_4 solubility and, therefore, exsolution (Fig. 4-5; Duan and Mao, 2006; Dompierre and Barbour, 2016; Barr Engineering, 2018). Minimum solubility occurs from August to October when temperatures are warmest in the FFT (Dompierre and Barbour, 2016; Lawrence et al., 2016; Duan and Mao, 2006). This time period would also correspond to higher rates of methanogenesis associated with the higher fluid temperatures (Nozhevnikova et al., 1997). The combined effect of decreasing CH_4 solubility and higher rates of production would likely result in higher rates of $\text{CH}_{4(\text{g})}$ exsolution. The reverse is true in late winter as decreasing temperatures within the upper FFT result in lower rates of production, higher CH_4 solubility limits and consequently, lower rates of exsolution and ebullition.

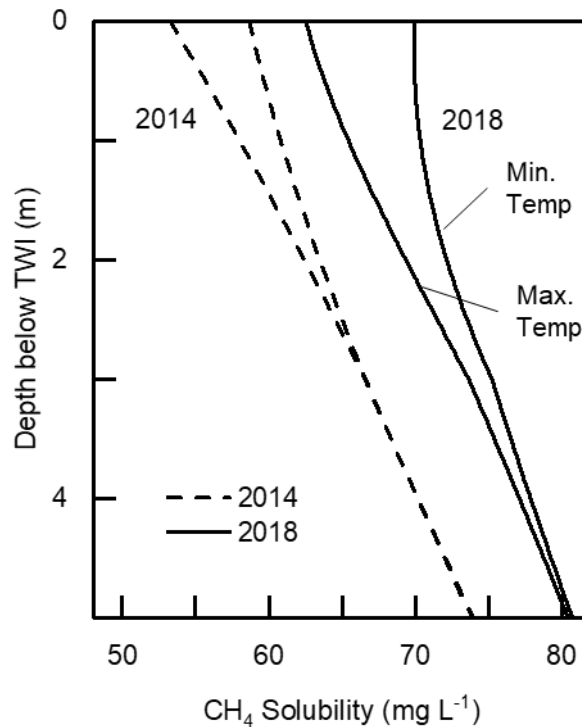


Figure 6-1: Dissolved methane solubility saturation limits for average summer and winter conditions in 2014 and 2018 at BML.

Increasing pressure with depth also increases CH₄ solubility within the FFT (Duan and Mao, 2006). Pressure may also vary over short time-scales (e.g., hours to weeks) due to fluctuating barometric pressure and changing water levels. However, FFT settlement will continue to increase water cap thickness and therefore fluid pressure at a given depth. The water cap has doubled in thickness in some places from 5 m in 2012 to over 12 m in 2019 increasing solubility by as much as 80% at a given depth relative to the TWI (Lawrence et al., 2016; Barr Engineering, 2018). Integrating the long-term trends of the two parameters shows that the CH_{4(aq)} solubility at a given depth in BML is increasing over time (Fig. 6-1).

To better understand CH₄ dynamics in the FFT profile, the degree of saturation associated with each measured CH₄ concentration was calculated based on the solubility conditions in late summer using the method of Duan and Mao (2006; Fig. 6-2). Methane solubility was calculated using FFT temperatures measured for individual samples (2016 and 2017) or the warmest recorded temperature profiles (2019). The measured CH_{4(aq)} concentrations were well below theoretical

saturation in the water cap and near the TWI, consistent with dilution by mixing with surface waters and depletion by oxidation (Arriaga et al., 2019; Goad, 2017; Rudderham 2019; Risacher et al., 2018). The degree of CH₄ saturation increased with depth, approaching or reaching the solubility limit at depths of 1.5 to 2 m below the TWI (Fig 6-2). Methane saturation persisted to between 2 and 3 m below the TWI. Below this zone, CH₄ concentrations remained relatively constant while solubility increased, resulting in a decrease in the degree of CH₄ saturation. Four CH_{4(aq)} concentrations exceed the modelled CH₄ saturation limit from 2017 and 2016 which may be indicative of the presence of entrained CH₄ bubbles within the sampled FFT (Fig. 6-2).

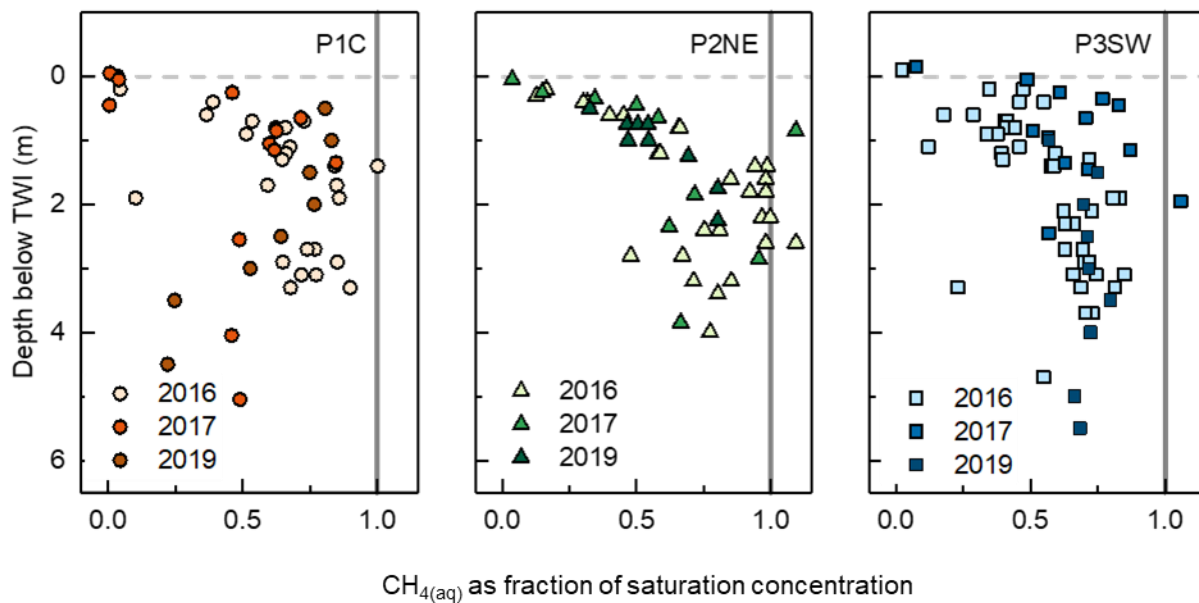


Figure 6-2: Dissolved CH₄ concentrations plotted as a fraction of modelled solubility by sampling location and year. Horizontal dashed line represents the TWI.

Methanogenesis is an ongoing process that likely occurs throughout the entire FFT deposit at variable rates. If methanogenesis were temporally discontinuous, continuing advective-dispersive transport and oxidation would remove any elevated concentrations in porewater. A depth interval from 1.5 m to 3 m over which near CH₄ saturation persisted during the sampled period at P1C and P2NE, indicates that methanogenesis was enhanced through this zone. Without ongoing methanogenesis, the degree of CH₄ saturation should have declined concomitant with increasing solubility.

Deeper FFT is depleted in residual diluent HCs, which are degraded to a carbon source for methanogenesis and, therefore, may contribute less to overall CH₄ production (Stasik et al., 2015; Siddique et al., 2012). This depletion of available carbon for acetoclastic methanogenesis, identified as the primary methanogenic pathway, may account for the undersaturation observed below 3 m below the TWI (Goad 2017; Rudderham, 2019). Rudderham (2019) noted relative increases in populations of methanogens that use the hydrogenotrophic pathway in deeper FFT. This change in population may reflect a change in available carbon source. This pathway, while possible, is thermodynamically less favourable (Rudderham, 2019; Goad, 2017; Nozhevnikova et al., 1997).

Carbon cycling in FFT is an intertwined process that involves multiple steps before methanogenesis occurs which may be enhanced or inhibited by sulfur or nitrogen cycling (Rudderham, 2019; Stasik and Wendt-Pothoff, 2016; 2014; Stasik et al., 2014). Sulfate reducing bacteria may consume CH₃CHOO⁻_(aq) to generate CO₂, thereby inhibiting methanogenesis, or oxidize CH_{4(aq)} in oil sands tailings ponds (Holowenko et al., 2000; Ramos–Padron et al., 2011; Siddique et al., 2012). The nitrogen species NO₂⁻ and NO₃ can be used as electron acceptors in anaerobic methanotrophy (Beal et al., 2008; Luo et al., 2018). Dissolved ammonia, likely as NH₄⁺, is found in FFT porewater but the species associated with CH₄ oxidation, NO₂⁻ and NO₃, are only observed in low concentrations in the water cap of BML (Dompierre et al., 2016; Rudderham, 2019). Depth profiles of SO₄²⁻_(aq) in BML show a sharp drop in concentrations immediately below the TWI from 177 mg L⁻¹ to a mean of 13 mg L⁻¹ (Dompierre et al., 2016; Rudderham, 2019). This suggests, consistent with findings by Rudderham (2019), that nitrogen species likely don't influence CH₄ dynamics in BML, however, sulfur cycling may influence dissolved CH₄ in the uppermost FFT.

6.1.2. Methane Ebullition

Results from CH₄ saturation modelling, NG analysis, and gas pressure surveys can be used to inform the ebullition potential in BML. These methods suggest that ebullition is possible throughout a narrow, 1 to 1.5 m thick zone of FFT ~1–2.5 m below the TWI (Fig. 6-1; 5-9; 5-4). Solubility modelling and pressure surveys indicate greater potential for ebullition in P2NE and P1C compared to P3SW.

The NG results show substantial depletion of all NGs, particularly with lighter NGs relative to the heavier NGs compared to ASW (Fig. 5-9). Preferential depletion of lighter NGs relative to heavy NGs can indicate stripping by partitioning into an existing gas phase (Amos et al., 2005; Jones et al., 2014). The preferential depletion of lighter NGs in BML with depth is similar to a studied CH₄ producing site in Minnesota where gas exsolution and ebullition was identified as the primary cause of the NG depletion there (Fig. 6-3, Jones et al., 2014).

The gas and fluid pressure sampling results are broadly consistent with the measured CH₄ concentrations and the calculated CH₄ solubility. Both the pressure surveys and CH₄ saturation show greater potential for ebullition at P2NE and P1C compared to P3SW. However, all sensor pairings including the deepest sensor pairing at 5m below the TWI in both P1C and P2NE showed that P_{TDG} approached or exceeded P_{fluid}. Since the P_{TDG} sensor records the sum of partial pressures, and therefore may be influenced by the presence of other dissolved gases, it may slightly overestimate the potential for CH₄ exsolution compared to solubility modelling. Though CH₄ makes up the majority of the dissolved gases, dissolved CO₂ is also present in the FFT porewater (Rudderham 2019).

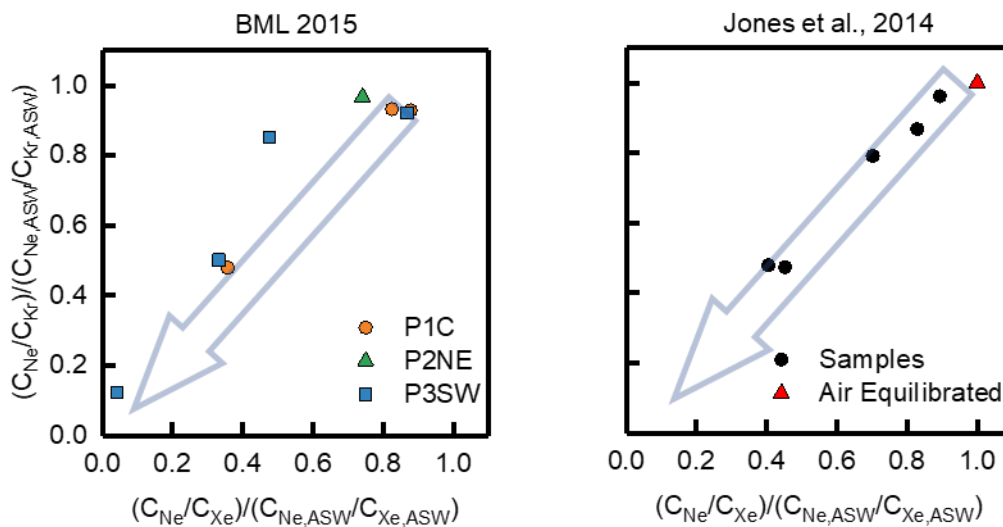


Figure 6-3: Comparison of 2015 BML noble gas ratios with data from Jones et al., (2014).

While the different methods all indicate that gas exsolution is possible, the potential ebullition is less well constrained. Ebullition is controlled by both bubble formation and the ability of the bubbles to move up through the FFT. Bubble transport requires that buoyancy forces on the

bubble exceed forces associated with shear strength and viscosity. In some cases, it is likely that bubbles remained trapped within the FFT until some perturbation in the confining forces occurs as a result of disturbance of the FFT after which there are episodic bubbling events (Dompierre and Barbour 2016; Scandella et al., 2011; 2017). These perturbations may be an initial bubble release or changes in the confining fluid pressure from things lateral currents reducing shear strength (Joyce and Jewell, 2003; Sirhan et al., 2019). For example, if the water cap decreases in elevation due to drawdown or evaporation, then the confining pressure can release trapped bubbles from the tailings similar to observations in reservoir drawdown events (Harrison et al., 2017). Conversely, settlement and dewatering increases FFT the confining pressure and the yield strength with it.

6.1.3. *Long-Term Trends*

Methane dynamics in BML and other EPLs will be affected by long-term changes in temperature, pressure, and production related to ongoing EPL development. Based on trends in these processes currently observed, CH₄ ebullition will decline over time, ultimately, flux will be dominated by diffusion. Changes in temperature, pressure and available labile organic carbon will influence this decrease in ebullition by increasing CH₄ solubility, increasing storage capacity and lowering CH₄ production. In addition, long term cooling of the FFT combined with increasing lake depth over time will continue to increase the CH₄ solubility within the FFT.

Easily degraded diluent HCs that become the carbon source for methanogenesis may become depleted over time, leading to a decrease in the rates of methanogenesis (Rudderham 2019; Stasik and Wendt-Pothoff 2016). This trend has already been noted with depth in BML which is analogous to time (Stasik et al., 2015; Foght et al., 2017). As the majority of available organics are consumed, the carbon cycle may be altered decreasing the rates of acetoclastic methanogenesis. While this may be taken up by hydrogenotrophic methanogenesis, it is unclear what impact this will have on CH₄ production rates. (Rudderham, 2019).

Seasonal temperature changes will continue to induce temperature fluctuations in the upper FFT, continuing to lower solubility in the late summer/early autumn and increase solubility in late winter and spring (e.g. Duan and Mao, 2006; Delsontro et al., 2010). The depth of penetration of the seasonal variations could continue to increase into the FFT as advection continues to slow. Mass transport will shift to a diffusion dominated setting with slowed settlement, altering CH_{4(aq)}

transport (Carrier et al., 2007; Dompierre and Barbour, 2016). The timing of this shift may be variable in BML but may only be on the order of years as both P3SW and P1C are exhibiting slowed settlement rates (Fig. 5.2).

Since FFT under 3 m below the TWI tends to be undersaturated, this creates a potential reservoir for longer term $\text{CH}_{4(\text{aq})}$ storage. Currently, advection works to transport $\text{CH}_{4(\text{aq})}$ upwards out of the FFT into the water cap. In a diffusion dominated setting, CH_4 would diffuse outwards above and below into the undersaturated FFT. Eventually, continuous CH_4 production could see the majority of FFT profile CH_4 saturated. Continual FFT dewatering will increase pressure and the total solubility. However, the pressure increases are tied to settlement and will decrease in magnitude with time. Fluctuations in the pressure and yield strength of the overlying sediments could induce a mass ebullition event in the lake if the FFT remains CH_4 saturated (Harrison et al., 2017).

Decreasing ebullition has implications for long term greenhouse gas emissions and water cap quality. Currently, CH_4 oxidation is a major O_2 consuming process in the water cap. The $\text{CH}_{4(\text{aq})}$ contribution from dissolution from expressed bubbles into the water cap has not been published, however, it may be a significant component along with mass loading from the FFT. Dissolved CH_4 transported upwards will continue to be oxidized both aerobically in the water cap and anaerobically in the uppermost FFT. Mass loading of CH_4 into the water cap will become dominated by diffusion across the TWI, impacting the rates of O_2 consumption, potentially decreasing the overall O_2 loss in the water cap. Methane ebullition from the FFT dominates the CH_4 flux to the atmosphere from BML, should ebullition decrease, then the total greenhouse gas emissions from BML may decrease as well.

6.2 Transport of Conservative Constituents

Chloride was used as a conservative tracer to develop a transport simulation in a similar manner to that developed previously by Dompierre et al., (2017). Dompierre and Barbour (2016) also utilized $\delta^2\text{H}$ and $\delta^{18}\text{O}$ for conservative species transport; however, given the degree of scatter in the data; and the lack of a distinct trend after 2015 these tracers were not simulated in the current study. Rather, B was selected as a second conservative constituent since it had distinct trends across the uppermost FFT profile in all the sampled years. A constant ratio of 0.65 was used to

adjust 2017 B depth profiles to make these concentrations consistent with the preceding years data. Possible reasons for the difference in the 2017 B profiles from the previous B data was discussed in section 5.5.1.

Calculated upwards advection from measured settlement shows a continuously decreasing flow similar to settlement as predicted by early consolidation models (Carrier et al., 2007; Fig. 6-4). These settlement rates also vary by platform with FFT at P2NE exhibiting the highest rates while P3SW had the lowest rates. Based on settlement data from Barr (2018), settlement rates at P1C decreased from 1.3 to 0.7 m a⁻¹ from 2013 to 2017. Over the same time, these rates fell from 1.9 to 0.7 m a⁻¹ at P2NE and 0.95 to 0.6 m a⁻¹ at P3SW.

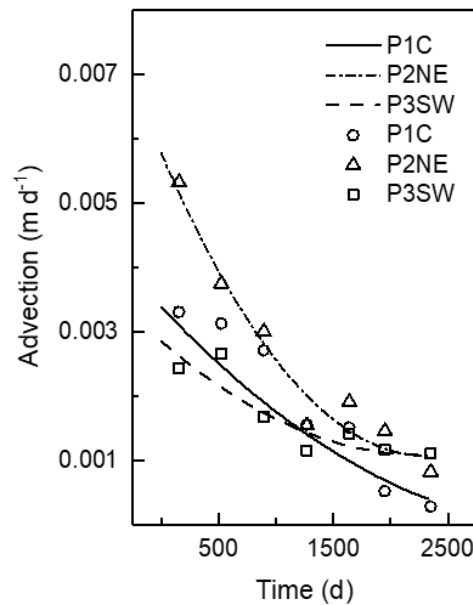


Figure 6-4: Plot of calculated upwards advection based on measured TWI elevations (points) and modelled elevations (lines).

The previous work by Dompierre and Barbour (2016) and Dompierre et al., (2017) found that advective-dispersive transport alone could not simulate the observed depth profiles for conservative constituents (Dompierre and Barbour, 2016; Dompierre et al., 2017). Without some enhanced mixing process in the upper 0.25 – 1.5 m of the FFT profile, the transport models produced Cl⁻ concentrations that were higher than those measured. This was confirmed with the field measurements and modelling undertaken in this study as well. The enhanced mixing simulated in the current study was based on the findings from CH₄ concentrations, gas pressures

and noble gas measurements that ebullition was occurring within the upper 3 m of the FFT profile. The enhanced mixing likely caused by ebullition was replicated by increasing the coefficients of diffusion over the upper meter by a factor of 2.5x, 10x or 25x the values that would have been estimated based on the relationships between porosity and the coefficient of molecular diffusion established by Boudreau (1996; Table 4-1). From 1 to 2 m below the TWI, the coefficient of diffusion was only enhanced by 60% of the change in the top 0 to 1 m below the TWI. The smaller magnitude diffusion coefficient enhancement in the lower 1 to 2 m depth interval was to reflect the smaller and less intense mixing at depth as bubbles increase in size as they rise (Scandella et al., 2011; 2017; Sirhan et al., 2019). As ebullition is tied to CH₄ exsolution, the enhanced mixing was only applied to periods of low solubility and greater rates of methanogenesis in the from June to November of each year in the modelled period. It is important to note that the selection of these enhanced diffusion coefficients was based on a trial and error approach to identify the amount of increase in diffusion coefficient required to enable the simulation to envelope the majority of the observed concentration profiles.

The amount of ebullition required to simulate observed depth profiles varies by location. Locations with greater ebullition potential and higher settlement required more diffusion enhancement to reproduce observed depth profiles (P2NE), while sites that had less ebullition potential were better simulated by primarily advective dispersive transport (P3SW). The goodness of fit for the simulation model curves to the data was determined by calculating the root mean square error (RMSE) for each modelled curve relative to the measurements (Table 6-1). The best fit for Cl⁻ data was the 10x diffusion coefficient model run at P1C for all modelled years. P2NE was best simulated by the 25x diffusion coefficient, except for 2015 (Fig. 6-6). P3SW could not be simulated by any of the models using the observed settlement rate. Decreasing the settlement rate to a constant rate of 0.2 m a⁻¹ produced a good fit to 2016 and 2017 Cl⁻ profiles when a 2.5x diffusion coefficient was used (Fig 6-6; Table 6-1). Measured 2015 Cl⁻ values fell between the base case and the 2.5x diffusion coefficient (Fig. 6-6). Using the same models to simulate the B profiles provided a reasonable fit, particularly at the P1C and P2NE profiles (Fig. 6-7). P3SW profiles for Boron did not fit as well due to large scatter and variance in the data.

Plots of Cl⁻ mass flux rates were generated to examine the influence that greater diffusion coefficient enhancement would have on the mass rate from the FFT in the water cap (Fig. 6-8). As

mass flux is a function of advective dispersive transport, P2NE, with the greatest settlement rates had much higher mass flux than the P1C and P3SW. P1C had a mean flux of $0.21 \pm 0.04 \text{ g d}^{-1} \text{ m}^{-2}$, P2NE had a mean flux of $0.62 \pm 0.03 \text{ g d}^{-1} \text{ m}^{-2}$, and P3SW had a mean of $0.19 \pm 0.04 \text{ g d}^{-1} \text{ m}^{-2}$. The more that the diffusion coefficient was enhanced the greater the mass flux expressed into the water cap during the bubbled periods but, conversely, had lower mass flux in the periods when no ebullition was applied.

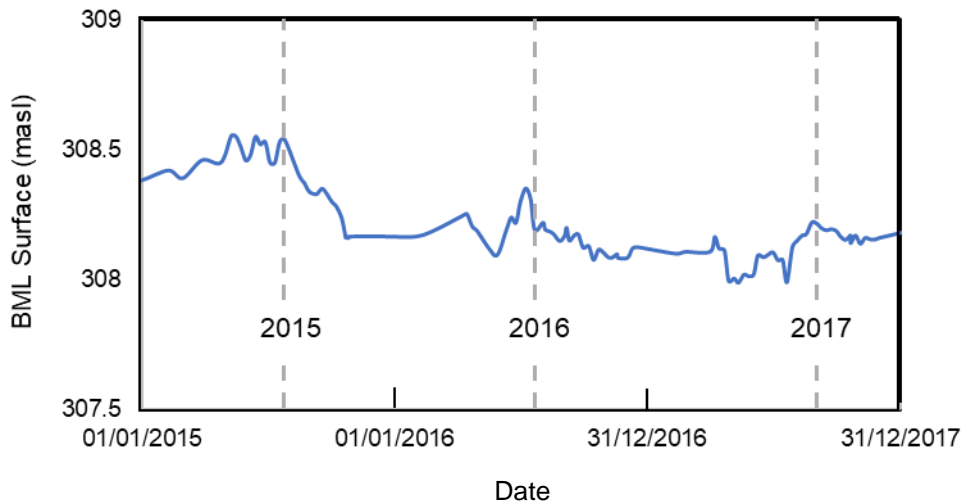


Figure 6-5: Plot of BML surface water elevation over time. The grey dashed lines indicate sampling times at P2NE.

The P2NE 2016 Cl^- depth profile has a much greater depth interval over the which Cl^- concentrations increase from water cap values to FFT values compared to other locations and years (Fig. 6-6). This may be due to induced bubbling events by water level fluctuations. It has been established that small changes in the confining pressure on saturated sediments can cause ebullition events (Harrison et al., 2017). During the 2016 sampling period, FFT at P2NE was sampled just after a water level drop of approximately 0.5 m, whereas FFT at both P1C and P3SW had been sampled before the water level fluctuations (Fig. 6-5). This may explain the much greater depth interval over which gradient in the 2016 depth profile for Cl^- that could not be modelled here.

Anomalous depth profiles at P3SW may be due to settlement rates lower than the apparent values suggested by the annual surveys and FFT sampling (Barr Engineering 2018). For example, it is possible that the measured FFT elevations at P3SW and perhaps elsewhere in BML are influenced by multiple processes rather than solely settlement. Lateral sediment flows within the

FFT as it settles at different rates are possible due to the low shear strength (Dompierre and Barbour 2016). P3SW is also near the inflow from BCR, where higher water velocities may have caused erosion of the uppermost FFT near the pump (Lawrence et al., 2016). Both of these processes could mimic the effect of settlement when studying TWI elevation changes, leading to overestimating the advection rate. One way to check if the uppermost FFT at this location was being removed rather than settling is to compare the solids content data between locations. Locations where erosion is likely should have a lower VWC closer to the TWI than a typical FFT profile. However, VWC profiles are relatively consistent between locations and years, this may be due to expansion of the FFT from unloading, limiting the impacts on VWC (Fig. 5-1; Dompierre et al., 2016; Dompierre and Barbour 2016).

Table 6-1: RMSE for each modelled profile with different simulated ebullition rates of Cl^- (top) and Boron (bottom). The smaller the number the better the fit of the data.

Cl^-	P1C			P2NE			P3SW		
	2015	2016	2017	2015	2016	2017	2015	2016	2017
No Ebullition	19.5	24.0	42.0	37.5	65.7	73.0	25.2	24.5	19.6
2.5x	17.4	25.5	39.6	28.0	62.1	64.5	32.6	24.2	15.9
10x	15.1	13.7	32.3	20.6	48.8	39.7	55.1	46.5	54.0
25x	33.2	16.2	40.6	31.1	32.3	23.7	78.9	73.0	87.7
Boron	P1C			P2NE			P3SW		
	2015	2016	2017	2015	2016	2017	2015	2016	2017
No Ebullition	600.2	398.4	484.1	256.3	446.6	656.9	292.6	882.5	212.3
2.5x	590.5	392.2	435.1	264.4	429.6	584.3	339.6	916.4	253.0
10x	538.5	386.7	302.9	278.9	48.8	460.3	349.0	915.0	317.7
25x	491.2	546.1	319.5	314.2	32.3	427.9	373.3	926.9	414.3

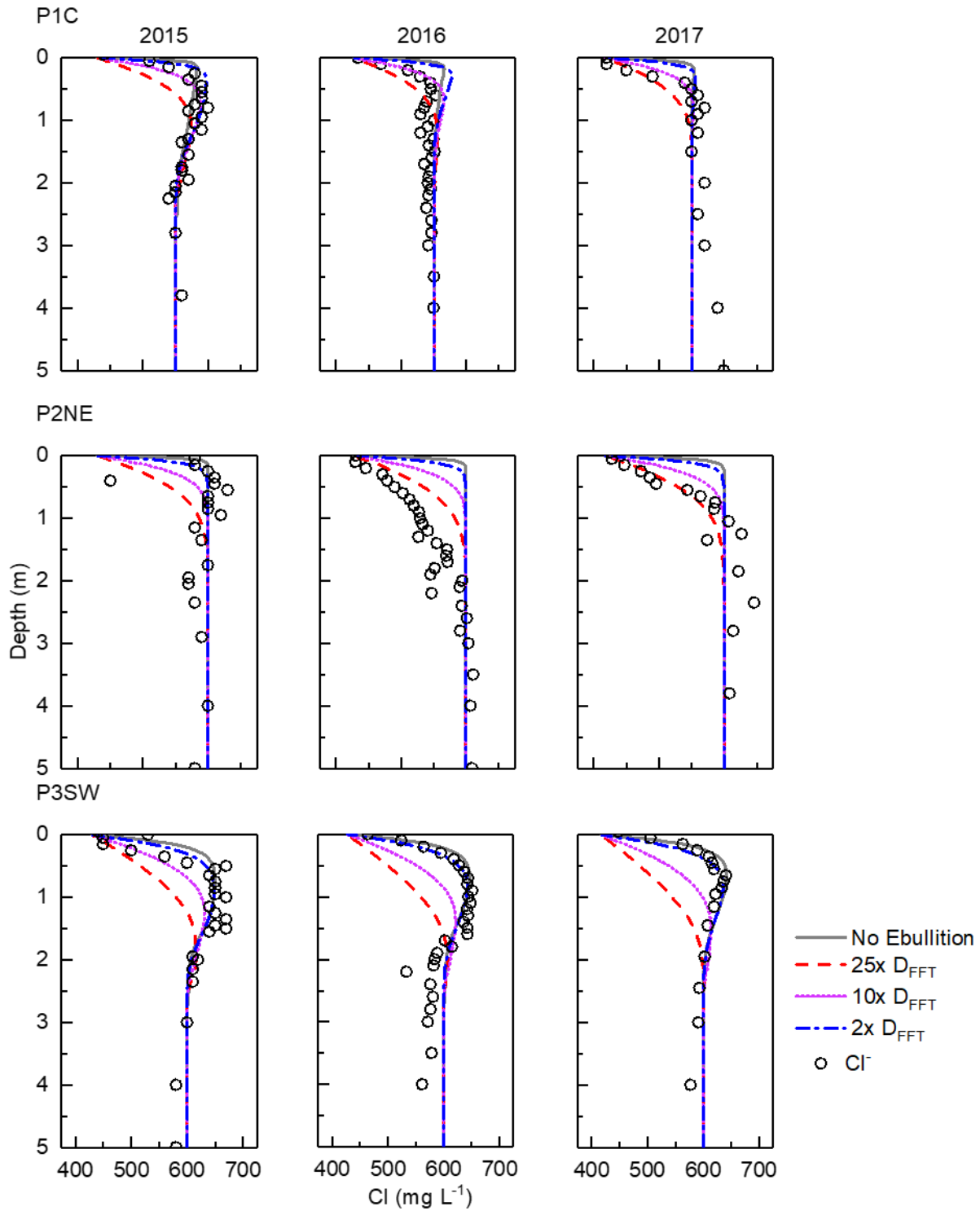


Figure 6-6: Mass transport model profiles and observed concentrations for Cl^- depth profiles by year and location extending to 5 m below the TWI.

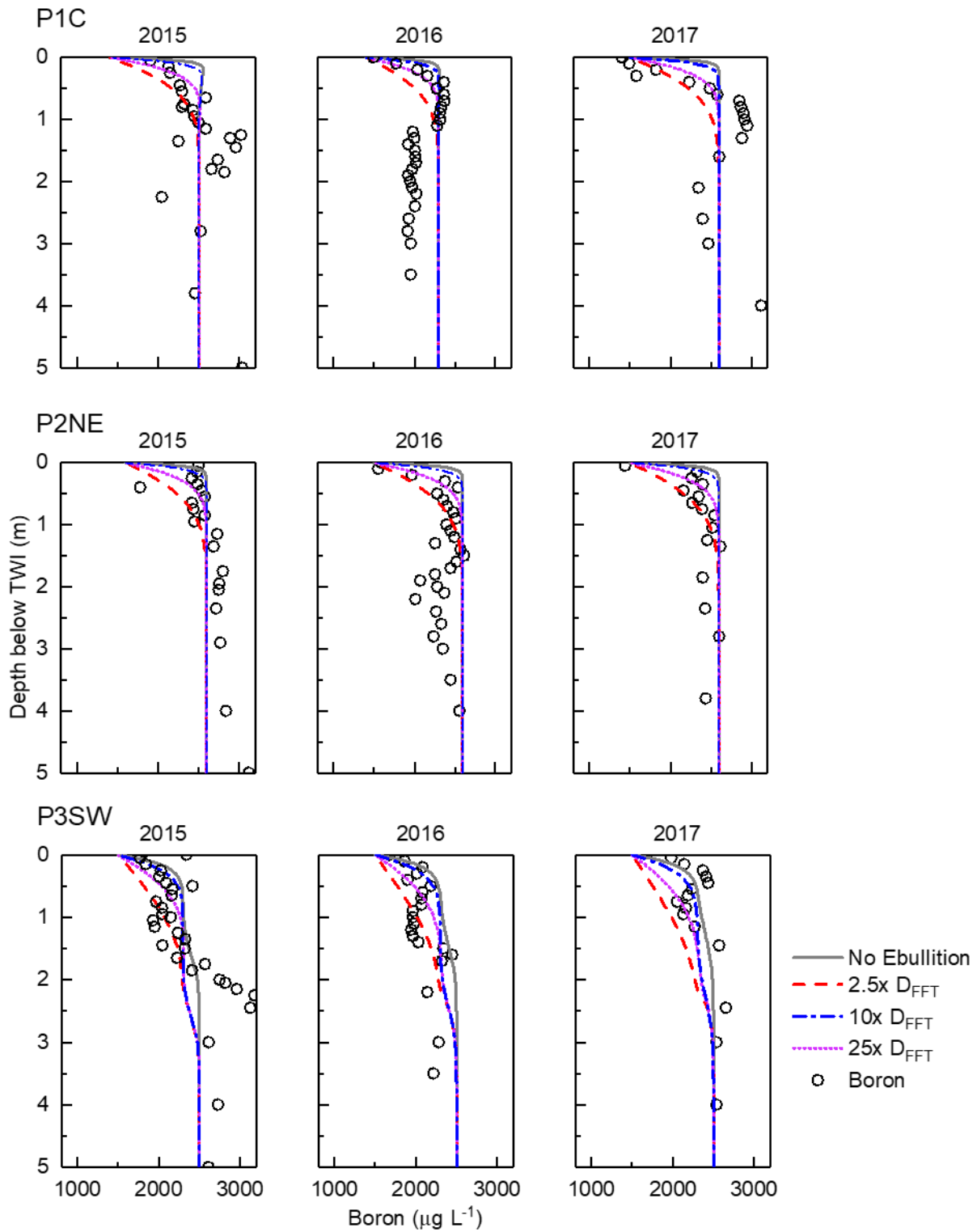


Figure 6-7: Mass transport model profiles and observed concentrations for boron depth profiles by year and location extending to 5 m below the TWI.

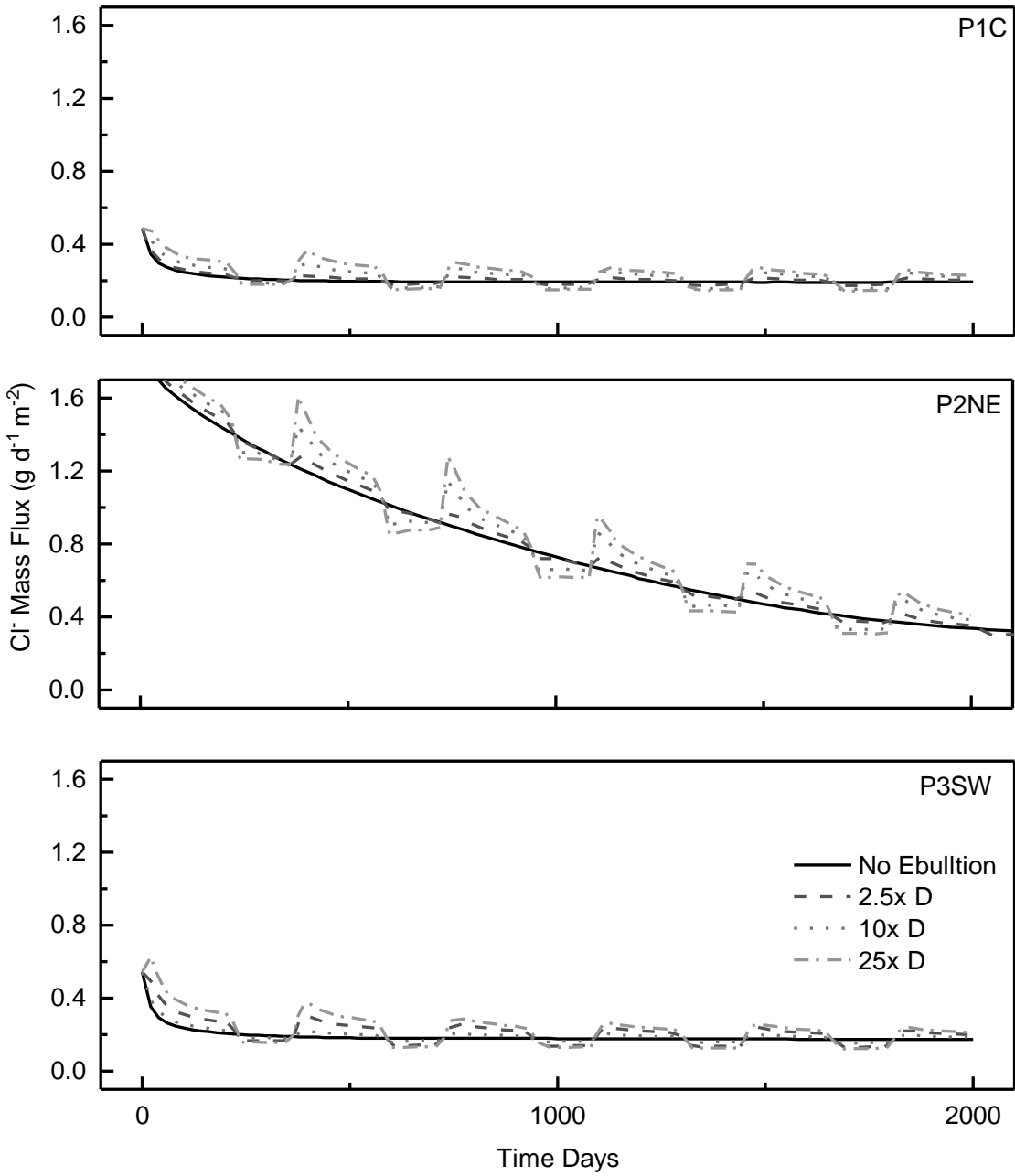


Figure 6-8: Timeline of $\text{Cl}^-_{(\text{aq})}$ mass flux rate from the FFT into the water cap for the differing amounts of ebullition simulated in the transport models over the modelled period.

6.3 Transport of Dissolved CH₄

After developing viable conservative transport models using ebullitive mixing, simple reactive terms were incorporated into the conservative transport models to simulate CH₄ concentration profiles across the tailings-water interface. The conservative transport models help to constrain the primary two controls on transport; the advective water flow rate (i.e. FFT settlement) and the enhanced diffusion created as a result of ongoing ebullition.

Simple reactive transport models of CH_{4(aq)} show a negative flux was required in the upper 1.0 to 2m of FFT above the zone of saturation (Fig. 6-9). Constant consumption rates of $-0.025 \text{ g d}^{-1} \text{ m}^{-2}$ (P1C), $-0.030 \text{ g d}^{-1} \text{ m}^{-2}$ (P2NE) and $-0.0225 \text{ g d}^{-1} \text{ m}^{-2}$ (P3SW) were applied across the uppermost 1 m, 1.5 m and 2.0 m, respectively, of the modelled profiles. These rates are typically 100 to 1000 times higher than anaerobic oxidation rates reported in various freshwater lakes and reservoirs which can range from 9×10^{-5} to $2 \times 10^{-4} \text{ g m}^{-2} \text{ d}^{-1}$ (Barbosa et al., 2018; Deutzmann et al., 2014; Geulin et al., 2007; Saarela et al., 2019). However, introduction of aerobic oxidizers may account for some of the discrepancy the presence of which was report by Rudderham (2020). Some reported aerobic CH₄ oxidation rates can reach $0.080 \text{ g m}^{-2} \text{ d}^{-1}$ (Oswald et al., 2016; Schubert et al., 2010). Simulations of CH_{4(aq)} transport and consumption provided good fits for the 2016 data, whereas larger differences were noted the between model output and 2017 data. Goodness of fit was determined by RMSE calculations (Table 6-2). No modelled profiles for 2019 at P2NE are presented as the sampler array did not deploy to the correct depth. P1C was best simulated by no consumption in 2016 and 1.0 m of consumption for both 2017 and 2019. CH_{4(aq)} depth profiles at P2NE were best fit by 1.5 m of consumption in both 2016 and 2017. P3SW CH_{4(aq)} concentrations showed the greatest variability between years, 2016 concentrations were best fit by 1.5 m of consumption while 2017 and 2019 were best fit by 1.0 m of consumption. 2017 CH_{4(aq)} concentrations had generally lower fits at all platforms compared to 2016. (Fig. 6-9).

Table 6-2: RMSE for each CH_{4(aq)} modelled profile with different simulated CH_{4(aq)} consumption rates. The smaller the number the better the fit of the data.

CH _{4(aq)}	P1C			P2NE		P3SW		
	2016	2017	2019	2016	2017	2016	2017	2019
No Consumption	9.25	20.07	16.31	9.27	19.50	14.40	20.05	9.74
1.0 m	9.38	9.68	12.05	7.61	16.11	10.21	17.41	9.28
1.5 m	9.77	14.55	16.61	7.31	13.15	6.85	17.57	11.01
2.0 m	12.05	13.04	17.43	9.84	10.79	9.83	19.52	17.49

The consumption rate term applied to the model is largely attributed to aerobic oxidation reported as possible in the FFT by Rudderham (2019) in the upper FFT, though this does not preclude the occurrence of anaerobic oxidation. Results of these preliminary models suggest that oxidation may substantially decrease the CH_{4(aq)} flux across the TWI. The aerobic methanotrophs *Methyloparacoccus* and *Methylobacter*, belonging to the class *Gammaproteobacteria*, were found in relatively high counts in FFT immediately below the TWI and in some settings have been found to be active under anoxic conditions (Rudderham, 2019; Martinez-Cruz et al., 2017; Oswald et al., 2016). Additionally, different microbial communities capable of anaerobic oxidation by using NO₃ and NO₂ as electron donors have been identified (Rudderham, 2019; Ettwig et al., 2009; Knittel and Boetius, 2009). The microbial communities *Desulfosarcina* and *Desulfococcus*, associated with anaerobic methanotrophs that can use SO₄²⁻ species as electron donors, were also identified. NO_{3(aq)} and NO_{2(aq)} concentrations are commonly below detection in both the water cap and FFT porewater with only scattered measurable values (Rudderham 2019). Dissolved SO₄²⁻ is abundant near and above the TWI and persists in minor amounts (13 mg L⁻¹) up 5 m below the TWI. Given that CH₄ saturation is reached by 1.5 to 2.0 m below the TWI, the interval between this zone and the TWI could host anaerobic oxidation. Based on abundances of both constituent and microbial communities identified, both anaerobic and aerobic oxidation are likely restricted to the upper FFT (Rudderham, 2019; Dompierre et al., 2016).

The CH_{4(aq)} consumption rate from the FFT into the water cap varies on an annual basis, similar to conservative transport models and is tied to the timing of ebullition (Fig. 6-10; 6-8).

Maximum $\text{CH}_{4(\text{aq})}$ fluxes coincide with the high ebullition periods in the summer to late fall. Best fit consumption rates can decrease the mass loading rate into the water cap by up to 35% during high ebullition periods. The average flux at the TWI in high periods was $0.0364 \text{ g d}^{-1} \text{ m}^{-2}$ at P1C and $0.0443 \text{ g d}^{-1} \text{ m}^{-2}$ at P2NE. In low flux periods, the average flux was $0.0128 \text{ g d}^{-1} \text{ m}^{-2}$ at P1C and $0.00823 \text{ g d}^{-1} \text{ m}^{-2}$ at P2NE. Dissolved CH_4 transport at P3SW exhibits a less variable flux across the TWI consistent with the lower changes in the diffusion coefficient required to simulate observed conservative tracer profiles (Fig. 6-6; 6-7). The average flux at the TWI after 2015, when the flux variations were largely attenuated, was $0.00135 \text{ g d}^{-1} \text{ m}^{-2}$. Extrapolating this flux across the entire FFT surface area gives a range of 19 to 84 tonnes of $\text{CH}_{4(\text{aq})}$ expressed across the TWI over the course of a year. Seasonally variable ebullition also impacts flux across the TWI, enhancing mass flux over five-fold during the highly ebullitive months compared to the quiescent months in some locations (Fig. 6-10). Model outputs indicate that (i) CH_4 consumption occurs within the upper FFT overlying the zone of enhanced production and (ii) CH_4 mass loading to the water cover is affected by ebullition.

These models were a preliminary investigation into the role of anaerobic oxidation and its influence on $\text{CH}_{4(\text{aq})}$ concentrations and mass transport. These models could be further constrained by varying the consumption rate applied over the FFT interval above the zone of saturation. Given that chemical species associated with anaerobic CH_4 oxidation are most abundant above or within 0.5 m of the TWI, it would be assumed that greater $\text{CH}_{4(\text{aq})}$ consumption would occur there relative to deeper FFT.

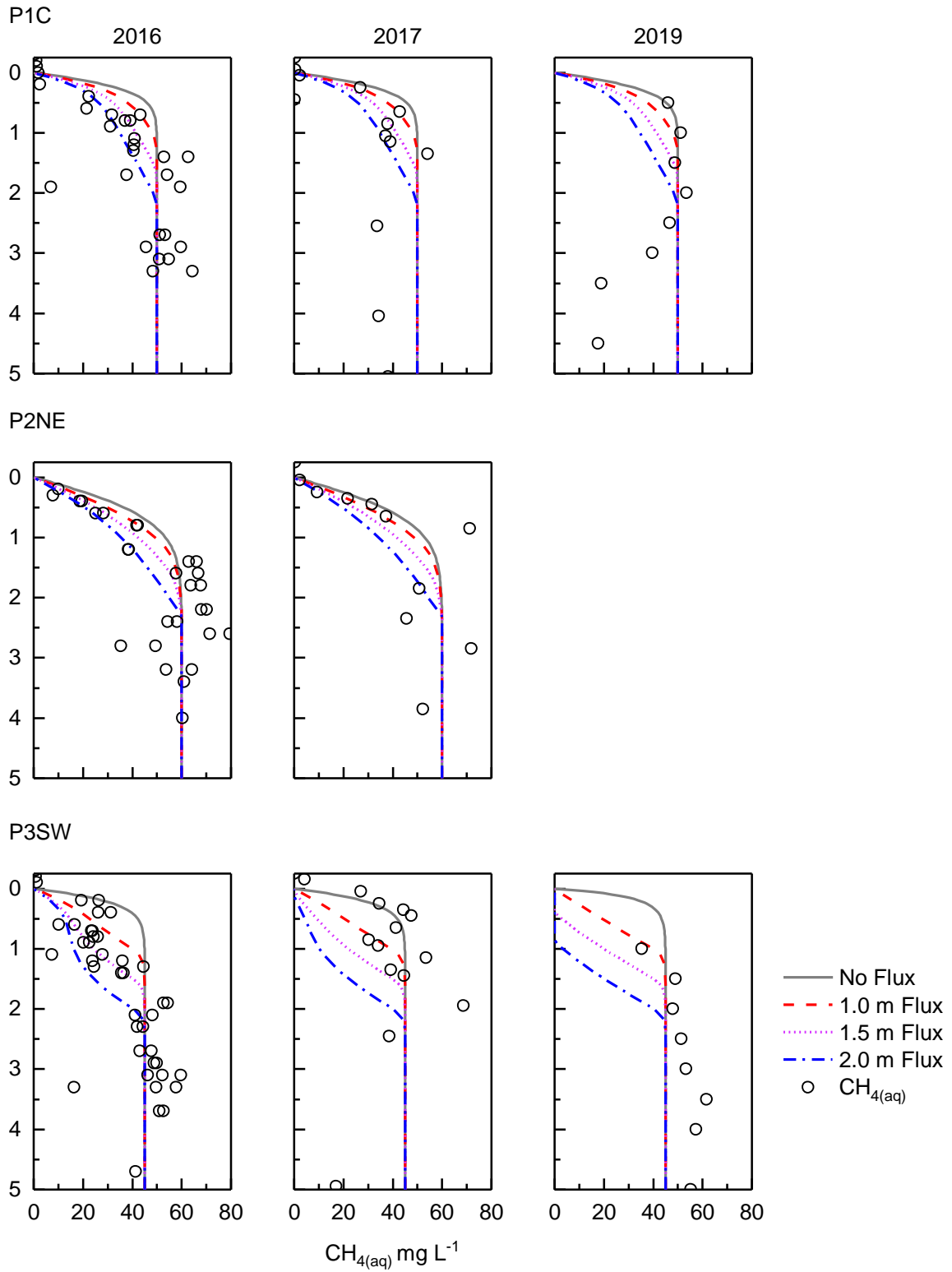


Figure 6-9: Mass transport model profiles for CH₄ depth profiles by year and location extending to 5 m below the TWI.

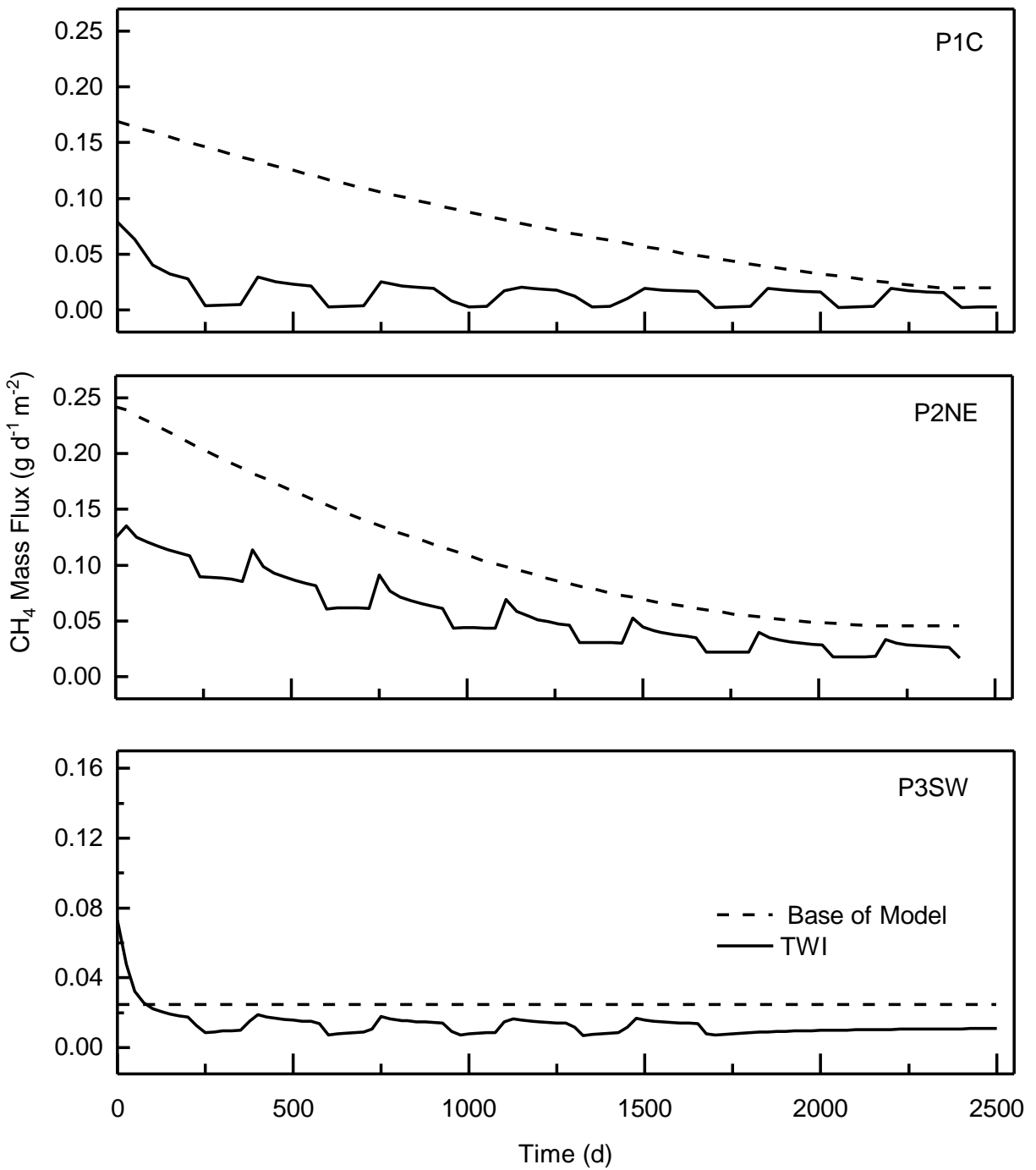


Figure 6-10: Conservative and consumptive CH_{4(aq)} mass flux rate over the modelled period at the TWI. The consumptive model flux shown uses a consumption rate over 1.0 m at both P1C and P3SW and 1.5 m at P2NE.

6.4 Revised Conceptual Model

The conceptual model for internal mass loading can be used to identify the influence of different processes on mass transport from the FFT into the water cap (Fig. 6-11). It compiles results and interpretations from different aspects of collaborative research contributing to the understanding of internal mass loading in BML. The work presented here contributes to the development of the conceptual model by constraining the influence of mixing by CH₄ ebullition on mass transport. In early time, the mass transport is primarily controlled by upwards advective dispersive transport of FFT porewater into the overlying water cap from FFT settlement. Transport of pore-water constituents from the FFT to overlying water cover may adversely impact the development of the water cap quality. Ebullition may enhance transport into water cap via physical mixing of the FFT over the bubbled interval which extend to lower boundary of the zone of CH₄ saturation.

Settlement is expected to slow with time, leading to development of a diffusion dominated transport regime. Older FFT will have had more time to settle relative to younger FFT leading to variable settlement rates across BML. Strong, diffusive gradients across the TWI are present as the FFT porewater is elevated with respect to a number of solutes correlated with OSPW or secondary process in tailings, such as methanogenesis (Dompierre et al., 2016; Rudderham 2019; Stasik and Wendt-Pothoff, 2016; Stasik et al., 2014). This strong, diffusive gradient is expected to persist as the water cap develops due to fresh water inputs.

The final part of the conceptual model involves mixing by ebullition which has the tendency to enhance transport in the upper FFT. Ebullition is limited by the depth of exsolution and bubble release where gases are supersaturated within the porewater and bubbles are sufficiently buoyant to overcome the yield strength of the confining FFT. Multiple factors can affect the potential for ebullition across BML, and the complexity leads to variable amounts of ebullition, both temporally and spatially.

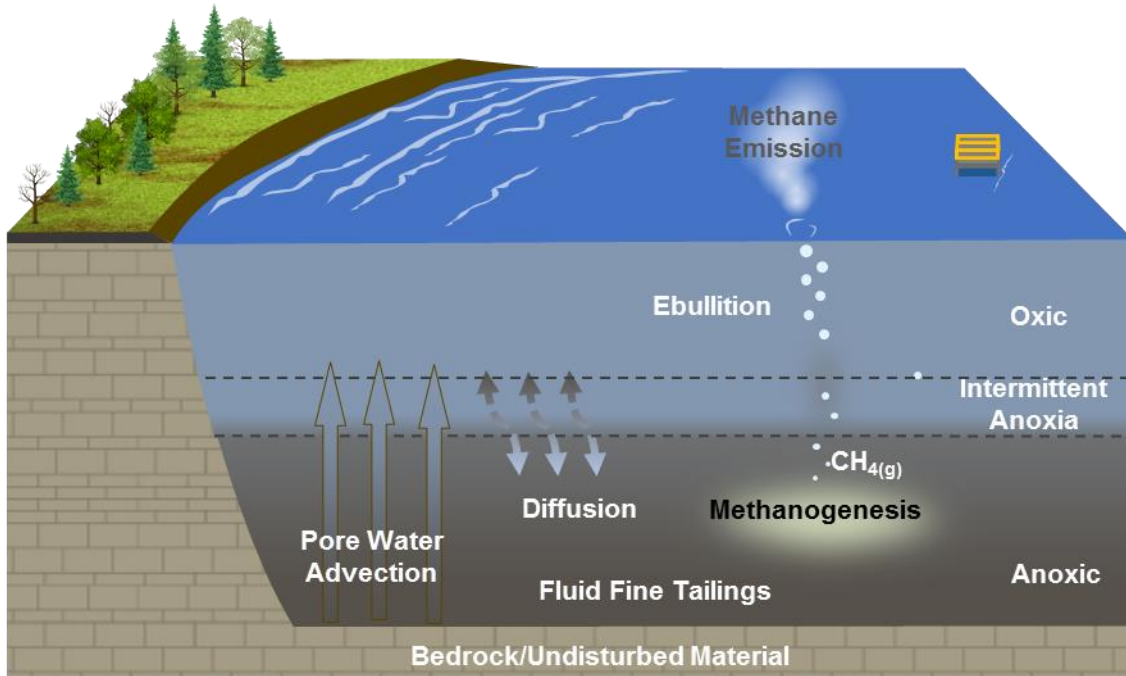


Figure 6-11: General conceptual model showing the main processes that affect mass transport within BML.

A second conceptual model was created to summarize the complex interplay of physical, biological and chemical factors that can influence the potential for CH_4 ebullition in an oil sands EPL (Fig. 6-12). Ebullition is an important ongoing process that results from the interaction of porewater chemistry, FFT microbiology, settlement, temperature and FFT provenance and age. Ebullition is possible across BML, but areas that have higher temperatures and settlement rates also have the highest $\text{CH}_{4(\text{aq})}$ concentrations, the greatest degree of saturation and, therefore, the highest ebullition potential.

Methane is produced biogenically via the degradation of diluent HCs available in the FFT. The availability of these diluent HCs may be related to both the age of the FFT and the previous tailings impoundments that the FFT was stored in. While it is likely that methanogenesis occurs throughout the FFT profile, the majority appears to occur within the upper tailings from 1.5 to 3.0 m based on modelled saturation. Below this zone, the FFT is undersaturated with respect to

CH₄. Any excess CH_{4(aq)} is exsolved and may then be released as bubbles to the water cap and atmosphere.

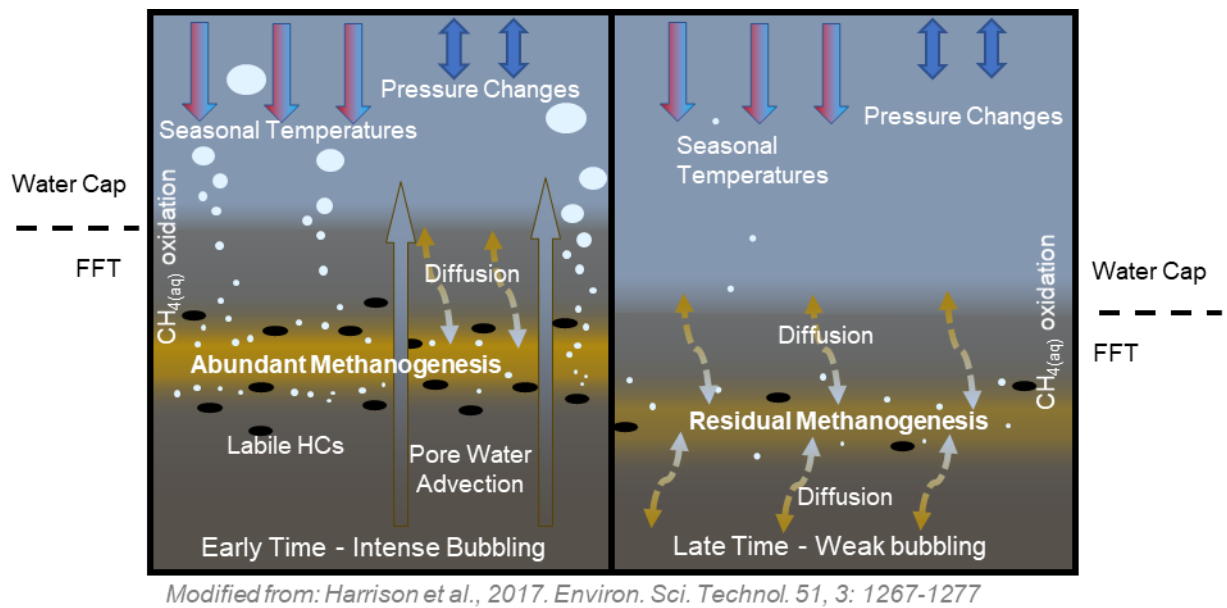


Figure 6-12: Conceptual model of the parameters affecting ebullition potential in BML. Modified from Harrison et al. (2017).

CH_{4(aq)} sinks include aerobic and anaerobic oxidation occurring in the water cap and FFT, respectively. As anoxic conditions are found to variably occur in the hypolimnion of the water cap, the degree of oxidation across the TWI may change with time (Risacher et al., 2018; Arriaga et al., 2019). In early time advective dispersive transport can limit the degree of saturation in BML as advection transports CH_{4(aq)} upwards into the water cap, and CH_{4(aq)} will diffuse outwards from the zone of primary production. Physical parameters that can increase the ebullition potential include seasonal increases in upper FFT temperatures and drops in water level or barometric pressure. Temperature increases will lower the solubility limit and induce exsolution in previously saturated or near-saturated waters. Decreases in water cap thickness or barometric pressure may induce bubbling events by reducing the yield strength on the confining sediments (Harrison et al., 2017). The physical processes that limit ebullition are seasonal cooling in the late fall that will increase solubility and increases in the overlying pressure such as increases in water cap thickness, ice formation, and snowfall.

The long-term CH₄ ebullition potential is not known, but specific trends in parameters influencing ebullition potential can be discerned. Continued settlement would lead to increasing CH_{4(aq)} solubility at a rate tied to settlement which slows with time. As settlement slows mass transport shifts to a primarily diffusion dominated system. In a diffusion dominated system CH_{4(aq)} can diffuse outwards and into the underlying, undersaturated FFT. The availability of easily biodegraded hydrocarbons to become fuel for acetoclastic methanogenesis is expected to decrease with time, which could cause a decrease in the overall rate of methanogenesis. Seasonal temperature changes are expected to persist long term, and changes in confining pressure may still occur causing short term variations in solubility and may induce ebullition. In the long term EPL may have a reduced potential long term as the CH₄ storage capacity increases and methanogenesis slows. The revised conceptual model does not account for impacts of changing water cap processes on CH₄ dynamics. If labile organic carbon availability increases due to changing primary production, the vertical distribution of CH₄ production and consumption reactions may shift relative to the TWI towards the water cap. However, exsolution and ebullition likely wouldn't occur in the water cap as transport processes move CH_{4(aq)} away.

CHAPTER 7: CONCLUSIONS

The overall objective of the study was to evaluate whether CH₄ ebullition could impact the internal mass loading of an oil sands EPL. Gas pressure surveys, CH₄ solubility modelling, and noble gas analysis were used to determine the potential for CH₄ ebullition in FFT. Detailed FFT porewater analysis was carried out and combined with previously published FFT geochemical data to identify geochemical gradients from the water cap into the FFT. These results informed development of numerical transport models that simulated ebullition with enhanced diffusion coefficients across the CH₄ saturated interval. The influence of anaerobic CH₄ consumption on CH_{4(aq)} flux into the water cap was determined by reactive transport models built off the conservative transport models. Methane saturation was identified in a FFT interval between 1.5 and 3 m below the TWI that persisted between sampled years indicating a zone of continuous enhanced production. Observed chemical gradients from the FFT to the water cap throughout BML indicated a chemical difference between FFT porewater and the water cap. Transport models with enhanced diffusion coefficients suggest that ebullition may explain observed depth profiles that cannot be simulated by advective-dispersive transport alone. Dissolved CH₄ transport models show that anaerobic oxidation in the upper FFT above the zone of saturation can reduce the flux into the water cap by up to 35%. These findings were used to update the conceptual model for internal mass loading in an EPL and informed the development of a conceptual model examining the relationship between the different parameters influencing CH₄ dynamics in BML.

Results from field investigations showed that seasonal temperature cycles influence the upper 4 m of FFT in BML and that FFT is slowly cooling over time. FFT settlement was found to be laterally variable, with the central and SW portions of BML settling at rates comparable to early predictive models while the freshest tailings in the NE were settling at a much higher rate. Geochemical depth profiles all have short depth intervals where dissolved concentrations increased from water cap values to FFT porewater values.

Calculated CH₄ solubility was found to be influenced by changes in both temperatures and pressure in BML. Seasonal temperature cycles influence the solubility in the upper FFT lower the solubility limit in summer and autumn and raising it in the winter and spring. Increasing water cap

thickness raises fluid pressure and the CH₄ solubility at a given depth. Total dissolved gas pressure results, CH₄ solubility modelling and noble gas analysis indicate that ebullition was likely across BM in a narrow 1.5 m thick zone where CH₄ concentrations approached or reached modelled saturation limits. Total dissolved gas pressures met or exceeded fluid pressure in sampled depths at 1, 2 3 and in some locations 5 m below the TWI. Noble gas ratios show depletion of lighter NGs relative to heavier NGs with depth. The last deposited and hottest tailings to the NE of BML showed both greater CH₄ saturation and higher total dissolved gas pressures relative to fluid pressures. Ebullition potential was tied to both the age and the provenance of the FFT in BML.

Internal mass loading in the EPL was found to be a function of both advective dispersive transport and physical mixing of the upper FFT by CH₄ ebullition. Advection due to porewater expression from FFT settlement is slowing with time. Ebullition has a important role in the internal mass loading of an EPL and can enhance internal flux rates from the FFT during periods of ebullition. Reactive transport modeling demonstrated that CH_{4(aq)} flux rates into the water cap were limited by anaerobic oxidation in the uppermost FFT above the zone of saturation. Anaerobic oxidation of CH_{4(aq)} is likely tied to other biogeochemical processes that involve S or N cycling. The findings from this thesis inform the long term CH₄ dynamics within an EPL and provide insight into the controls on internal mass loading. The results from this study can be used to inform future EPL designs, however, further studies should be carried out for different designs and tailings used. The findings can also inform studies on other hydrocarbon contaminated saturated sites where gas producing sediments may be settling or unloading.

CHAPTER 8: RECOMMENDATIONS

Findings from this body of work demonstrated that FFT porewater geochemistry did not vary substantially temporally and did not warrant further study at this time, this is consistent with the findings of Rudderham (2019). However, as the parameters around CH_4 solubility and ebullition continue to evolve with BML, further investigation into dissolved CH_4 concentrations, temperatures, dissolved gas pressures, and FFT settlement do warrant further study. Long-term trends of these parameters can better constrain the long-term internal mass loading of the EPL, particularly with regards to the shift from advective-dispersive to diffusion dominated mass transport and the shift in biogeochemical processes as various diluent HCs are degraded. Changes in these processes may impact long term dissolved oxygen content in the water cap by altering the loading of oxygen consuming constituents into the water cap.

This research is built upon an established modelling framework for internal mass loading of an oil sands end pit lake. It demonstrated that simple reactive terms could be used to approximate the reactive species $\text{CH}_{4(\text{aq})}$. More work with modelling and applying different scenarios could develop a stronger characterization of the mass flux of dissolved CH_4 into the water cap, and the relative contributions of dissolved transport compared with dissolution from fugitive bubbles. The $\text{CH}_{4(\text{aq})}$ transport model developed here is preliminary and makes some concessions; a more rigorous model would use an applied positive mass flux to represent the effect of methane production in the FFT instead of a constant boundary concentration at the bottom of the model domain. Further investigations using the models presented here could be applied to other reactive species, particularly those that are of interest to the long-term evolution of the water cap. Oxygen consuming constituents have been identified a possible challenge to long term water quality, the mass transport regime and the flux of NH_4^+ has yet to be investigated in BML (Rudderham 2019; Risacher et al., 2019; Arriaga et al., 2019). While the long-term mass loading regime has been discussed here, investigations using numerical models under a variety of long-term scenarios such as diffusion dominated, different magnitudes of FFT mixing by ebullition would provide valuable insight into the long term EPL evolution in both the FFT and water cap quality.

REFERENCES

- Alberta Energy Regulator, 2017. Directive 085: Fluid Tailings Management for Oil Sands Mining Projects.
- Allen, E.W., 2008. Process water treatment in Canada's oil sands industry: I. Target pollutants and treatment objectives. *J. Environ. Eng. Sci.* 7, 123–138. doi:10.1139/S07-038
- Arriaga, D., Nelson, T.C., Risacher, F.F., Morris, P.K., Goad, C., Slater, G.F., Warren, L.A., 2019. The co-importance of physical mixing and biogeochemical consumption in controlling water cap oxygen levels in Base Mine Lake. *J. Appl. Geochem.* 111, 1–12. <https://doi.org/10.1016/j.apgeochem.2019.104442>
- Bao, P., and Li, G. X. (2017). Sulfur-driven iron reduction coupled to anaerobic ammonium oxidation. *Environ. Sci. Technol.* 51, 6691–6698. doi: 10.1021/acs.est.6b05971
- Barbosa, P.M., Farjalla, V.F., Melack, J.M., Amaral, J.H.F., da Silva, J.S., Forsberg, B.R., 2018. High rates of methane oxidation in an Amazon floodplain lake. *Biogeochem.* 137, 351–365. doi:10.1007/s10533-018-0425-2
- Barr Engineering Co., 2017. 2016 Base Mine Lake Annual FFT Physical Assessment Report (Industry Report).
- Beal, E.J., House, C.H., Orphan, V.J., 2009. Manganese- and Iron-Dependent Marine Methane Oxidation. *Science* 325, 184–187. doi: 10.1126/science.1169984
- Bethke, C.M., Sanford, R.A., Kirk, M.F., Jin, Q., Flynn, T.M., 2011. The thermodynamic ladder in geomicrobiology. *Am. J. Sci.* 311, 183–210. doi:10.2475/03.2011.01
- Beyerle, U., Aeschbach-Hertig, W., Imboden, D.M., Baur, H., Graf, T., Kipfer, R., 2000. A Mass Spectrometric System for the Analysis of Noble Gases and Tritium from Water Samples. *Environ. Sci. Technol.* 34, 2042–2050. doi:10.1021/es990840h
- BGC Engineering Inc., T., 2010. Oil Sands Tailings Technology Review, Oil Sands Research and Information Network. BGC Engineering inc.
- Boudreau, B.P., 1996. The diffusive tortuosity of fine-grained unlithified sediments. *Geochim. et Cosmochim. Acta* 60, 3139–3142. doi:10.1016/0016-7037(96)00158-5

- Brown, D., Ramos-Padrón, E., Gieg, L., Voordouw, G., 2013. Effect of calcium ions and anaerobic microbial activity on sedimentation of oil sands tailings. *Int. Biodeter. Biodegr.* 81, 9–16. doi: 10.1016/j.ibiod.2012.07.006
- Carey, S.K., 2008. Growing season energy and water exchange from an oil sands overburden reclamation soil cover, Fort McMurray, Alberta, Canada. *Hydrol. Process.* 22, 2847–2857. doi:10.1002/hyp.7026
- Castro, J.M., Moore, J.N., 2000. Pit lakes: their characteristics and the potential for their remediation. *J. Environ. Geol.* 39, 1254–1260. doi:10.1007/s002549900100
- Clark, K.A., Pasternack, D.S., 1932. Hot Water Separation of Bitumen from Alberta Bituminous Sand. *Ind. Eng. Chem. Res.* 24, 1410–1416. doi:10.1021/ie50276a016
- Cumulative Environmental Management Association (CEMA) (2012), End pit lakes guidance document [online], Fort McMurray, Alberta, Canada. [Available at <http://www.cemaonline.ca>, last accessed 11 Oct 2018.]
- Chalaturnyk, R.J., Don Scott, J., Özüim, B., 2002. MANAGEMENT OF OIL SANDS TAILINGS. *Petrol. Sci. and Technol.* 20, 1025–1046. doi:10.1081/LFT-120003695
- Chen, M., Walshe, G., Chi Fru, E., Ciborowski, J.J.H., Weisener, C.G., 2013. Microcosm assessment of the biogeochemical development of sulfur and oxygen in oil sands fluid fine tailings. *J. Appl. Geochem.* 37, 1–11. doi: 10.1016/j.apgeochem.2013.06.007
- DelSontro, T., McGinnis, D.F., Sobek, S., Ostrovsky, I., Wehrli, B., 2010. Extreme Methane Emissions from a Swiss Hydropower Reservoir: Contribution from Bubbling Sediments. *Environ. Sci. Technol.* 44, 2419–2425. doi:10.1021/es9031369
- Deutzmann, J.S., Stief, P., Brandes, J., Schink, B., 2014. Anaerobic methane oxidation coupled to denitrification is the dominant methane sink in a deep lake. *Proc Natl Acad Sci USA* 111, 18273–18278. doi:10.1073/pnas.1411617111
- Dompierre, K., Barbour, L., Halferdahl, G., 2014. Characterization of the thermal regime through the oil sands fluid fine tailings in an end pit lake. Presented at the Geo Regina 2014, p. 8.

- Dompierre, K.A., Barbour, S.L., 2016. Characterization of physical mass transport through oil sands fluid fine tailings in an end pit lake: a multi-tracer study. *J. Contam. Hydrol.* 189, 12–26. doi: 10.1016/j.jconhyd.2016.03.006
- Dompierre, K.A., Lindsay, M.B.J., Cruz-Hernández, P., Halferdahl, G.M., 2016. Initial geochemical characteristics of fluid fine tailings in an oil sands end pit lake. *Sci. Total Environ.* 556, 196–206. doi: 10.1016/j.scitotenv.2016.03.002
- Dompierre, K.A., Barbour, S.L., North, R.L., Carey, S.K., Lindsay, M.B.J., 2017. Chemical mass transport between fluid fine tailings and the overlying water cover of an oil sands end pit lake: mass transport in an oil sands end pit lake. *Water Resour. Res.* 53, 4725–4740. doi:10.1002/2016WR020112
- Don Scott, J., Dusseault, M.B., David Carrier, W., 1985. Behaviour of the clay/bitumen/water sludge system from oil sands extraction plants. *Appl. Clay Sci.* 1, 207–218. doi:10.1016/0169-1317(85)90574-5
- Duan, Z., Mao, S., 2006. A thermodynamic model for calculating methane solubility, density and gas phase composition of methane-bearing aqueous fluids from 273 to 523K and from 1 to 2000bar. *Geochim. et Cosmochim. Acta* 70, 3369–3386. doi: 10.1016/j.gca.2006.03.018
- Environment Canada (2015), Canadian Climate Data [online], Gov. of Can., Ottawa. [Available at <http://climate.weather.gc.ca>, last accessed Aug 08, 2018.]
- Ettwig, K.F., van Alen, T., van de Pas-Schoonen, K.T., Jetten, M.S.M., Strous, M., 2009. Enrichment and Molecular Detection of Denitrifying Methanotrophic Bacteria of the NC10 Phylum. *Appl. Environ. Microbiol.* 75, 3656–3662. doi:10.1128/AEM.00067-09
- Fedorak, P.M., Coy, D.L., Dudas, M.J., Simpson, M.J., Renneberg, A.J., MacKinnon, M.D., 2003. Microbially-mediated fugitive gas production from oil sands tailings and increased tailings densification rates. *Environ. Eng. Sci.* 2, 199–211. doi:10.1139/s03-022
- Fendinger, N.J., Adams, D.D., Glotfelty, D.E., 1992. The role of gas ebullition in the transport of organic contaminants from sediments. *Sci. Total Environ.* 112, 189–201. doi:10.1016/0048-9697(92)90187-W

- Foght, J.M., Gieg, L.M., Siddique, T., 2017. The microbiology of oil sands tailings: past, present, future. *FEMS Microbiology Ecology* 93. doi:10.1093/femsec/fix034
- Goad, C.A., 2017. Methane biogeochemical cycling over seasonal and annual scales in an oil sands tailings end pit lake. McMaster University, Hamilton, Ontario.
- GEO-SLOPE International Ltd. (2018a), Contaminant Modeling With CTRAN/W, Version 2018 [computer program], GEO-SLOPE Int. Ltd., Calgary, Canada.
- GEO-SLOPE International Ltd. (2018b), Seepage Modeling With SEEP/W, Version 2018 [computer program], GEO-SLOPE Int. Ltd., Calgary, Canada.
- Gibson, J.J., Fennell, J., Birks, S.J., Yi, Y., Moncur, M.C., Hansen, B., Jasechko, S., 2013. Evidence of discharging saline formation water to the Athabasca River in the oil sands mining region, northern Alberta. *Can. J. Earth Sci.* 50, 1244–1257. doi:10.1139/cjes-2013-0027
- Gosselin, P., Hrudley, S.E., Naeth, M.A., Plourde, A., Therrien, R., Van Der Kraak, G., Xu, Z., 2010. Environmental and Health IMpacts of Canada's Oil Sands Industry (No. 1), Royal Society of Canada Expert Panel. The Royal Society of Canada.
- Government of Alberta, 2019a. Oil Sands Information Portal [WWW Document]. [Available at: <http://osip.alberta.ca/map/> last accessed Jul 15, 2019]
- Government of Alberta, 2019b. Alberta Oil Sands: Facts and Statistics [online], Edmonton, Canada. [Available at: <https://www.energy.alberta.ca/OS/AOS/Pages/FAS.aspx>, last accessed Jul 15, 2019]
- Guérin, F., Abril, G., 2007. Significance of pelagic aerobic methane oxidation in the methane and carbon budget of a tropical reservoir: CH₄ oxidation in a tropical reservoir. *J. Geophys. Res.* 112, n/a-n/a. doi:10.1029/2006JG000393
- Guo, C., 2009. Rapid Densification of the Oil Sands Mature Fine Tailings (MFT) by Microbial Activity. University of Alberta, Edmonton, Canada.
- Harrison, J.A., Deemer, B.R., Birchfield, M.K., O'Malley, M.T., 2017. Reservoir Water-Level Drawdowns Accelerate and Amplify Methane Emission. *Environ. Sci. Technol.* 51, 1267–1277. doi: 10.1021/acs.est.6b03185

- Hein, F.J., Cotterill, D.K., 2006. The Athabasca Oil Sands — A Regional Geological Perspective, Fort McMurray Area, Alberta, Canada. *Nat. Resour. Res.* 15, 85–102. doi:10.1007/s11053-006-9015-4
- Holowenko, F.M., MacKinnon, M.D., Fedorak, P.M., 2000. Methanogens and sulfate-reducing bacteria in oil sands fine tailings waste. *Can. J. Microbiol* 46, 927–937.
- Huber, C., Beyerle, U., Leuenberger, M., Schwander, J., Kipfer, R., Spahni, R., Severinghaus, J., Weiler, K., 2006. Evidence for molecular size dependent gas fractionation in firm air derived from noble gases, oxygen, and nitrogen measurements. *Earth Planet. Sci. Lett.* 243, 61–73. doi: 10.1016/j.epsl.2005.12.036
- Jones, K.L., Lindsay, M.B.J., Kipfer, R., Mayer, K.U., 2014. Atmospheric noble gases as tracers of biogenic gas dynamics in a shallow unconfined aquifer. *Geochim. et Cosmochim. Acta* 128, 144–157. doi: 10.1016/j.gca.2013.12.008
- Joyce, J., Jewell, P.W., 2003. Physical Controls on Methane Ebullition from Reservoirs and Lakes. *Environ. Eng. Geosci.* 9, 167–178. doi:10.2113/9.2.167
- Kabwe, L.K., Scott, J.D., Beier, N.A., Wilson, G.W., Jeeravipoolvarn, S., 2018. Environmental implications of end pit lakes at oil sand mines in Alberta, Canada. *Environ. Geotech.* 1–8. doi:10.1680/jenge.17.00110
- Kachhwal, L.K., Yanful, E.K., Lanteigne, L., 2011. Water Cover Technology for Reactive Tailings Management: A Case Study of Field Measurement and Model Predictions. *Water Air Soil Poll.*, 214, 357–382. doi:10.1007/s11270-010-0429-6
- Kaperski, K.L., 2003. Review of research on aqueous extraction of bitumen from mined oil sands. Unpublished report. CANMET Energy Technology Centre, Natural Resources Canada, Deven, Alberta.
- Kaperski, K.L., 1992. A review of properties and treatment of oil sands tailings. *AOSTRA* 8: 11–53.
- Kasperski, K.L., Mikula, R.J., 2011. Waste Streams of Mined Oil Sands: Characteristics and Remediation. *Elements* 7, 387–392. doi:10.2113/gselements.7.6.387

- Kavanagh, R.J., Frank, R.A., Burnison, B.K., Young, R.F., Fedorak, P.M., Solomon, K.R., Van Der Kraak, G., 2012. Fathead minnow (*Pimephales promelas*) reproduction is impaired when exposed to a naphthenic acid extract. *Aquat. Toxicol.* 116–117, 34–42. doi: 10.1016/j.aquatox.2012.03.002
- Kavcar, P.C., Wright, S.J., 2009. Effects of Gas Ebullition on Cohesive Sediment Resuspension and Cap Stability, in: World Environmental and Water Resources Congress 2009. Presented at the World Environmental and Water Resources Congress 2009, American Society of Civil Engineers, Kansas City, Missouri, United States, pp. 1–10. doi:10.1061/41036(342)351
- Kipfer, R., Aeschbach-Hertig, W., Peeters, F., Stute, M., 2002. Noble Gases in Lakes and Ground Waters. *Rev. Mineral. Geochem.* 47, 615–700. doi:10.2138/rmg.2002.47.14
- Knittel, K., Boetius, A., 2009. Anaerobic Oxidation of Methane: Progress with an Unknown Process. *Annu. Rev. Microbiol.* 63, 311–334. doi: 10.1146/annurev.micro.61.080706.093130
- Kong, J.D., Wang, H., Siddique, T., Foght, J., Semple, K., Burkus, Z., Lewis, M.A., 2019. Second-generation stoichiometric mathematical model to predict methane emissions from oil sands tailings. *Sci. Total Environ.* 694, 133645. doi: 10.1016/j.scitotenv.2019.133645
- Lawrence, G.A., Tedford, E.W., Pieters, R., 2016. Suspended solids in an end pit lake: potential mixing mechanisms. *Can. J. Civ. Eng.* 43, 211–217. doi:10.1139/cjce-2015-0381
- Lin, J.-L., Joye, S.B., Scholten, J.C.M., Schafer, H., McDonald, I.R., Murrell, J.C., 2005. Analysis of Methane Monooxygenase Genes in Mono Lake Suggests That Increased Methane Oxidation Activity May Correlate with a Change in Methanotroph Community Structure. *Appl. Environ. Microbiol.* 71, 6458–6462. doi: 10.1128/AEM.71.10.6458-6462.2005
- Luo, J.-H., Chen, H., Hu, S., Cai, C., Yuan, Z., Guo, J., 2018. Microbial Selenate Reduction Driven by a Denitrifying Anaerobic Methane Oxidation Biofilm. *Environ. Sci. Technol.* 52, 4006–4012. doi: 10.1021/acs.est.7b05046
- Martinez-Cruz, K., Leewis, M.-C., Herriott, I.C., Sepulveda-Jauregui, A., Anthony, K.W., Thalasso, F., Leigh, M.B., 2017. Anaerobic oxidation of methane by aerobic methanotrophs in sub-Arctic lake sediments. *Sci. Total Environ.* 607–608, 23–31. doi: 10.1016/j.scitotenv.2017.06.187

- Masliyah, J., Zhou, Z.J., Xu, Z., Czarnecki, J., Hamza, H., 2008. Understanding Water-Based Bitumen Extraction from Athabasca Oil Sands. *Can. J. Chem. Eng.* 82, 628–654. doi:10.1002/cjce.5450820403
- McCance, W., Jones, O.A.H., Edwards, M., Surapaneni, A., Chadalavada, S., Currell, M., 2018. Contaminants of Emerging Concern as novel groundwater tracers for delineating wastewater impacts in urban and peri-urban areas. *Wat. Res.* 146, 118–133. doi:10.1016/j.watres.2018.09.013
- Misiti, T., Tandukar, M., Tezel, U., Pavlostathis, S.G., 2013. Inhibition and biotransformation potential of naphthenic acids under different electron-accepting conditions. *Water Res.* 47, 406–418. doi: 10.1016/j.watres.2012.10.019
- Nozhevnikova, A.N., Ammann, A., Zehnder, A.J.B., 1997. Methanogenesis in sediments from deep lakes at different temperatures (2–70°C). *Wat. Sci. Tech.* 36, 57–64. doi:10.2166/wst.1997.0575
- Oil Sands magazine, 2019a. In-Situ Bitumen Extraction [online]. Calgary, AB, Canada. [Available at: <https://www.oilsandsmagazine.com/technical/in-situ>, Last accessed Jul 15, 2019
- Oil Sands magazine, 2019b. Mining for Bitumen [online]. Calgary, AB, Canada. [Available at: <https://www.oilsandsmagazine.com/technical/mining>, Last accessed Jul 15, 2019
- Onset Computer Corporation, 2010, HOBOWare Pro V2 User Guide [Online]. Bourne, MA, U.S.A. [Available at https://www.onsetcomp.com/files/manual_pdfs/10694-H-MAN-U23.pdf, Last accessed Jul, 17, 2019]
- Oswald, K., Milucka, J., Brand, A., Hach, P., Littmann, S., Wehrli, B., Kuypers, M.M.M., Schubert, C.J., 2016. Aerobic gammaproteobacterial methanotrophs mitigate methane emissions from oxic and anoxic lake waters: Methane oxidation in Lake Zug. *Limnol. Oceanogr.* 61, S101–S118. doi:10.1002/lno.10312
- Penner, T.J., Foght, J.M., 2010. Mature fine tailings from oil sands processing harbour diverse methanogenic communities. *Can. J. Microbiol.* 56, 459–470. doi:10.1139/W10-029
- Pieters, R., Lawrence, G.A., 2009. Effect of salt exclusion from lake ice on seasonal circulation. *Limnol. Oceanogr.* 54, 401–412. doi:10.4319/lo.2009.54.2.0401

- Prakash, S., Vandenberg, J.A., Buchak, E., n.d. The Oil Sands Pit Lake Model – Sediment Diagenesis Module 8.
- Quin, P., Joseph, S., Husson, O., Donne, S., Mitchell, D., Munroe, P., Phelan, D., Cowie, A., Van Zwieten, L., 2015. Lowering N₂O emissions from soils using eucalypt biochar: the importance of redox reactions. *Scientific Reports* 5. doi:10.1038/srep16773
- Reeburgh, W.S., 1980. Anaerobic methane oxidation: Rate depth distributions in Skan Bay sediments. *Earth Planet. Sci. Lett.* 47, 345–352. doi: 10.1016/0012-821X(80)90021-7
- Risacher, F.F., Morris, P.K., Arriaga, D., Goad, C., Nelson, T.C., Slater, G.F., Warren, L.A., 2018. The interplay of methane and ammonia as key oxygen consuming constituents in early stage development of Base Mine Lake, the first demonstration oil sands pit lake. *J. Appl. Geochem.* 93, 49–59. doi: 10.1016/j.apgeochem.2018.03.013
- Roy, R., Knowles, R., Charlton, M.N., 1996. Nitrification and methane oxidation at the sediment surface in Hamilton Harbour (Lake Ontario). *Can. J. Fish. Aquat. Sci.* 53, 2466–2472.
- Rudderham, S.B., 2019. Geomicrobiology and Geochemistry of Fluid Fine Tailings in and Oil Sands End Pit Lake. M.Sc. Thesis, University of Saskatchewan, Saskatoon, Canada, 96 pp.
- Ruecker, A., Uzun, H., Karanfil, T., Tsui, M.T.K., Chow, A.T., 2017. Disinfection byproduct precursor dynamics and water treatability during an extreme flooding event in a coastal blackwater river in southeastern United States. *Chemosphere* 188, 90–98. doi: 10.1016/j.chemosphere.2017.08.122
- Saarela, T., Rissanen, A.J., Ojala, A., Pumpanen, J., Aalto, S.L., Tirola, M., Vesala, T., Jäntti, H., 2020. CH₄ oxidation in a boreal lake during the development of hypolimnetic hypoxia. *Aquat Sci* 82, 19. doi:10.1007/s00027-019-0690-8
- Saidi-Mehrabad, A., He, Z., Tamas, I., Sharp, C.E., Brady, A.L., Rochman, F.F., Bodrossy, L., Abell, G.C., Penner, T., Dong, X., Sensen, C.W., Dunfield, P.F., 2013. Methanotrophic bacteria in oilsands tailings ponds of northern Alberta. *J. ISME* 7, 908–921. doi:10.1038/ismej.2012.163

- Scandella, B.P., Delwiche, K., Hemond, H.F., Juanes, R., 2017. Persistence of bubble outlets in soft, methane-generating sediments: Bubbles in methane-generating sediments. *J. Geophys. Res. Biogeo.* 122, 1298–1320. doi:10.1002/2016JG003717
- Scandella, B.P., Varadharajan, C., Hemond, H.F., Ruppel, C., Juanes, R., 2011. A conduit dilation model of methane venting from lake sediments: Methane venting from lake sediments. *Geophys. Res. Lett.* 38, 1-6. doi:10.1029/2011GL046768
- Schubert, C.J., Lucas, F.S., Durisch-Kaiser, E., Stierli, R., Diem, T., Scheidegger, O., Vazquez, F., Müller, B., 2010. Oxidation and emission of methane in a monomictic lake (Rotsee, Switzerland). *Aquat. Sci.* 72, 455–466. doi: 10.1007/s00027-010-0148-5
- Siddique, T., Fedorak, P.M., MacKinnon, M.D., Foght, J.M., 2007. Metabolism of BTEX and Naphtha Compounds to Methane in Oil Sands Tailings. *Environ. Sci. Technol.* 41, 2350–2356. doi:10.1021/es062852q
- Siddique, T., Kuznetsov, P., Kuznetsova, A., Arkell, N., Young, R., Li, C., Guigard, S., Underwood, E., Foght, J.M., 2014. Microbially-accelerated consolidation of oil sands tailings. Pathway I: changes in porewater chemistry. *Front. Microbiol.* 5. doi:10.3389/fmicb.2014.00106
- Siddique, T., Stasik, S., Mohamad Shahimin, M.F., Wendt-Potthoff, K., 2018. Microbial communities in oil sands tailings: their implications in biogeochemical processes and tailings management. Springer Nat. Switz. AG 2018 T. J. McGenity (ed.), *Microbial Communities Utilizing Hydrocarbons and Lipids: Handbook of Hydrocarbon and Lipid Microbiology*, 2nd edn. Springer, Cham, 1-33.
- Sirhan, S.T., Katsman, R., Lazar, M., 2019. Methane Bubble Ascent within Fine-Grained Cohesive Aquatic Sediments: Dynamics and Controlling Factors. *Environ. Sci. Technol.* 53, 6320–6329. doi: 10.1021/acs.est.8b06848
- Solinst Canada Ltd., 2018. User Guide: Levellogger Series – Software version 4.3.3 [online]. Georgetown, ON, Canada. Retrieved from <https://www.solinst.com/products/dataloggers-and-telemetry/3001-levellogger-series/operating-instructions/user-guide/3001-user-guide.pdf>, Last accessed July 17, 2019]

- Stasik, S., Loick, N., Knöller, K., Weisener, C., Wendt-Potthoff, K., 2014. Understanding biogeochemical gradients of sulfur, iron and carbon in an oil sands tailings pond. *Chem. Geol.* 382, 44–53. doi: 10.1016/j.chemgeo.2014.05.026
- Stasik, S., Wick, L.Y., Wendt-Potthoff, K., 2015. Anaerobic BTEX degradation in oil sands tailings ponds: Impact of labile organic carbon and sulfate-reducing bacteria. *Chemosphere* 138, 133–139. doi: 10.1016/j.chemosphere.2015.05.068
- Stasik, S., Wendt-Potthoff, K., 2014. Interaction of microbial sulphate reduction and methanogenesis in oil sands tailings ponds. *Chemosphere* 103, 59–66. doi: 10.1016/j.chemosphere.2013.11.025
- Stasik, S., Wendt-Potthoff, K., 2016. Vertical gradients in carbon flow and methane production in a sulfate-rich oil sands tailings pond. *Water Res.* 106, 223–231. doi: 10.1016/j.watres.2016.09.053
- van Kessel, T., van Kesteren, W.G.M., 2002. Gas production and transport in artificial sludge depots. *J. Waste Manag.* 22, 19–28. doi:10.1016/S0956-053X(01)00021-6
- Wolf, L., Zwiener, C., Zemann, M., 2012. Tracking artificial sweeteners and pharmaceuticals introduced into urban groundwater by leaking sewer networks. *Sci. Tot. Environ.* 430, 8–19. doi: 10.1016/j.scitotenv.2012.04.059
- Yeh, S., Jordaan, S.M., Brandt, A.R., Turetsky, M.R., Spatari, S., Keith, D.W., 2010. Land Use Greenhouse Gas Emissions from Conventional Oil Production and Oil Sands. *Environ. Sci. Technol.* 44, 8766–8772. doi:10.1021/es1013278

APPENDIX A: AQUEOUS GEOCHEMISTRY

This section contains supplemental information of various aqueous geochemical data.

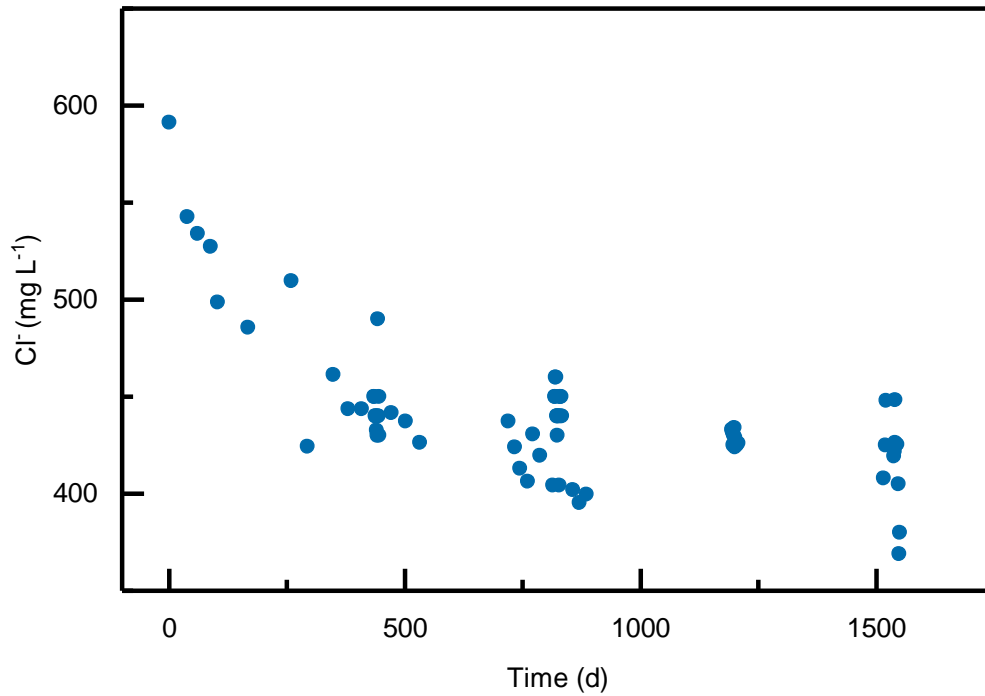


Figure A–1: Plot of water cap Cl^- concentrations over time. Data comes from Dompierre et al. (2017) and FFT sampling campaigns in 2016 and 2017. Dates with multiple values coincide with annual FFT geochemistry sampling campaigns.

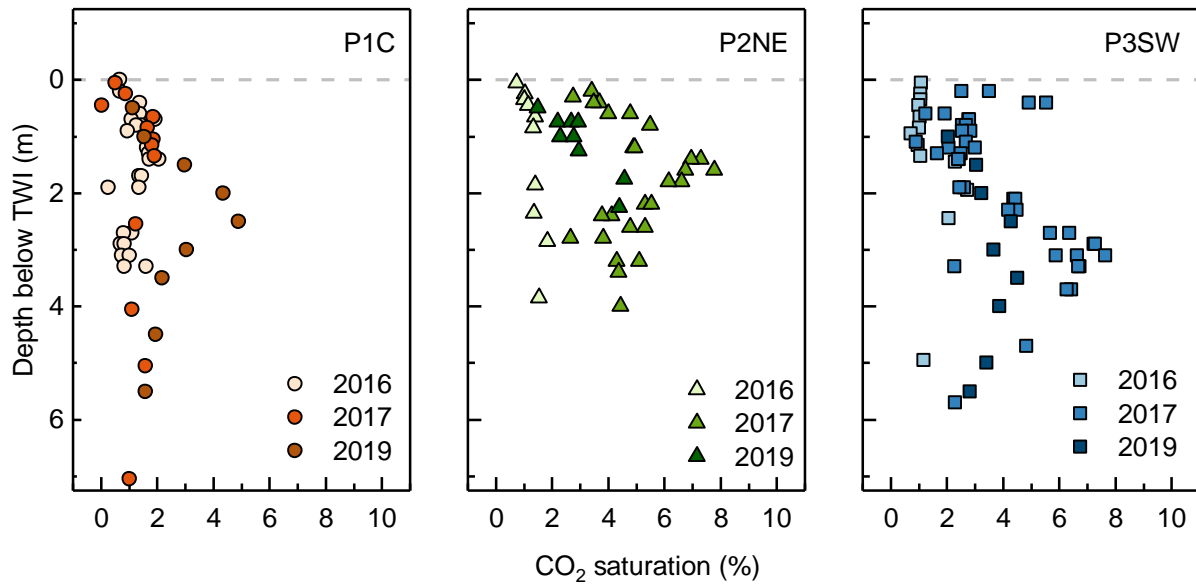


Figure A-2: Percent saturation of FFT porewater with respect to CO_{2(aq)} at all three sample locations.

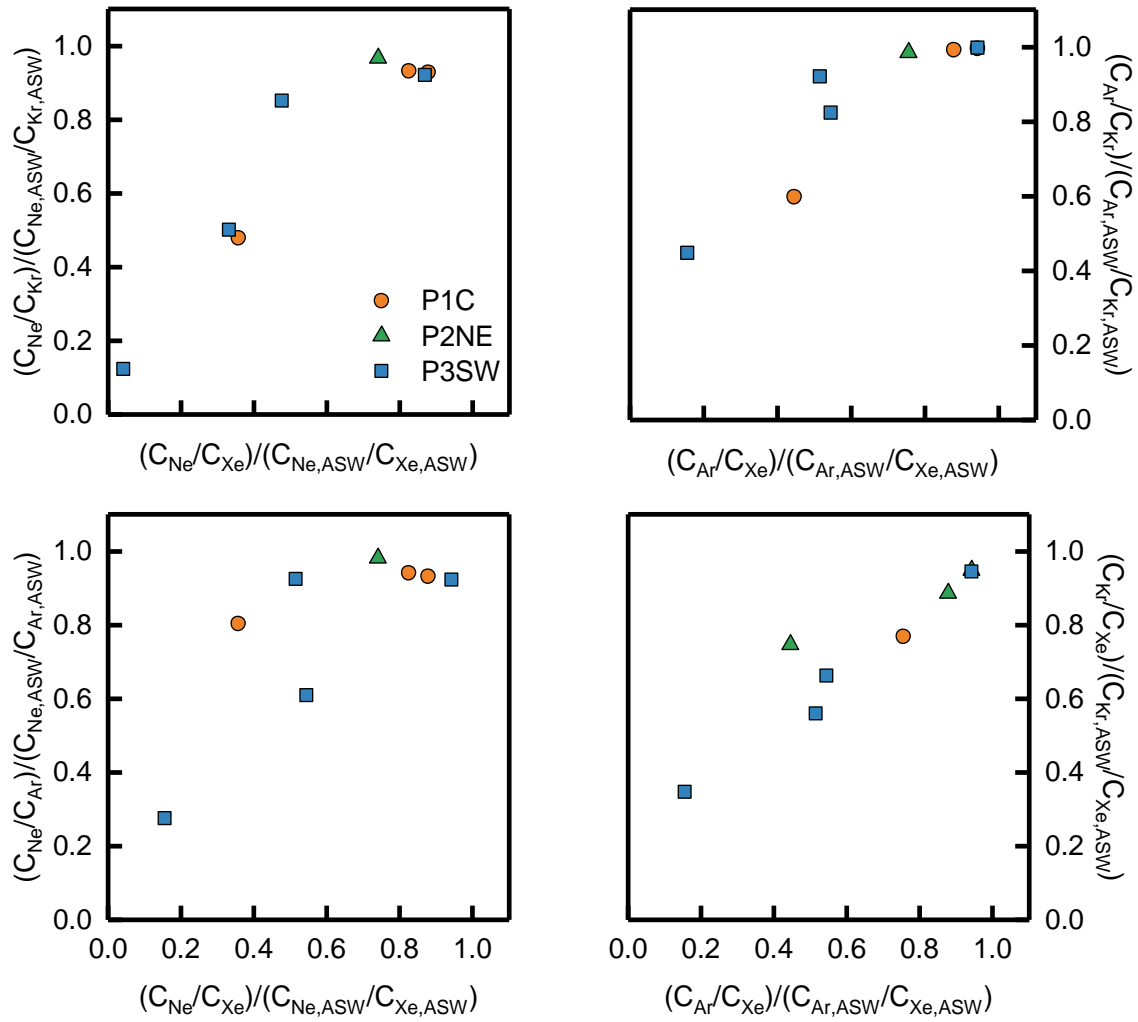


Figure A-3: Ratios of noble gases in FFT samples normalized to those of air-saturated water (ASW) at the BML water cap elevation.

Table A–1: Porewater Cl⁻ concentrations used in this study. *From Dompierre et al. (2016; 2017), Dompierre and Barbour (2016).

Depth below TWI (m)	P1C			P2NE			P3SW		
	2015*	2016	2017	2015*	2016	2017	2015*	2016	2017
Values (mg L ⁻¹)									
-0.75	440	-	-	450	-	-	430	-	-
-0.70	440	-	-	-	-	-	-	-	-
-0.65	440	-	-	-	-	430	-	-	-
-0.60	450	-	-	450	-	-	-	-	-
-0.55	430	-	-	-	-	420	-	-	-
-0.45	-	-	-	-	-	-	450	-	-
-0.40	440	430	370	-	430	430	-	430	420
-0.30	430	420	-	-	430	-	450	430	-
-0.20	-	430	380	-	430	-	440	430	-
-0.10	440	430	-	460	430	430	450	430	420
-0.05	440	-	-	-	-	430	440	-	450
0.00	-	430	420	-	430	-	530	470	-
0.10	510	470	420	580	430	430	-	520	510
0.15	540	-	-	580	-	450	450	-	560
0.20	580	510	450	600	440	470	500	560	590
0.30	570	530	490	610	470	490	560	600	610
0.40	590	550	540	450	480	500	600	620	620
0.50	590	550	550	610	490	540	670	630	620
0.60	590	550	560	630	500	560	650	640	-
0.70	580	540	550	600	510	590	640	640	640
0.80	600	540	570	600	520	-	650	640	640
0.90	570	530	560	600	530	580	650	650	630
1.00	590	550	550	620	530	-	650	650	620
1.10	580	540	-	-	530	610	670	650	-
1.20	590	530	560	580	540	-	640	640	620
1.30	570	550	-	-	530	630	650	640	-
1.40	560	540	-	590	560	570	670	640	610
1.50	-	550	550	-	570	-	670	640	-
1.60	570	550	-	-	570	-	650	640	-
1.70	560	540	-	-	570	-	640	600	-
1.80	560	550	-	600	550	-	-	620	-
1.90	-	540	-	-	550	620	610	590	-
2.00	570	540	570	570	590	-	620	580	600
2.10	550	550	-	570	590	-	-	580	-
2.20	550	540	-	-	550	-	610	530	-
2.30	540	-	-	580	-	650	610	-	-
2.40	-	540	-	-	590	-	-	580	590

Depth below TWI (m)	P1C			P2NE			P3SW		
	2015*	2016	2017	2015*	2016	2017	2015*	2016	2017
Values (mg L ⁻¹)									
2.50	-	-	560	-	-	-	-	-	-
2.60	-	550	-	-	600	-	-	580	-
2.80	550	550	-	-	590	610	-	580	-
2.90	-	-	-	590	-	-	-	-	-
3.00	-	540	570	-	600	-	600	570	590
3.50	-	550	-	-	610	-	-	580	-
3.80	560	-	-	-	-	610	-	-	-
4.00	-	550	590	600	610	-	580	560	580
5.00	-	-	600	580	610	-	580	-	-
5.50	-	560	-	570	-	-	-	-	-
6.00	570	-	660	560	600	630	560	550	540
7.00	670	560	720	-	-	610	-	-	550
8.00	-	-	760	-	600	600	600	570	560
9.00	-	610	820	-	-	590	-	-	570
10.00	-	-	860	-	600	650	-	570	590
10.50	-	610	-	-	-	680	-	-	670
12.00	-	-	920	-	-	650	-	-	-
14.00	-	-	950	-	-	640	-	-	780
16.00	-	-	920	-	-	650	-	-	930
18.00	-	-	680	-	-	680	-	-	1020
20.00	-	-	570	-	-	-	-	-	850
24.00	-	-	590	-	-	-	-	-	400
28.00	-	-	870	-	-	-	-	-	480
32.00	-	-	710	-	-	-	-	-	660
36.00	-	-	390	-	-	-	-	-	510
40.00	-	-	590	-	-	-	-	-	-

Table A–2: Porewater B concentrations used in this study. * From Dompierre et al. (2016).

Depth below TWI (m)	P1C			P2NE			P3SW		
	2015*	2016	2017	2015*	2016	2017	2015*	2016	2017
	Values ($\mu\text{g L}^{-1}$)								
-0.75	1560	-	-	1780	-	-	1710	-	-
-0.70	1490	-	-	-	-	-	-	-	-
-0.65	1670	-	-	-	-	1380	-	-	-
-0.60	1560	-	-	1720	-	-	-	-	-
-0.55	1570	-	-	-	-	1370	1770	-	-
-0.45	1580	-	-	-	-	1450	1750	-	1440
-0.40	-	1460	1340	-	1550	-	-	1640	-
-0.30	1640	1420	-	-	1550	-	1750	1640	-
-0.25	1580	-	-	-	-	-	1730	-	-
-0.20	1600	1400	-	-	1540	-	-	1680	-
-0.15	1700	1400	1330	1770	1580	1360	1720	1660	1550
-0.05	1580	-	-	-	-	-	1830	-	1710
0.00	-	1500	1400	-	1590	-	2340	1680	-
0.10	1910	1780	1490	2500	1560	1440	1770	1860	1980
0.20	2130	2040	1830	2480	1970	2330	1840	2080	2140
0.30	2150	2170	1580	2420	2380	2260	2030	2020	2380
0.35	-	-	-	2490	0	2400	2010	-	2410
0.40	-	2370	2240	1780	2540	-	-	1900	-
0.45	2270	-	-	2540	0	2160	2090	-	2440
0.50	2300	2280	2490	2580	2280	2350	2420	2190	2240
0.60	-	2370	2580	-	2360	-	2170	2090	-
0.70	2590	2370	2860	2420	2410	2280	2160	2070	2190
0.75	2320	-	-	2440	-	2390	1970	-	2060
0.80	2300	2340	2870	-	2480	-	-	2070	-
0.90	2430	2320	2910	2580	2510	2550	2040	1960	2160
1.00	2450	2320	2920	2450	2400	-	2050	1960	2130
1.10	2500	2290	2950	-	2450	2520	2150	1980	-
1.20	2590	1990	-	2730	2500	-	1930	1950	2270
1.25	3030	-	-	-	-	2460	1950	-	-
1.30	2890	2010	2880	-	2260	-	2240	1970	-
1.40	2250	1930	-	2690	2570	2620	2330	2040	-
1.45	2960	-	-	-	-	-	2050	-	2570
1.50	-	2010	-	-	2620	-	2320	2350	-
1.60	2740	2020	2600	-	2520	-	2230	2450	-
1.70	-	2020	-	2800	2450	-	2570	2320	-
1.80	2660	1980	-	-	2260	2400	2410	4100	-
1.90	2820	1930	-	2760	2070	-	-	3730	-
2.00	-	1960	-	-	2290	-	2750	3650	-

Depth below TWI (m)	P1C			P2NE			P3SW		
	2015*	2016	2017	2015*	2016	2017	2015*	2016	2017
	Values ($\mu\text{g L}^{-1}$)								
2.10	-	1980	2350	2750	2380	-	2820	4550	-
2.20	-	2030	-	-	2010	-	2960	2150	-
2.30	2050	-	-	2720	-	2430	3180	-	-
2.40	-	2010	-	-	2270	-	3130	4620	2660
2.60	-	1930	2400	-	2330	-	-	3940	-
2.80	2530	1920	-	-	2240	2610	-	4330	-
2.90	-	-	-	2770	-	-	-	-	-
3.00	-	1960	2470	-	2360	-	2620	2290	2540
3.50	-	1960	-	-	2450	-	-	2220	-
3.80	2460	-	-	-	-	2440	-	-	-
4.00	-	3890	3120	2840	2560	-	2730	3780	2540
5.00	3040	-	-	3120	4300	-	2620	4150	-
5.50	-	3980	-	3240	-	-	-	-	-
6.00	3240	-	3020	2390	3740	2610	2630	3840	2390
6.50	-	2880	-	-	-	-	-	-	-
7.00	2880	-	2990	-	-	2600	-	-	2450
8.00	-	-	2920	-	2550	2620	2790	4310	2920
8.50	-	4380	-	-	-	-	-	-	-
9.00	-	-	2950	-	-	2360	-	-	3110
9.50	-	-	-	-	-	-	-	-	-
10.00	-	-	3020	-	4280	2540	-	4380	3170
10.50	-	4740	-	-	-	2300	-	-	3320
12.00	-	-	2830	-	-	2240	-	-	3100
14.00	-	-	2840	-	-	2240	-	-	3300
16.00	-	-	3250	-	-	2220	-	-	3140
18.00	-	-	3210	-	-	1900	-	-	2420
20.00	-	-	3040	-	-	-	-	-	3060
24.00	-	-	2950	-	-	-	-	-	2870
28.00	-	-	2730	-	-	-	-	-	3390
32.00	-	-	2800	-	-	-	-	-	3650
36.00	-	-	2330	-	-	-	-	-	2560
40.00	-	-	2580	-	-	-	-	-	-

Table A–3: Porewater $\delta^2\text{H}$ concentrations used in this study. *From Dompierre et al. (2016) Dompierre and Barbour (2016).

Depth below TWI (m)	PIC			P2NE			P3SW		
	2015*	2016	2017	2015*	2016	2017	2015*	2016	2017
Values (‰)									
-0.75	-114.8	-	-	-114.6	-	-	-114.5	-	-
-0.70	-115.5	-	-	-	-	-	-	-	-
-0.65	-114.8	-	-	-	-	-112.3	-	-	-
-0.60	-114.8	-	-	-114.6	-	-	-	-	-
-0.55	-115.0	-	-	-	-	-112.1	-114.6	-	-
-0.45	-115.4	-	-	-	-	-112.0	-115.2	-	-110.8
-0.40	-	-112.6	-111.4	-	-117.0	-	-114.6	-112.7	-
-0.30	-114.8	-113.2	-	-	-114.4	-	-114	-113.1	-
-0.20	-115.6	-112.3	-	-	-112.0	-112.0	-114.5	-114.8	-111.7
-0.10	-115.0	-111.1	-110.9	-114.8	-110.1	-111.2	-114.7	-113.8	-111.8
0.00	-114.7	-111.6	-111.6	-115.3	-110.4	-111.3	-113.8	-112.8	-110.5
0.10	-114.8	-112.0	-111.1	-114.3	-112.3	-111.1	-115.4	-111.6	-111.4
0.20	-114.0	-111.4	-110.7	-112.8	-113.0	-111.4	-115.1	-111.5	-110.7
0.30	-111.3	-111.0	-111.4	-113.0	-111.6	-112.0	-114.8	-110.1	-111.2
0.40	-111.2	-112.1	-112.0	-113.1	-112.3	-111.2	-113.7	-110.2	-111.4
0.50	-111.3	-111.3	-111.5	-112.5	-113.1	-111.4	-110.5	-110.5	-
0.60	-111.8	-112.3	-111.0	-112.0	-110.3	-111.2	-111.4	-110.7	-110.8
0.70	-111.4	-110.6	-111.3	-128.3	-110.4	-111.5	-111.3	-110.2	-111.5
0.75	-109.8	-	-	-111.3	-	-111	-111.3	-	-
0.80	-112.8	-111.7	-110.9	-112.7	-112.3	-111	-111.7	-110.7	-111.4
0.90	-112.7	-111.6	-111.9	-	-113.2	-	-112.1	-109.7	-111.2
1.00	-112.2	-112.5	-112.1	-112.4	-112.8	-111	-110.9	-110.1	-111.1
1.10	-113.4	-113.4	-110.9	-	-113.2	-	-112.4	-109.2	-
1.20	-114.3	-113.3	-	-112.4	-115.0	-110.6	-112.5	-112.0	-111.3
1.30	-113.6	-112.5	-112.1	-112.1	-113.0	-113.2	-112.2	-	-
1.40	-114.8	-113.3	-	-	-113.4	-	-112.4	-111.2	-112.1
1.50	-	-113.4	-	-	-111.5	-	-112.7	-112.5	-
1.60	-	-112.9	-111.7	-	-111.3	-	-111.0	-111.9	-
1.70	-115.1	-112.8	-	-	-111.5	-	-112.6	-111.8	-
1.80	-114.2	-	-	-111.9	-111.1	-	-	-110.4	-
1.90	-112.2	-112.2	-	-111.8	-111.3	-110.2	-112.1	-112.8	-112.8
2.00	-	-111.5	-	-111.5	-111.7	-	-112.8	-112.4	-
2.10	-	-	-112.9	-	-111.8	-	-112.1	-112.4	-
2.20	-114.0	-111.9	-	-	-110.0	-	-	-110.6	-
2.40	-	-112.9	-	-112.1	-111.8	-111.6	-112.1	-111.6	-
2.50	-	-	-113.0	-	-	-	-112.9	-	-113.4
2.60	-	-111.1	-	-	-112.8	-	-	-111.4	-

Depth below TWI (m)	P1C			P2NE			P3SW		
	2015*	2016	2017	2015*	2016	2017	2015*	2016	2017
	Values (‰)								
2.80	-114.1	-109.9	-	-	-112.5	-111.8	-	-112.4	-
2.90	-	-	-	-110.2	-	-	-	-	-
3.00	-	-110.2	-112.4	-	-110.6	-	-113.0	-	-113.5
3.50	-	-110.7	-	-	-111.9	-	-	-	-
3.80	-113.4	-	-	-	-	-112.6	-	-	-
4.00	-	-111.5	-112.6	-111.4	-111.8	-	-112.7	-113.4	-113.0
5.00	-113.1	-	-114.9	-111.8	-110.9	-110.1	-113.6	-111.6	-111.9
5.50	-	-112.6	-	-	-	-	-	-	-
6.00	-113.0	-	-115.6	-112.6	-111	-111.5	-113.3	-111.9	-111.9
6.50	-	-112.7	-	-	-	-	-	-	-
7.00	-	-	-114.9	-	-	-111.2	-	-	-113.2
8.00	-	-	-114.8	-	-111.8	-110.9	-113.6	-113.9	-112.3
8.50	-	-111.7	-	-	-	-	-	-	-
9.00	-	-	-117.1	-	-	-111.9	-	-	-112.6
9.50	-	-	-	-	-	-	-	-	-
10.00	-	-	-115.4	-	-111.3	-111.5	-	-112.5	-113.1
10.50	-	-115.2	-	-	-	-111.6	-	-	-114.9
12.00	-	-	-118.4	-	-	-110.4	-	-	-
14.00	-	-	-118.5	-	-	-110.0	-	-	-116.9
16.00	-	-	-114.0	-	-	-110.6	-	-	-117.7
18.00	-	-	-113.0	-	-	-110.0	-	-	-119.8
20.00	-	-	-113.7	-	-	-	-	-	-117.1
24.00	-	-	-116.8	-	-	-	-	-	-119.1
28.00	-	-	-115.8	-	-	-	-	-	-114.3
32.00	-	-	-118.5	-	-	-	-	-	-116.3
36.00	-	-	-114.0	-	-	-	-	-	-
40.00	-	-	-117.8	-	-	-	-	-	-

Table A–4: Porewater $\delta^{18}\text{O}$ concentrations used in this study. *From Dompierre et al. (2016) Dompierre and Barbour (2016).

$\delta^{18}\text{O}$ Data Depth below TWI (m)	P1C			P2NE			P3SW		
	2015*	2016	2017	2015*	2016	2017	2015*	2016	2017
	Values (‰)								
-0.75	-12.70	-	-	-12.56	-	-	-12.55	-	-
-0.70	-12.61	-	-	-	-	-	-	-	-
-0.65	-12.62	-	-	-	-	-11.96	-	-	-
-0.60	-12.31	-	-	-12.57	-	-	-12.6	-	-
-0.55	-12.60	-	-	-	-	-12.02	-12.50	-	-
-0.40	-12.75	-12.41	-12.09	-	-14.2	-11.94	-12.62	-12.15	-11.89
-0.30	-12.52	-12.54	-	-	-13.18	-	-12.37	-12.09	-
-0.20	-12.66	-12.26	-	-	-12.22	-12.16	-12.42	-12.87	-12.04
-0.10	-12.58	-12.08	-11.84	-12.49	-11.54	-11.89	-12.64	-12.65	-12.01
0.00	-12.49	-12.25	-11.9	-12.7	-11.57	-11.83	-12.50	-12.42	-11.93
0.10	-12.69	-12.28	-11.75	-12.44	-12.12	-12.04	-12.64	-12.27	-12.14
0.20	-12.47	-12.35	-12.17	-12.07	-12.65	-12.02	-12.67	-12.28	-12.06
0.30	-12.28	-12.35	-12.31	-12.42	-12.07	-12.3	-12.75	-12.19	-12.24
0.40	-12.31	-12.41	-12.55	-12.52	-12.27	-12.38	-12.53	-12.15	-12.19
0.50	-12.48	-12.42	-12.32	-12.41	-12.57	-12.39	-12.36	-12.02	-12.26
0.60	-12.56	-12.40	-12.39	-12.39	-11.88	-12.32	-12.14	-12.08	-12.29
0.70	-12.29	-11.65	-12.48	-16.07	-11.98	-12.46	-12.26	-12.08	-12.39
0.80	-12.36	-12.43	-12.3	-12.24	-12.15	-12.21	-12.30	-12.19	-12.44
0.90	-12.63	-12.31	-12.4	-12.71	-12.45	-12.21	-12.18	-12.16	-12.33
1.00	-12.75	-12.46	-12.36	-12.61	-12.40	-12.41	-12.19	-12.18	-12.32
1.10	-12.46	-12.34	-11.82	-	-12.45	-	-12.16	-11.82	-
1.20	-12.80	-12.46	-	-12.64	-13.01	-	-12.31	-12.16	-12.37
1.30	-12.81	-12.50	-12.23	-	-12.56	-12.37	-12.38	-	-
1.40	-12.54	-12.47	-	-12.54	-12.41	-12.63	-12.28	-12.24	-
1.50	-12.99	-12.43	-	-	-12.29	-	-12.30	-12.35	-12.44
1.60	-13.07	-12.52	-12.04	-	-12.2	-	-12.44	-12.19	-
1.70	-	-12.50	-	-12.44	-12.37	-	-11.97	-12.32	-
1.80	-12.65	-	-	-	-12.31	-	-12.30	-11.53	-
1.90	-11.82	-12.50	-	-	-12.16	-11.88	-12.42	-12.32	-
2.00	-	-12.40	-	-12.40	-12.27	-	-12.48	-12.30	-12.6
2.10	-	-	-12.42	-12.18	-12.36	-	-12.43	-12.35	-
2.20	-12.54	-12.41	-	-	-12.22	-	-12.46	-12.11	-
2.40	-	-12.33	-	-12.52	-12.41	-12.43	-	-12.35	-
2.50	-	-	-12.44	-	-	-	-12.62	-	-12.52
2.60	-	-12.29	-	-	-12.55	-	-	-12.34	-
2.80	-12.61	-12.07	-	-	-12.35	-12.47	-	-12.61	-
2.90	-	-	-	-12.16	-	-	-	-	-

$\delta^{18}\text{O}$ Data Depth below TWI (m)	P1C			P2NE			P3SW		
	2015*	2016	2017	2015*	2016	2017	2015*	2016	2017
	Values (‰)								
3.00	-	-12.17	-11.98	-	-12.33	-	-12.11	-	-12.49
3.50	-	-12.06	-	-	-12.44	-	-	-	-
3.80	-12.45	-	-	-	-	-12.52	-	-	-
4.00	-	-12.14	-12.05	-12.30	-12.31	-	-12.01	-12.59	-12.40
5.00	-12.34	-	-12.51	-12.28	-12.32	-11.92	-12.44	-12.22	-12.04
5.50	-	-12.28	-	-	-	-	-	-	-
6.00	-12.43	-	-12.46	-12.47	-12.16	-12.45	-12.16	-12.07	-12.03
6.50	-	-12.32	-	-	-	-	-	-	-
7.00	-	-	-12.10	-	-	-12.33	-	-	-12.39
8.00	-	-	-12.10	-	-12.45	-12.23	-12.30	-12.45	-12.26
8.50	-	-11.94	-	-	-	-	-	-	-
9.00	-	-	-12.83	-	-	-12.58	-	-	-12.26
9.50	-	-	-	-	-	-	-	-	-
10.00	-	-	-12.14	-	-12.15	-12.57		-12.52	-12.45
10.50	-	-12.61	-	-	-	-12.61	-	-	-12.60
12.00	-	-	-13.13	-	-	-12.50	-	-	-
14.00	-	-	-13.19	-	-	-12.25	-	-	-12.96
16.00	-	-	-12.41	-	-	-12.60	-	-	-12.98
18.00	-	-	-12.38	-	-	-12.47	-	-	-13.56
20.00	-	-	-12.50	-	-	-	-	-	-13.00
24.00	-	-	-12.94	-	-	-	-	-	-13.70
28.00	-	-	-12.85	-	-	-	-	-	-12.56
32.00	-	-	-13.35	-	-	-	-	-	-12.93
36.00	-	-	-12.48	-	-	-	-	-	-
40.00	-	-	-13.13	-	-	-	-	-	-

Table A–5: Porewater CH_{4(aq)} concentrations used in this study. *From Dompierre et al. (2016) Dompierre and Barbour (2016).

CH _{4(aq)} Data Depth below TWI (m)	P1C			P2NE			P3SW		
	2016	2017	2019	2016	2017	2019	2016	2017	2019
Values (mg L ⁻¹)									
-0.7	-	-	-	-	0.39	-	-	-	-
-0.5	-	-	-	-	0.39	-	-	-	-
-0.4	-	-	--	-	-	-	0.90	0.25	-
-0.3	0.55	0.37	-	-	0.40	-	0.91	0.24	-
-0.2	0.98	-	-	-	-	-	0.87	4.25	-
-0.1	1.20	0.38	-	-	-	-	1.30	-	-
0.0	2.00	2.34	-	-	2.31	-	26.47	27.17	-
0.2	2.58	26.82	-	9.93	9.34	-	19.51	34.48	-
0.3	-	-	-	7.89	21.83	-	26.21	44.28	-
0.4	22.47	0.27	-	19.57	31.62	-	31.36	47.65	-
0.5	21.44	-	46.01	18.74	-	21.25	16.72	-	-
0.6	31.86	42.98	-	28.41	37.29	-	10.32	41.38	-
0.7	43.28	-	-	25.10	-	-	23.46	-	-
0.8	37.07	38.06	-	41.83	71.26	33.33	23.99	30.22	-
0.9	39.19	-	-	42.23	-	35.85	24.23	34.20	-
1.0	31.04	37.05	51.23	-	-	31.18	26.06	-	35.36
1.1	40.87	39.01	-	-	-	36.30	22.64	53.61	-
1.2	40.70	-	-	38.30	-	-	20.25	-	-
1.3	40.57	54.21	-	38.67	-	47.51	27.92	39.35	-
1.4	52.80	-	-	66.09	-	-	36.10	44.63	-
1.5	62.68	-	48.95	62.98	-	-	24.59	-	49.17
1.6	-	-	-	66.76	-	-	44.57	-	-
1.7	54.13	-	-	57.88	-	-	35.66	-	-
1.8	37.78	-	-	67.93	50.68	-	36.42	-	-
1.9	7.02	-	-	63.80	-	61.06	54.41	68.64	-
2.0	59.52	-	53.48	-	-	-	52.75	-	47.91
2.1	-	-	-	-	-	-	41.27	-	-
2.1	-	-	-	-	-	-	48.26	-	-
2.2	-	-	-	68.08	-	-	-	-	-
2.3	-	-	-	70.16	45.75	63.34	44.36	-	-
2.4	-	-	-	58.33	-	-	42.05	38.52	-
2.5	-	33.73	46.70	54.30	-	-	-	-	51.34
2.6	-	-	-	79.62	-	-	-	-	-
2.7	53.35	-	-	71.54	-	-	47.84	-	-
2.8	51.25	-	-	35.36	71.84	-	43.17	-	-
2.9	45.60	-	-	49.55	-	-	48.86	-	-

CH _{4(aq)} Data Depth below TWI (m)	P1C			P2NE			P3SW		
	2016	2017	2019	2016	2017	2019	2016	2017	2019
Values (mg L ⁻¹)									
3.0	59.73	-	39.74	-	-	-	49.95	-	53.42
3.1	54.84	-	-	-	-	-	59.70	-	-
3.2	50.90	-	-	64.14	-	-	52.33	-	-
3.2	-	-	-	53.66	-	-	46.32	-	-
3.3	48.52	-	-	-	-	-	57.75	-	-
3.4	64.40	-	-	60.97	-	-	16.42	-	-
3.5	-	-	19.03	-	-	-	49.65	-	61.59
3.7	-	-	-	-	-	-	52.79	-	-
3.8	-	-	-	-	52.29	-	50.96	-	-
4.0	-	34.41	-	60.33	-	-	-	-	57.29
4.5	-	-	17.80	-	-	-	-	-	-
4.7	-	-	-	-	-	-	41.47	-	-
4.9	-	-	-	-	-	-	-	17.06	-
5.0	-	38.23	-	-	-	-	-	-	55.17
5.5	-	-	22.77	-	-	-	-	-	59.70
5.7	-	-	-	-	-	-	26.22	-	-
6.8	-	37.91	-	-	-	-	-	-	-

APPENDIX B: SENSOR DESIGN

Diffusion tests were run using the P_{TDG} sensor in the Tygon tubing without a PVC housing in a soil moisture extractor filled with water and applied headspace of 275 kPa of CO_2 . The test was only run for 3 days. A modelled diffusion coefficient was calculated using the data from the test and indicates an equilibration time of 5 days. To simulate the effect of the PVC housing, a 1% factor was applied to the diffusion coefficient of the P_{TDG} housing. The PVC housing effect resulted in an equilibration time of ~150 days, which closely matches the deployment time for the 2019 season.

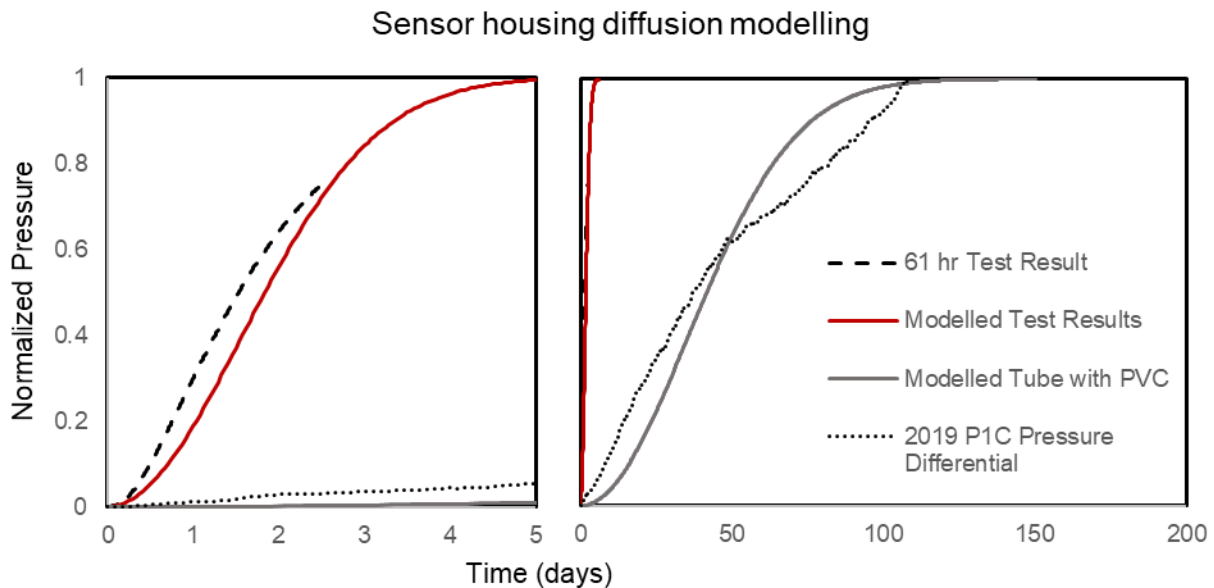


Figure B-1: Plots of pressure over time comparing the measured values in a 61 hr test to modelled results for the tubing and simulated effects of the PVC housing compared to the pressure differential results from P1C in 2019.

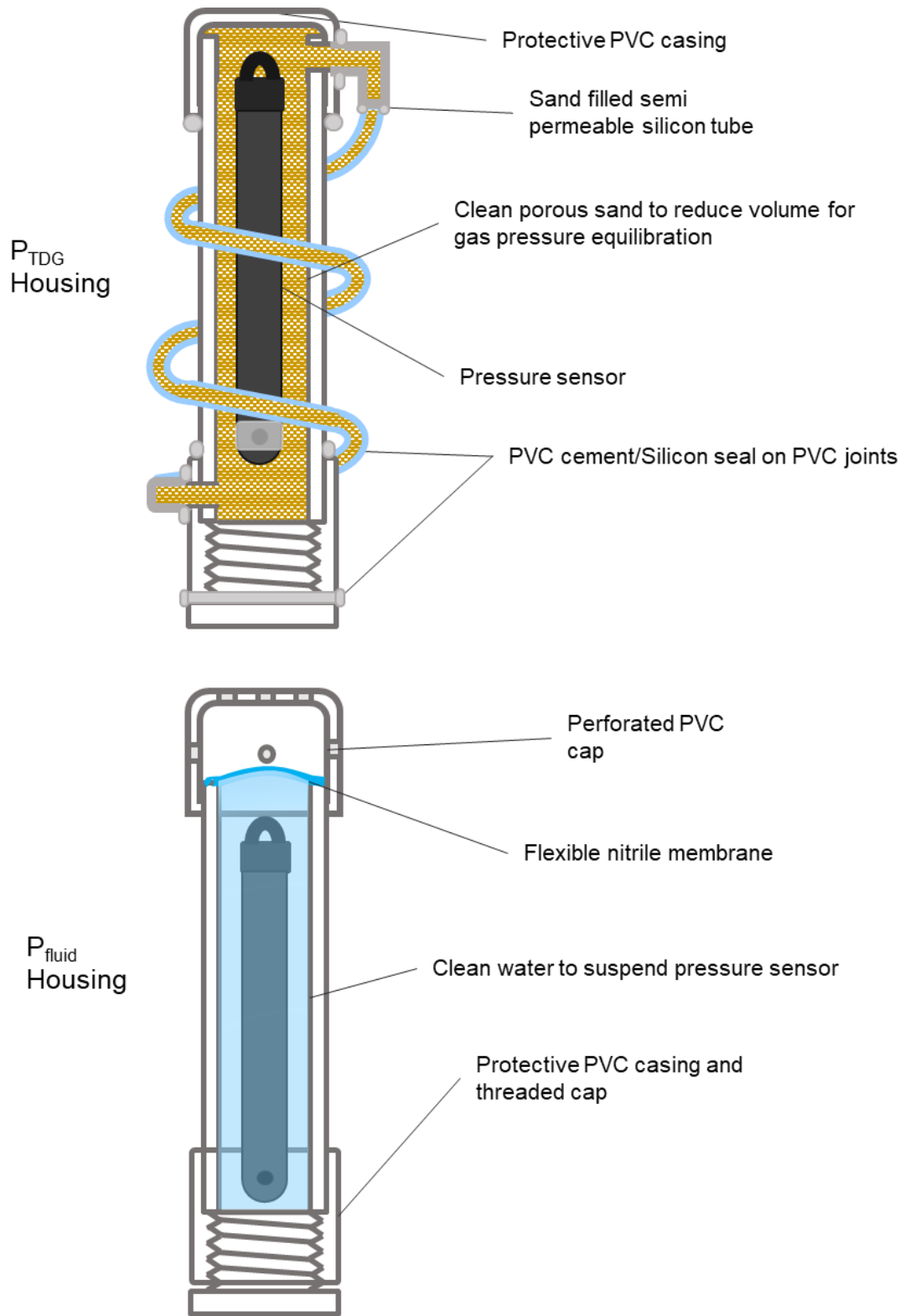


Figure B–2: Pressure sensor housing design for the 2018 deployment.

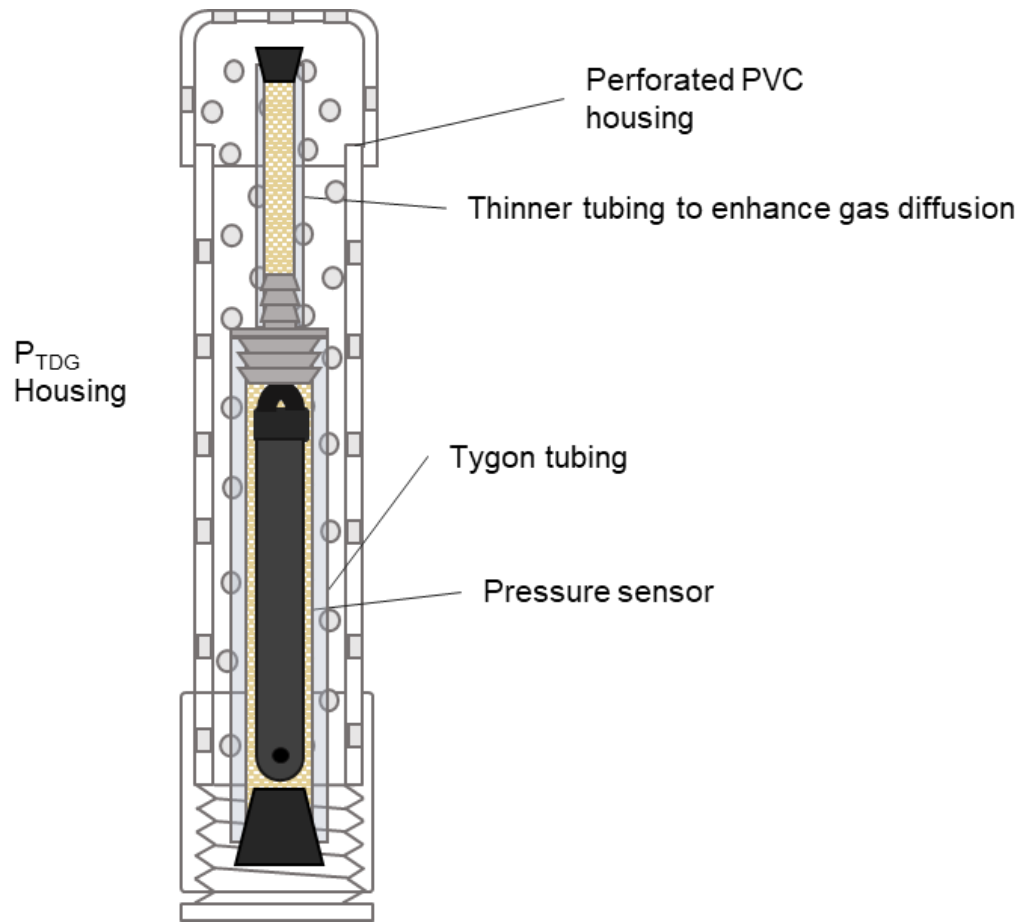


Figure B-3: P_{TDG} sensor housing design for 2019 pressure survey period.

APPENDIX C: TRANSPORT MODEL DATA

Table B-1: Best fit simulated Cl^- concentrations for location P1C in 2015, 2016 and 2017.

Location	Depth (m below TWI)	Simulated Cl^- (mg L^{-1})		
		2015	2016	2017
P1C	0.00	430	428	417
P1C	0.02	443	438	427
P1C	0.04	455	448	437
P1C	0.06	466	458	446
P1C	0.08	477	467	454
P1C	0.10	487	476	462
P1C	0.12	496	484	470
P1C	0.13	505	492	477
P1C	0.15	513	499	484
P1C	0.17	521	505	490
P1C	0.19	528	512	496
P1C	0.21	535	517	502
P1C	0.23	541	523	507
P1C	0.25	546	528	511
P1C	0.30	559	539	522
P1C	0.35	568	547	530
P1C	0.40	575	553	537
P1C	0.45	580	558	542
P1C	0.50	584	561	546
P1C	0.55	586	564	548
P1C	0.60	588	565	550
P1C	0.65	588	565	551
P1C	0.70	589	565	552
P1C	0.75	589	565	553
P1C	0.80	588	565	553
P1C	0.85	587	564	553
P1C	0.90	587	563	553
P1C	0.95	585	562	552
P1C	1.00	584	561	552
P1C	1.05	583	560	552
P1C	1.10	581	559	552
P1C	1.15	580	558	552
P1C	1.20	578	557	551
P1C	1.25	576	556	551
P1C	1.30	575	556	551
P1C	1.35	573	555	551
P1C	1.40	571	554	551
P1C	1.45	569	554	551

Location	Depth (m below TWI)	Simulated Cl ⁻ (mg L ⁻¹)		
		2015	2016	2017
P1C	1.50	568	553	550
P1C	1.55	566	553	550
P1C	1.60	564	552	550
P1C	1.65	562	552	550
P1C	1.70	561	551	550
P1C	1.75	559	551	550
P1C	1.80	558	551	550
P1C	1.85	557	551	550
P1C	1.90	555	551	550
P1C	1.95	554	550	550
P1C	2.00	554	550	550
P1C	2.10	552	550	550
P1C	2.20	551	550	550
P1C	2.30	550	550	550
P1C	2.40	550	550	550
P1C	2.50	550	550	550
P1C	2.60	550	550	550
P1C	2.70	550	550	550
P1C	2.80	550	550	550
P1C	2.90	550	550	550
P1C	3.00	550	550	550
P1C	3.10	550	550	550
P1C	3.20	550	550	550
P1C	3.30	550	550	550
P1C	3.40	550	550	550
P1C	3.50	550	550	550
P1C	3.60	550	550	550
P1C	3.70	550	550	550
P1C	3.80	550	550	550
P1C	3.90	550	550	550
P1C	4.00	550	550	550
P1C	4.10	550	550	550
P1C	4.20	550	550	550
P1C	4.30	550	550	550
P1C	4.40	550	550	550
P1C	4.50	550	550	550
P1C	4.60	550	550	550
P1C	4.70	550	550	550
P1C	4.80	550	550	550
P1C	4.90	550	550	550
P1C	5.00	550	550	550

Table B-2: Best fit simulated Cl⁻ concentrations for location P2NE in 2015, 2016 and 2017.

Location	Depth (m below TWI)	Simulated Cl ⁻ (mg L ⁻¹)		
		2015	2016	2017
P2NE	0.00	430	428	417
P2NE	0.02	442	433	423
P2NE	0.04	453	438	428
P2NE	0.06	463	443	433
P2NE	0.08	473	447	438
P2NE	0.10	483	452	443
P2NE	0.12	492	457	448
P2NE	0.13	500	462	453
P2NE	0.15	508	466	458
P2NE	0.17	516	471	462
P2NE	0.19	523	475	467
P2NE	0.21	529	480	472
P2NE	0.23	536	484	476
P2NE	0.25	541	488	481
P2NE	0.30	554	499	492
P2NE	0.35	565	509	502
P2NE	0.40	573	518	512
P2NE	0.45	580	527	521
P2NE	0.50	585	535	529
P2NE	0.55	588	542	537
P2NE	0.60	591	548	544
P2NE	0.65	594	555	550
P2NE	0.70	595	560	556
P2NE	0.75	597	565	561
P2NE	0.80	597	569	566
P2NE	0.85	598	573	570
P2NE	0.90	599	577	574
P2NE	0.95	599	580	578
P2NE	1.00	599	583	581
P2NE	1.05	600	585	583
P2NE	1.10	600	587	586
P2NE	1.15	600	589	588
P2NE	1.20	600	591	590
P2NE	1.25	600	592	591
P2NE	1.30	600	593	592
P2NE	1.35	600	594	593
P2NE	1.40	600	595	594
P2NE	1.45	600	596	595
P2NE	1.50	600	597	596
P2NE	1.55	600	597	597

Location	Depth (m below TWI)	Simulated Cl ⁻ (mg L ⁻¹)		
		2015	2016	2017
P2NE	1.60	600	598	597
P2NE	1.65	600	598	598
P2NE	1.70	600	598	598
P2NE	1.75	600	599	598
P2NE	1.80	600	599	599
P2NE	1.85	600	599	599
P2NE	1.90	600	599	599
P2NE	1.95	600	599	599
P2NE	2.00	600	599	599
P2NE	2.10	600	600	599
P2NE	2.20	600	600	600
P2NE	2.30	600	600	600
P2NE	2.40	600	600	600
P2NE	2.50	600	600	600
P2NE	2.60	600	600	600
P2NE	2.70	600	600	600
P2NE	2.80	600	600	600
P2NE	2.90	600	600	600
P2NE	3.00	600	600	600
P2NE	3.10	600	600	600
P2NE	3.20	600	600	600
P2NE	3.30	600	600	600
P2NE	3.40	600	600	600
P2NE	3.50	600	600	600
P2NE	3.60	600	600	600
P2NE	3.70	600	600	600
P2NE	3.80	600	600	600
P2NE	3.90	600	600	600
P2NE	4.00	600	600	600
P2NE	4.10	600	600	600
P2NE	4.20	600	600	600
P2NE	4.30	600	600	600
P2NE	4.40	600	600	600
P2NE	4.50	600	600	600
P2NE	4.60	600	600	600
P2NE	4.70	600	600	600
P2NE	4.80	600	600	600
P2NE	4.90	600	600	600
P2NE	5.00	600	600	600

Table B-3: Best fit simulated Cl⁻ concentrations for location P3SW in 2015, 2016 and 2017.

Location	Depth (m below TWI)	Simulated Cl ⁻ (mg L ⁻¹)		
		2015	2016	2017
P3SW	0.00	430	428	417
P3SW	0.02	464	446	436
P3SW	0.04	493	463	454
P3SW	0.06	518	480	471
P3SW	0.08	538	495	486
P3SW	0.10	556	509	500
P3SW	0.12	571	522	514
P3SW	0.13	584	534	526
P3SW	0.15	595	545	537
P3SW	0.17	604	555	548
P3SW	0.19	611	565	557
P3SW	0.21	618	573	566
P3SW	0.23	623	581	574
P3SW	0.25	628	588	581
P3SW	0.30	636	603	596
P3SW	0.35	642	615	608
P3SW	0.40	645	623	616
P3SW	0.45	647	630	622
P3SW	0.50	648	634	627
P3SW	0.55	649	637	629
P3SW	0.60	649	639	631
P3SW	0.65	649	640	632
P3SW	0.70	649	641	632
P3SW	0.75	649	641	632
P3SW	0.80	648	640	631
P3SW	0.85	648	639	630
P3SW	0.90	647	638	629
P3SW	0.95	647	637	627
P3SW	1.00	646	635	625
P3SW	1.05	645	633	624
P3SW	1.10	643	631	622
P3SW	1.15	642	629	620
P3SW	1.20	640	627	618
P3SW	1.25	638	625	616
P3SW	1.30	635	623	615
P3SW	1.35	633	621	613
P3SW	1.40	630	619	611
P3SW	1.45	627	617	610

Location	Depth (m below TWI)	Simulated Cl ⁻ (mg L ⁻¹)		
		2015	2016	2017
P3SW	1.50	625	615	609
P3SW	1.55	622	613	607
P3SW	1.60	619	611	606
P3SW	1.65	616	609	605
P3SW	1.70	614	608	604
P3SW	1.75	611	607	604
P3SW	1.80	609	605	603
P3SW	1.85	607	604	602
P3SW	1.90	606	603	602
P3SW	1.95	604	603	602
P3SW	2.00	603	602	601
P3SW	2.10	602	601	601
P3SW	2.20	601	601	600
P3SW	2.30	600	600	600
P3SW	2.40	600	600	600
P3SW	2.50	600	600	600
P3SW	2.60	600	600	600
P3SW	2.70	600	600	600
P3SW	2.80	600	600	600
P3SW	2.90	600	600	600
P3SW	3.00	600	600	600
P3SW	3.10	600	600	600
P3SW	3.20	600	600	600
P3SW	3.30	600	600	600
P3SW	3.40	600	600	600
P3SW	3.50	600	600	600
P3SW	3.60	600	600	600
P3SW	3.70	600	600	600
P3SW	3.80	600	600	600
P3SW	3.90	600	600	600
P3SW	4.00	600	600	600
P3SW	4.10	600	600	600
P3SW	4.20	600	600	600
P3SW	4.30	600	600	600
P3SW	4.40	600	600	600
P3SW	4.50	600	600	600
P3SW	4.60	600	600	600
P3SW	4.70	600	600	600
P3SW	4.80	600	600	600
P3SW	4.90	600	600	600
P3SW	5.00	600	600	600

Table B-4: Best fit simulated B concentrations for location P1C in 2015, 2016 and 2017.

Location	Depth (m below TWI)	Simulated B ($\mu\text{g L}^{-1}$)		
		2015	2016	2017
P1C	0.00	1400	1400	1500
P1C	0.02	1486	1482	1533
P1C	0.04	1568	1559	1566
P1C	0.06	1645	1632	1598
P1C	0.08	1718	1701	1629
P1C	0.10	1787	1766	1660
P1C	0.12	1851	1827	1690
P1C	0.15	1967	1938	1749
P1C	0.17	2019	1988	1777
P1C	0.19	2067	2034	1805
P1C	0.21	2111	2077	1832
P1C	0.23	2152	2117	1859
P1C	0.25	2190	2153	1884
P1C	0.30	2274	2236	1948
P1C	0.35	2339	2301	2007
P1C	0.40	2390	2353	2062
P1C	0.45	2428	2392	2112
P1C	0.50	2456	2422	2158
P1C	0.55	2476	2445	2200
P1C	0.60	2490	2462	2238
P1C	0.65	2500	2474	2272
P1C	0.70	2507	2483	2302
P1C	0.75	2511	2489	2329
P1C	0.80	2513	2493	2353
P1C	0.85	2514	2496	2374
P1C	0.90	2514	2498	2393
P1C	0.95	2514	2499	2409
P1C	1.00	2513	2500	2423
P1C	1.05	2512	2501	2436
P1C	1.10	2510	2501	2446
P1C	1.15	2509	2501	2456
P1C	1.20	2508	2501	2464
P1C	1.25	2507	2501	2470
P1C	1.30	2506	2501	2476
P1C	1.35	2505	2501	2480
P1C	1.40	2504	2501	2484
P1C	1.45	2503	2500	2487
P1C	1.50	2503	2500	2490
P1C	1.55	2502	2500	2492
P1C	1.60	2502	2500	2493

Location	Depth (m below TWI)	Simulated B ($\mu\text{g L}^{-1}$)		
		2015	2016	2017
P1C	1.65	2501	2500	2494
P1C	1.70	2501	2500	2496
P1C	1.75	2501	2500	2496
P1C	1.80	2501	2500	2497
P1C	1.85	2500	2500	2498
P1C	1.90	2500	2500	2498
P1C	1.95	2500	2500	2498
P1C	2.00	2500	2500	2499
P1C	2.10	2500	2500	2499
P1C	2.20	2500	2500	2500
P1C	2.30	2500	2500	2500
P1C	2.40	2500	2500	2500
P1C	2.50	2500	2500	2500
P1C	2.60	2500	2500	2500
P1C	2.70	2500	2500	2500
P1C	2.80	2500	2500	2500
P1C	2.90	2500	2500	2500
P1C	3.00	2500	2500	2500
P1C	3.10	2500	2500	2500
P1C	3.20	2500	2500	2500
P1C	3.30	2500	2500	2500
P1C	3.40	2500	2500	2500
P1C	3.50	2500	2500	2500
P1C	3.60	2500	2500	2500
P1C	3.70	2500	2500	2500
P1C	3.80	2500	2500	2500
P1C	3.90	2500	2500	2500
P1C	4.00	2500	2500	2500
P1C	4.10	2500	2500	2500
P1C	4.20	2500	2500	2500
P1C	4.30	2500	2500	2500
P1C	4.40	2500	2500	2500
P1C	4.50	2500	2500	2500
P1C	4.60	2500	2500	2500
P1C	4.70	2500	2500	2500
P1C	4.80	2500	2500	2500
P1C	4.90	2500	2500	2500
P1C	5.00	2500	2500	2500

Table B-5: Best fit simulated B concentrations for location P2NE in 2015, 2016 and 2017.

Location	Depth (m below TWI)	Simulated B ($\mu\text{g L}^{-1}$)		
		2015	2016	2017
P2NE	0.00	1500	1500	1500
P2NE	0.02	2020	1533	1532
P2NE	0.04	2226	1565	1563
P2NE	0.06	2359	1597	1595
P2NE	0.08	2445	1629	1625
P2NE	0.10	2500	1660	1655
P2NE	0.12	2535	1690	1685
P2NE	0.13	2558	1720	1714
P2NE	0.15	2573	1750	1743
P2NE	0.17	2583	1779	1771
P2NE	0.19	2589	1807	1799
P2NE	0.21	2593	1835	1826
P2NE	0.23	2595	1862	1852
P2NE	0.25	2597	1889	1879
P2NE	0.30	2599	1955	1944
P2NE	0.35	2600	2017	2005
P2NE	0.40	2600	2075	2062
P2NE	0.45	2600	2129	2116
P2NE	0.50	2600	2179	2165
P2NE	0.55	2600	2224	2211
P2NE	0.60	2600	2266	2253
P2NE	0.65	2600	2304	2292
P2NE	0.70	2600	2339	2327
P2NE	0.75	2600	2370	2359
P2NE	0.80	2600	2399	2388
P2NE	0.85	2600	2424	2414
P2NE	0.90	2600	2447	2438
P2NE	0.95	2600	2467	2459
P2NE	1.00	2600	2485	2478
P2NE	1.05	2600	2501	2494
P2NE	1.10	2600	2515	2509
P2NE	1.15	2600	2528	2523
P2NE	1.20	2600	2539	2534
P2NE	1.25	2600	2549	2544
P2NE	1.30	2600	2557	2553
P2NE	1.35	2600	2564	2561
P2NE	1.40	2600	2570	2567
P2NE	1.45	2600	2575	2572
P2NE	1.50	2600	2579	2577

Location	Depth (m below TWI)	Simulated B ($\mu\text{g L}^{-1}$)		
		2015	2016	2017
P2NE	1.55	2600	2582	2580
P2NE	1.60	2600	2585	2583
P2NE	1.65	2600	2588	2586
P2NE	1.70	2600	2590	2588
P2NE	1.75	2600	2591	2590
P2NE	1.80	2600	2593	2592
P2NE	1.85	2600	2594	2593
P2NE	1.90	2600	2595	2594
P2NE	1.95	2600	2596	2595
P2NE	2.00	2600	2596	2596
P2NE	2.10	2600	2598	2597
P2NE	2.20	2600	2599	2599
P2NE	2.30	2600	2600	2600
P2NE	2.40	2600	2600	2600
P2NE	2.50	2600	2600	2600
P2NE	2.60	2600	2600	2600
P2NE	2.70	2600	2600	2600
P2NE	2.80	2600	2600	2600
P2NE	2.90	2600	2600	2600
P2NE	3.00	2600	2600	2600
P2NE	3.10	2600	2600	2600
P2NE	3.20	2600	2600	2600
P2NE	3.30	2600	2600	2600
P2NE	3.40	2600	2600	2600
P2NE	3.50	2600	2600	2600
P2NE	3.60	2600	2600	2600
P2NE	3.70	2600	2600	2600
P2NE	3.80	2600	2600	2600
P2NE	3.90	2600	2600	2600
P2NE	4.00	2600	2600	2600
P2NE	4.10	2600	2600	2600
P2NE	4.20	2600	2600	2600
P2NE	4.30	2600	2600	2600
P2NE	4.40	2600	2600	2600
P2NE	4.50	2600	2600	2600
P2NE	4.60	2600	2600	2600
P2NE	4.70	2600	2600	2600
P2NE	4.80	2600	2600	2600
P2NE	4.90	2600	2600	2600
P2NE	5.00	2600	2600	2600

Table B–5: Best fit simulated B concentrations for location P3SW in 2015, 2016 and 2017.

Location	Depth (m below TWI)	Simulated B ($\mu\text{g L}^{-1}$)		
		2015	2016	2017
P3SW	0.00	1500	1500	1500
P3SW	0.02	1597	1594	1593
P3SW	0.04	1682	1677	1675
P3SW	0.06	1758	1751	1748
P3SW	0.08	1825	1816	1813
P3SW	0.10	1884	1874	1870
P3SW	0.12	1937	1925	1921
P3SW	0.15	2023	2010	2006
P3SW	0.17	2059	2045	2041
P3SW	0.19	2091	2077	2072
P3SW	0.21	2118	2104	2100
P3SW	0.23	2143	2129	2125
P3SW	0.25	2164	2150	2147
P3SW	0.30	2208	2195	2193
P3SW	0.35	2238	2228	2227
P3SW	0.40	2259	2251	2252
P3SW	0.45	2273	2267	2270
P3SW	0.50	2283	2279	2284
P3SW	0.55	2289	2288	2295
P3SW	0.60	2294	2294	2304
P3SW	0.65	2297	2300	2312
P3SW	0.70	2299	2304	2319
P3SW	0.75	2300	2308	2325
P3SW	0.80	2302	2312	2331
P3SW	0.85	2303	2316	2337
P3SW	0.90	2304	2320	2344
P3SW	0.95	2306	2324	2351
P3SW	1.00	2308	2330	2358
P3SW	1.05	2311	2336	2366
P3SW	1.10	2315	2342	2373
P3SW	1.15	2319	2349	2382
P3SW	1.20	2324	2357	2390
P3SW	1.25	2330	2365	2398
P3SW	1.30	2337	2374	2407
P3SW	1.35	2345	2383	2415
P3SW	1.40	2354	2393	2423
P3SW	1.45	2363	2402	2431
P3SW	1.50	2374	2412	2439
P3SW	1.55	2385	2421	2446

Location	Depth (m below TWI)	Simulated B ($\mu\text{g L}^{-1}$)		
		2015	2016	2017
P3SW	1.60	2396	2430	2453
P3SW	1.65	2408	2439	2459
P3SW	1.70	2419	2447	2465
P3SW	1.75	2430	2455	2470
P3SW	1.80	2441	2462	2475
P3SW	1.85	2451	2468	2479
P3SW	1.90	2459	2474	2483
P3SW	1.95	2467	2479	2486
P3SW	2.00	2474	2483	2488
P3SW	2.10	2485	2490	2493
P3SW	2.20	2492	2494	2496
P3SW	2.30	2496	2497	2498
P3SW	2.40	2498	2498	2499
P3SW	2.50	2499	2499	2499
P3SW	2.60	2500	2500	2500
P3SW	2.70	2500	2500	2500
P3SW	2.80	2500	2500	2500
P3SW	2.90	2500	2500	2500
P3SW	3.00	2500	2500	2500
P3SW	3.10	2500	2500	2500
P3SW	3.20	2500	2500	2500
P3SW	3.30	2500	2500	2500
P3SW	3.40	2500	2500	2500
P3SW	3.50	2500	2500	2500
P3SW	3.60	2500	2500	2500
P3SW	3.70	2500	2500	2500
P3SW	3.80	2500	2500	2500
P3SW	3.90	2500	2500	2500
P3SW	4.00	2500	2500	2500
P3SW	4.10	2500	2500	2500
P3SW	4.20	2500	2500	2500
P3SW	4.30	2500	2500	2500
P3SW	4.40	2500	2500	2500
P3SW	4.50	2500	2500	2500
P3SW	4.60	2500	2500	2500
P3SW	4.70	2500	2500	2500
P3SW	4.80	2500	2500	2500
P3SW	4.90	2500	2500	2500
P3SW	5.00	2500	2500	2500

Table B-6: Best fit simulated CH_{4(aq)} concentrations for location P1C in 2015, 2016 and 2017.

Location	Depth (m below TWI)	Simulated CH _{4(aq)} (mg L ⁻¹)		
		2015	2016	2017
P1C	0.00	0.0	0.0	0.0
P1C	0.02	0.0	0.0	0.0
P1C	0.04	3.5	2.6	2.5
P1C	0.06	6.9	5.0	5.0
P1C	0.08	10.0	7.4	7.3
P1C	0.10	13.1	9.7	9.5
P1C	0.12	15.9	11.8	11.6
P1C	0.15	23.6	17.7	17.4
P1C	0.17	25.8	19.5	19.2
P1C	0.19	27.9	21.2	20.8
P1C	0.21	29.9	22.8	22.4
P1C	0.23	31.7	24.3	23.9
P1C	0.25	33.4	25.7	25.3
P1C	0.30	37.2	29.0	28.6
P1C	0.35	40.2	31.9	31.5
P1C	0.40	42.6	34.3	33.9
P1C	0.45	44.5	36.3	35.9
P1C	0.50	45.9	38.0	37.7
P1C	0.55	47.0	39.5	39.3
P1C	0.60	47.8	40.9	40.6
P1C	0.65	48.4	42.0	41.8
P1C	0.70	48.9	43.1	42.9
P1C	0.75	49.2	44.0	43.8
P1C	0.80	49.4	44.9	44.7
P1C	0.85	49.6	45.7	45.6
P1C	0.90	49.7	46.5	46.4
P1C	0.95	49.8	47.2	47.1
P1C	1.00	49.9	47.9	47.8
P1C	1.05	49.9	48.5	48.4
P1C	1.10	49.9	49.0	48.9
P1C	1.15	50.0	49.3	49.2
P1C	1.20	50.0	49.5	49.5
P1C	1.25	50.0	49.7	49.6
P1C	1.30	50.0	49.8	49.7
P1C	1.35	50.0	49.9	49.8
P1C	1.40	50.0	49.9	49.9
P1C	1.45	50.0	49.9	49.9
P1C	1.50	50.0	50.0	49.9
P1C	1.55	50.0	50.0	50.0

Location	Depth (m below TWI)	Simulated CH _{4(aq)} (mg L ⁻¹)		
		2015	2016	2017
P1C	1.60	50.0	50.0	50.0
P1C	1.65	50.0	50.0	50.0
P1C	1.70	50.0	50.0	50.0
P1C	1.75	50.0	50.0	50.0
P1C	1.80	50.0	50.0	50.0
P1C	1.85	50.0	50.0	50.0
P1C	1.90	50.0	50.0	50.0
P1C	1.95	50.0	50.0	50.0
P1C	2.00	50.0	50.0	50.0
P1C	2.10	50.0	50.0	50.0
P1C	2.20	50.0	50.0	50.0
P1C	2.30	50.0	50.0	50.0
P1C	2.40	50.0	50.0	50.0
P1C	2.50	50.0	50.0	50.0
P1C	2.60	50.0	50.0	50.0
P1C	2.70	50.0	50.0	50.0
P1C	2.80	50.0	50.0	50.0
P1C	2.90	50.0	50.0	50.0
P1C	3.00	50.0	50.0	50.0
P1C	3.10	50.0	50.0	50.0
P1C	3.20	50.0	50.0	50.0
P1C	3.30	50.0	50.0	50.0
P1C	3.40	50.0	50.0	50.0
P1C	3.50	50.0	50.0	50.0
P1C	3.60	50.0	50.0	50.0
P1C	3.70	50.0	50.0	50.0
P1C	3.80	50.0	50.0	50.0
P1C	3.90	50.0	50.0	50.0
P1C	4.00	50.0	50.0	50.0
P1C	4.10	50.0	50.0	50.0
P1C	4.20	50.0	50.0	50.0
P1C	4.30	50.0	50.0	50.0
P1C	4.40	50.0	50.0	50.0
P1C	4.50	50.0	50.0	50.0
P1C	4.60	50.0	50.0	50.0
P1C	4.70	50.0	50.0	50.0
P1C	4.80	50.0	50.0	50.0
P1C	4.90	50.0	50.0	50.0
P1C	5.00	50.0	50.0	50.0

Table B-7: Best fit simulated CH_{4(aq)} concentrations for location P2NE in 2015, 2016 and 2017.

Location	Depth (m below TWI)	Simulated CH _{4(aq)} (µg L ⁻¹)		
		2015	2016	2017
P2NE	0.00	0.0	0.0	-
P2NE	0.02	1.1	0.8	-
P2NE	0.04	2.1	1.6	-
P2NE	0.06	3.2	2.4	-
P2NE	0.08	4.2	3.2	-
P2NE	0.10	5.2	3.9	-
P2NE	0.12	6.3	4.7	-
P2NE	0.15	8.3	6.3	-
P2NE	0.17	9.3	7.1	-
P2NE	0.19	10.4	7.8	-
P2NE	0.21	11.4	8.6	-
P2NE	0.23	12.4	9.4	-
P2NE	0.25	13.3	10.1	-
P2NE	0.30	15.8	12.1	-
P2NE	0.35	18.3	14.0	-
P2NE	0.40	20.6	15.8	-
P2NE	0.45	22.8	17.6	-
P2NE	0.50	25.0	19.4	-
P2NE	0.55	27.0	21.1	-
P2NE	0.60	29.0	22.7	-
P2NE	0.65	30.9	24.3	-
P2NE	0.70	32.7	25.8	-
P2NE	0.75	34.4	27.3	-
P2NE	0.80	36.1	28.8	-
P2NE	0.85	37.7	30.2	-
P2NE	0.90	39.3	31.6	-
P2NE	0.95	40.8	32.9	-
P2NE	1.00	42.3	34.3	-
P2NE	1.05	43.7	35.5	-
P2NE	1.10	45.0	36.8	-
P2NE	1.15	46.3	38.0	-
P2NE	1.20	47.5	39.1	-
P2NE	1.25	48.6	40.2	-
P2NE	1.30	49.8	41.3	-
P2NE	1.35	50.8	42.4	-
P2NE	1.40	51.9	43.5	-
P2NE	1.45	52.9	44.5	-
P2NE	1.50	53.8	45.5	-
P2NE	1.55	54.7	46.5	-

Location	Depth (m below TWI)	Simulated CH _{4(aq)} (µg L ⁻¹)		
		2015	2016	2017
P2NE	1.60	55.5	47.5	-
P2NE	1.65	56.1	48.4	-
P2NE	1.70	56.7	49.4	-
P2NE	1.75	57.2	50.3	-
P2NE	1.80	57.7	51.2	-
P2NE	1.85	58.0	52.0	-
P2NE	1.90	58.3	52.9	-
P2NE	1.95	58.6	53.7	-
P2NE	2.00	58.8	54.5	-
P2NE	2.10	59.2	56.2	-
P2NE	2.20	59.6	58.1	-
P2NE	2.30	60.0	59.9	-
P2NE	2.40	60.0	60.0	-
P2NE	2.50	60.0	60.0	-
P2NE	2.60	60.0	60.0	-
P2NE	2.70	60.0	60.0	-
P2NE	2.80	60.0	60.0	-
P2NE	2.90	60.0	60.0	-
P2NE	3.00	60.0	60.0	-
P2NE	3.10	60.0	60.0	-
P2NE	3.20	60.0	60.0	-
P2NE	3.30	60.0	60.0	-
P2NE	3.40	60.0	60.0	-
P2NE	3.50	60.0	60.0	-
P2NE	3.60	60.0	60.0	-
P2NE	3.70	60.0	60.0	-
P2NE	3.80	60.0	60.0	-
P2NE	3.90	60.0	60.0	-
P2NE	4.00	60.0	60.0	-
P2NE	4.10	60.0	60.0	-
P2NE	4.20	60.0	60.0	-
P2NE	4.30	60.0	60.0	-
P2NE	4.40	60.0	60.0	-
P2NE	4.50	60.0	60.0	-
P2NE	4.60	60.0	60.0	-
P2NE	4.70	60.0	60.0	-
P2NE	4.80	60.0	60.0	-
P2NE	4.90	60.0	60.0	-
P2NE	5.00	60.0	60.0	-

Table B-8: Best fit simulated CH_{4(aq)} concentrations for location P3SW in 2015, 2016 and 2017.

Location	Depth (m below TWI)	Simulated CH _{4(aq)} (µg L ⁻¹)		
		2015	2016	2017
P3SW	0.00	0.0	0.0	0.0
P3SW	0.02	0.8	0.8	0.6
P3SW	0.04	1.5	1.7	1.3
P3SW	0.06	2.3	2.6	2.0
P3SW	0.08	3.0	3.4	2.7
P3SW	0.10	3.8	4.3	3.4
P3SW	0.12	4.5	5.1	4.1
P3SW	0.13	5.2	5.9	4.8
P3SW	0.15	5.9	6.8	5.6
P3SW	0.17	6.6	7.6	6.3
P3SW	0.19	7.2	8.4	7.0
P3SW	0.21	7.9	9.2	7.8
P3SW	0.23	8.5	10.0	8.5
P3SW	0.25	9.1	10.8	9.3
P3SW	0.30	10.5	12.8	11.2
P3SW	0.35	11.7	14.8	13.2
P3SW	0.40	12.9	16.7	15.1
P3SW	0.45	13.9	18.5	17.1
P3SW	0.50	14.8	20.4	19.1
P3SW	0.55	15.7	22.2	21.1
P3SW	0.60	16.5	24.0	23.2
P3SW	0.65	17.4	25.9	25.2
P3SW	0.70	18.2	27.7	27.3
P3SW	0.75	19.1	29.6	29.3
P3SW	0.80	20.0	31.5	31.4
P3SW	0.85	21.0	33.5	33.5
P3SW	0.90	22.0	35.4	35.6
P3SW	0.95	23.1	37.4	37.8
P3SW	1.00	24.3	39.4	39.9
P3SW	1.05	25.6	41.1	41.7
P3SW	1.10	27.0	42.3	42.8
P3SW	1.15	28.5	43.2	43.6
P3SW	1.20	30.0	43.8	44.1
P3SW	1.25	31.6	44.2	44.4
P3SW	1.30	33.2	44.5	44.6
P3SW	1.35	34.9	44.6	44.7
P3SW	1.40	36.7	44.8	44.8
P3SW	1.45	38.5	44.8	44.9
P3SW	1.50	40.3	44.9	44.9

Location	Depth (m below TWI)	Simulated CH _{4(aq)} (µg L ⁻¹)		
		2015	2016	2017
P3SW	1.55	41.8	44.9	44.9
P3SW	1.60	42.9	45.0	45.0
P3SW	1.65	43.6	45.0	45.0
P3SW	1.70	44.1	45.0	45.0
P3SW	1.75	44.4	45.0	45.0
P3SW	1.80	44.6	45.0	45.0
P3SW	1.85	44.8	45.0	45.0
P3SW	1.90	44.9	45.0	45.0
P3SW	1.95	44.9	45.0	45.0
P3SW	2.00	44.9	45.0	45.0
P3SW	2.10	45.0	45.0	45.0
P3SW	2.20	45.0	45.0	45.0
P3SW	2.30	45.0	45.0	45.0
P3SW	2.40	45.0	45.0	45.0
P3SW	2.50	45.0	45.0	45.0
P3SW	2.60	45.0	45.0	45.0
P3SW	2.70	45.0	45.0	45.0
P3SW	2.80	45.0	45.0	45.0
P3SW	2.90	45.0	45.0	45.0
P3SW	3.00	45.0	45.0	45.0
P3SW	3.10	45.0	45.0	45.0
P3SW	3.20	45.0	45.0	45.0
P3SW	3.30	45.0	45.0	45.0
P3SW	3.40	45.0	45.0	45.0
P3SW	3.50	45.0	45.0	45.0
P3SW	3.60	45.0	45.0	45.0
P3SW	3.70	45.0	45.0	45.0
P3SW	3.80	45.0	45.0	45.0
P3SW	3.90	45.0	45.0	45.0
P3SW	4.00	45.0	45.0	45.0
P3SW	4.10	45.0	45.0	45.0
P3SW	4.20	45.0	45.0	45.0
P3SW	4.30	45.0	45.0	45.0
P3SW	4.40	45.0	45.0	45.0
P3SW	4.50	45.0	45.0	45.0
P3SW	4.60	45.0	45.0	45.0
P3SW	4.70	45.0	45.0	45.0
P3SW	4.80	45.0	45.0	45.0
P3SW	4.90	45.0	45.0	45.0
P3SW	5.00	45.0	45.0	45.0

Best Fit Model Reports:

P1C Cl⁻ Transient Seepage

Report generated using GeoStudio 2018 R2. Copyright © 1991-2018 GEOSLOPE International Ltd.

Project Settings:

Unit System: International System of Units (SI)

Analysis Settings:

- Transient Seepage
- Description: Establish upward pore water movement
- Kind: SEEP/W
- Parent: Steady-State Seepage
- Method: Transient

Physics

- Water Transfer
- Free convection: thermal effects: No
- Free convection: solute effects: No
- Vapor transfer: isothermal: No
- Vapor transfer: thermal: No

Water Settings

- Initial PWP Conditions from: Parent Analysis
- Maximum Number of Iterations: 500
- Maximum Difference: 0.005
- Significant Digits: 2
- Max # of Reviews: 10

Under-Relaxation Criteria

- Initial Rate: 1
- Minimum Rate: 0.1
- Rate Reduction Factor: 0.65

- Reduction Frequency (iterations): 10
- Unit Weight of Water: 9.807 kN/m³
- Bulk Modulus of Pore-Fluid: 2,083,333.3 kPa

Settings

- Dimension: 1D
- Exclude cumulative values: No

Time

- Starting Time: 1 d
- Duration: 2,000 d
- # of Steps: 100
- Step Generation Method: Linear
- Time Increment: 20 d
- Save Steps Every: 1
- Fixed Elapsed Times: 810; 1,180; 1,550;

Materials:

FFT 1 Hydraulic Model: Saturated Only

- Sat Kx: 1 m/d
- Ky'/Kx' Ratio: 1
- Rotation: 0 °
- Volumetric Water Content: 0.86
- Compressibility: 0 /kPa

Water Hydraulic Model: Saturated Only

- Sat Kx: 1 m/d
- Ky'/Kx' Ratio: 1
- Rotation: 0 °
- Volumetric Water Content: 1
- Compressibility: 0 /kPa

FFT 2 Hydraulic Model: Saturated Only

- Sat Kx: 1 m/d

- K_y'/K_x' Ratio: 1
- Rotation: 0 °
- Volumetric Water Content: 0.85
- Compressibility: 0 /kPa

FFT 3 Hydraulic Model: Saturated Only

- Sat K_x : 1 m/d
- K_y'/K_x' Ratio: 1
- Rotation: 0 °
- Volumetric Water Content: 0.84
- Compressibility: 0 /kPa

FFT 4 Hydraulic Model: Saturated Only

- Sat K_x : 1 m/d
- K_y'/K_x' Ratio: 1
- Rotation: 0 °
- Volumetric Water Content: 0.83
- Compressibility: 0 /kPa

FFT 5 Hydraulic Model: Saturated Only

- Sat K_x : 1 m/d
- K_y'/K_x' Ratio: 1
- Rotation: 0 °
- Volumetric Water Content: 0.82
- Compressibility: 0 /kPa

Boundary Conditions:

Head at Top:

- Category: Hydraulic
- Kind: Water Pressure Head 10 m

Flow in bottom

- Category: Hydraulic

- Kind: Water Flux
- Seep Water Unit Flux Function: PIC
- Review: No

Hydraulic Boundary Functions: PIC

- Model: Spline Data Point Function
- Function: Water Flux vs. Time
- Curve Fit to Data: 100 %
- Segment Curvature: 100 %
- Y-Intercept: 0.003378243 m³/d/m²
- Data Points: Time (d), Water Flux (m³/d/m²)

PIC Cl CTRAN/W Analysis

Report generated using GeoStudio 2018 R2. Copyright © 1991-2018 GEOSLOPE International Ltd.

Project Settings:

Unit System: International System of Units (SI)

Analysis Settings

- CTRAN/W Analysis
- Description: Establish concentrations in tailings (and water)
- Kind: CTRAN/W
- Parent: Transient Seepage
- Method: Transient

Physics:

Solute Transfer

- Advection-dispersion with water transfer: Yes

Water Settings

- Results from: Parent Analysis

Solute Settings

- Initial Concentrations from: (none)
- Maximum Number of Iterations: 25
- Maximum Difference: 1e-05
- Significant Digits: 2

Settings

- Dimension: 1D
- Exclude cumulative values: No

Time

- Starting Time: 0 d
- Duration: 2,000 d
- # of Steps: 100
- Step Generation Method: Linear
- Time Increment: 20 d
- Save Steps Every: 1
- Fixed Elapsed Times: 810; 1,180; 1,550;

Materials

FFT 1 Solute:

- Diffusion Function: P1 Add In Function
- Adsorption Function: Adsorption vs concentration
- Longitudinal Dispersivity: 0.004 m
- Transverse Dispersivity: 0.003 m
- Decay Half-Life: 0 d
- Dry Density: 0 g/m³
- Activation Concentration: 600 g/m³

Water Solute

- Diffusion Function: Diffusion in water
- Adsorption Function: Adsorption vs concentration

- Longitudinal Dispersivity: 1 m
- Transverse Dispersivity: 1 m
- Decay Half-Life: 0 d
- Dry Density: 0 g/m³
- Activation Concentration: 380 g/m³

FFT 2 Solute

- Diffusion Function: P1 Add In Function
- Adsorption Function: Adsorption vs concentration
- Longitudinal Dispersivity: 0.004 m
- Transverse Dispersivity: 0.003 m
- Decay Half-Life: 0 d
- Dry Density: 0 g/m³
- Activation Concentration: 600 g/m³
- FFT 3 Solute: Diffusion Function: P1 Add In Function
- Adsorption Function: Adsorption vs concentration
- Longitudinal Dispersivity: 0.004 m
- Transverse Dispersivity: 0.003 m
- Decay Half-Life: 0 d
- Dry Density: 0 g/m³
- Activation Concentration: 600 g/m³

FFT 4 Solute

- Diffusion Function: P1 Add In Function
- Adsorption Function: Adsorption vs concentration
- Longitudinal Dispersivity: 0.004 m
- Transverse Dispersivity: 0.003 m
- Decay Half-Life: 0 d
- Dry Density: 0 g/m³
- Activation Concentration: 550 g/m³

FFT 5 Solute

- Diffusion Function: P1 Add In Function
- Adsorption Function: Adsorption vs concentration
- Longitudinal Dispersivity: 0.004 m
- Transverse Dispersivity: 0.003 m
- Decay Half-Life: 0 d
- Dry Density: 0 g/m³
- Activation Concentration: 550 g/m³

Boundary Conditions:

Bottom Cl

- Category: Contaminant
- Kind: Solute Concentration 550 g/m³

Changing Cl

- Category: Contaminant
- Kind: Solute Concentration

Contaminate Concentration Vs Time Function: Cl Changing geochem added in DF

Contaminant Adsorption Functions

Adsorption vs concentration

- Model: Spline Data Point Function
- Function: Adsorption vs. Concentration
- Curve Fit to Data: 100 %
- Segment Curvature: 100 %
- Y-Intercept: 0 g/g
- Data Points: Concentration (g/m³), Adsorption (g/g)

Contaminant Boundary Functions:

Cl Changing Cl-

- Model: Spline Data Point Function
- Function: Concentration vs. Time

- Curve Fit to Data: 32 %
- Segment Curvature: 40 %
- Y-Intercept: 546.95376 g/m³
- Data Points: Time (d), Concentration (g/m³)

Contaminant Diffusion Functions:

P1 Add In Function

- Model: Add-In Function
- Function: TestInterpolateList
- Assembly: Interpolate Diffusion Coefficient
- Function: TestInterpolateList

Diffusion in water

- Model: Spline Data Point Function
- Function: Diffusion Coefficient vs. Volumetric Water Content
- Curve Fit to Data: 100 %
- Segment Curvature: 100 %
- Y-Intercept: 0.000125 m²/d
- Data Points: Volumetric Water Content, Diffusion Coefficient (m²/d)

P2NE Cl⁻ Transient Seepage

Report generated using GeoStudio 2018 R2. Copyright © 1991-2018 GEOSLOPE International Ltd.

Project Settings

- Unit System: International System of Units (SI)

Analysis Settings

Transient Seepage

- Description: Establish upward pore water movement
- Kind: SEEP/W
- Parent: Steady-State Seepage
- Method: Transient

Physics

Water Transfer

- Free convection: thermal effects: No
- Free convection: solute effects: No
- Vapor transfer: isothermal: No
- Vapor transfer: thermal: No

Water Settings

- Initial PWP Conditions from: Parent Analysis
- Maximum Number of Iterations: 500
- Maximum Difference: 0.005
- Significant Digits: 2
- Max # of Reviews: 10

Under-Relaxation Criteria

- Initial Rate: 1
- Minimum Rate: 0.1
- Rate Reduction Factor: 0.65
- Reduction Frequency (iterations): 10
- Unit Weight of Water: 9.807 kN/m³
- Bulk Modulus of Pore-Fluid: 2,083,333.3 kPa

Settings

- Dimension: 1D
- Exclude cumulative values: No

Time

- Starting Time: 1 d
- Duration: 2,400 d
- # of Steps: 80
- Step Generation Method: Linear
- Time Increment: 30 d
- Save Steps Every: 1
- Fixed Elapsed Times: 810; 1,180; 1,550;

Materials

FFT 1

- Hydraulic Model: Saturated Only
- Sat Kx: 1 m/d
- K_y'/K_x' Ratio: 1
- Rotation: 0 °
- Volumetric Water Content: 0.95
- Compressibility: 0 /kPa

Water

- Hydraulic Model: Saturated Only
- Sat Kx: 1 m/d
- K_y'/K_x' Ratio: 1
- Rotation: 0 °
- Volumetric Water Content: 1
- Compressibility: 0 /kPa

FFT 2

- Hydraulic Model: Saturated Only
- Sat Kx: 1 m/d
- K_y'/K_x' Ratio: 1
- Rotation: 0 °
- Volumetric Water Content: 0.95
- Compressibility: 0 /kPa

FFT 3

- Hydraulic Model: Saturated Only
- Sat Kx: 1 m/d
- K_y'/K_x' Ratio: 1
- Rotation: 0 °
- Volumetric Water Content: 0.84
- Compressibility: 0 /kPa

FFT 4

- Hydraulic Model: Saturated Only

- Sat Kx: 1 m/d
- Ky'/Kx' Ratio: 1
- Rotation: 0 °
- Volumetric Water Content: 0.83
- Compressibility: 0 /kPa

FFT 5

- Hydraulic Model: Saturated Only
- Sat Kx: 1 m/d
- Ky'/Kx' Ratio: 1
- Rotation: 0 °
- Volumetric Water Content: 0.82
- Compressibility: 0 /kPa

Boundary Conditions

Head at Top

- Category: Hydraulic
- Kind: Water Pressure Head 10 m

Flow in bottom

- Category: Hydraulic
- Kind: Water Flux
- Seep Water Unit Flux Function: P2NE
- Review: No

Hydraulic Boundary Functions

P2NE

- Model: Spline Data Point Function
- Function: Water Flux vs. Time
- Curve Fit to Data: 100 %
- Segment Curvature: 100 %
- Y-Intercept: 0.00577 m³/d/m²
- Data Points: Time (d), Water Flux (m³/d/m²)

P2NE Cl⁻ CTRAN/W Analysis

Report generated using GeoStudio 2018 R2. Copyright © 1991-2018 GEOSLOPE International Ltd.

Project Settings:

- Unit System: International System of Units (SI)

Analysis Settings:

- CTRAN/W Analysis
- Description: Establish concentrations in tailings (and water)
- Kind: CTRAN/W
- Parent: Transient Seepage
- Method: Transient

Physics:

- Solute Transfer
- Advection-dispersion with water transfer: Yes
- Water Settings
- Results from: Parent Analysis

Solute Settings:

- Initial Concentrations from: (none)
- Maximum Number of Iterations: 25
- Maximum Difference: 1e-05
- Significant Digits: 2

Settings:

- Dimension: 1D
- Exclude cumulative values: No

Time:

- Starting Time: 0 d
- Duration: 2,400 d
- # of Steps: 80
- Step Generation Method: Linear
- Time Increment: 30 d

- Save Steps Every: 1
- Fixed Elapsed Times: 810; 1,180; 1,550;

Materials:

FFT 1 Solute

- Diffusion Function: P2 Add In Function
- Adsorption Function: Adsorption vs concentration
- Longitudinal Dispersivity: 0.004 m
- Transverse Dispersivity: 0.003 m
- Decay Half-Life: 0 d
- Dry Density: 0 g/m³
- Activation Concentration: 600 g/m³

Water

- Diffusion Function: Diffusion vs water content
- Adsorption Function: Adsorption vs concentration
- Longitudinal Dispersivity: 1 m
- Transverse Dispersivity: 1 m
- Decay Half-Life: 0 d
- Dry Density: 0 g/m³
- Activation Concentration: 380 g/m³

FFT 2 Solute

- Diffusion Function: P2 Add In Function
- Adsorption Function: Adsorption vs concentration
- Longitudinal Dispersivity: 0.004 m
- Transverse Dispersivity: 0.003 m
- Decay Half-Life: 0 d
- Dry Density: 0 g/m³
- Activation Concentration: 600 g/m³

FFT 3 Solute

- Diffusion Function: P2 Add In Function
- Adsorption Function: Adsorption vs concentration

- Longitudinal Dispersivity: 0.004 m
- Transverse Dispersivity: 0.003 m
- Decay Half-Life: 0 d
- Dry Density: 0 g/m³
- Activation Concentration: 600 g/m³

FFT 4 Solute

- Diffusion Function: P2 Add In Function
- Adsorption Function: Adsorption vs concentration
- Longitudinal Dispersivity: 0.004 m
- Transverse Dispersivity: 0.003 m
- Decay Half-Life: 0 d
- Dry Density: 0 g/m³
- Activation Concentration: 600 g/m³

FFT 5 Solute

- Diffusion Function: P2 Add In Function
- Adsorption Function: Adsorption vs concentration
- Longitudinal Dispersivity: 0.004 m
- Transverse Dispersivity: 0.003 m
- Decay Half-Life: 0 d
- Dry Density: 0 g/m³
- Activation Concentration: 600 g/m³

Boundary Conditions:

Bottom Cl

- Category: Contaminant
- Kind: Solute Concentration 600 g/m³
- Changing Cl
- Category: Contaminant
- Kind: Solute Concentration
- Contaminate Concentration Vs Time Function: Cl Changing geochem added in DF

Contaminant Adsorption Functions:

Adsorption vs concentration

- Model: Spline Data Point Function
- Function: Adsorption vs. Concentration
- Curve Fit to Data: 100 %
- Segment Curvature: 100 %
- Y-Intercept: 0 g/g
- Data Points: Concentration (g/m^3), Adsorption (g/g)
- Data Point: (0, 0)
- Data Point: (1,000, 0)

Contaminant Boundary Functions:

Cl⁻ Changing Water Cap

- Model: Spline Data Point Function
- Function: Concentration vs. Time
- Curve Fit to Data: 32 %
- Segment Curvature: 40 %
- Y-Intercept: 546.95376 g/m^3
- Data Points: Time (d), Concentration (g/m^3)

Contaminant Diffusion Functions:

Diffusion vs water content

- Model: Spline Data Point Function
- Function: Diffusion Coefficient vs. Volumetric Water Content
- Curve Fit to Data: 95 %
- Segment Curvature: 22 %
- Y-Intercept: 6.1999999e-05 m^2/d
- Data Points: Volumetric Water Content, Diffusion Coefficient (m^2/d)

P2 Add In Function

- Model: Add-In Function
- Function: TestInterpolateList
- Assembly: Interpolate Diffusion Coefficient
- Function: TestInterpolateList

- Field: csvFileLocation: C:\Users\djf160\Documents\MSc\Transport Models\P2 Add In\P2Function.cs

P3SW Cl⁻ Transient Seepage

Report generated using GeoStudio 2018 R2. Copyright © 1991-2018 GEOSLOPE International Ltd.

Project Settings

- Unit System: International System of Units (SI)

Analysis Settings:

- Transient Seepage
- Description: Establish upward pore water movement
- Kind: SEEP/W
- Parent: Steady-State Seepage
- Method: Transient

Physics

Water Transfer

- Free convection: thermal effects: No
- Free convection: solute effects: No
- Vapor transfer: isothermal: No
- Vapor transfer: thermal: No

Water Settings

- Initial PWP Conditions from: Parent Analysis
- Maximum Number of Iterations: 500
- Maximum Difference: 0.005
- Significant Digits: 2
- Max # of Reviews: 10

Under-Relaxation Criteria

- Initial Rate: 1
- Minimum Rate: 0.1
- Rate Reduction Factor: 0.65
- Reduction Frequency (iterations): 10

- Unit Weight of Water: 9.807 kN/m³
- Bulk Modulus of Pore-Fluid: 2,083,333.3 kPa

Settings

- Dimension: 1D
- Exclude cumulative values: No

Time

- Starting Time: 1 d
- Duration: 2,000 d
- # of Steps: 100
- Step Generation Method: Linear
- Time Increment: 20 d
- Save Steps Every: 1

Materials

FFT 1

- Hydraulic
- Model: Saturated Only
- Sat Kx: 1 m/d
- Ky'/Kx' Ratio: 1
- Rotation: 0 °
- Volumetric Water Content: 0.86
- Compressibility: 0 /kPa

Water

- Hydraulic
- Model: Saturated Only
- Sat Kx: 1 m/d
- Ky'/Kx' Ratio: 1
- Rotation: 0 °
- Volumetric Water Content: 1
- Compressibility: 0 /kPa

FFT 2

- Hydraulic
- Model: Saturated Only
- Sat Kx: 1 m/d
- Ky'/Kx' Ratio: 1
- Rotation: 0 °
- Volumetric Water Content: 0.85
- Compressibility: 0 /kPa

FFT 3

- Hydraulic
- Model: Saturated Only
- Sat Kx: 1 m/d
- Ky'/Kx' Ratio: 1
- Rotation: 0 °
- Volumetric Water Content: 0.84
- Compressibility: 0 /kPa

FFT 4

- Hydraulic
- Model: Saturated Only
- Sat Kx: 1 m/d
- Ky'/Kx' Ratio: 1
- Rotation: 0 °
- Volumetric Water Content: 0.83
- Compressibility: 0 /kPa

FFT 5

- Hydraulic
- Model: Saturated Only
- Sat Kx: 1 m/d
- Ky'/Kx' Ratio: 1
- Rotation: 0 °
- Volumetric Water Content: 0.82

- Compressibility: 0 /kPa

Boundary Conditions

Head at Top

- Category: Hydraulic
- Kind: Water Pressure Head 10 m
- P3 Constant flow
- Category: Hydraulic
- Kind: Water Flux 0.00055 m/d
- Review: No

P3SW Cl⁻ CTRAN/WAnalysis

Report generated using GeoStudio 2018 R2. Copyright © 1991-2018 GEOSLOPE International Ltd.

Project Settings

- Unit System: International System of Units (SI)

Analysis Settings

- CTRAN/WAnalysis
- Description: Establish concentrations in tailings (and water)
- Kind: CTRAN/W
- Parent: Transient Seepage
- Method: Transient

Physics

Solute Transfer

- Advection-dispersion with water transfer: Yes
- Water Settings
- Results from: Parent Analysis
- Solute Settings
- Initial Concentrations from: (none)
- Maximum Number of Iterations: 25
- Maximum Difference: 1e-05
- Significant Digits: 2

Settings:

- Dimension: 1D
- Exclude cumulative values: No

Time

- Starting Time: 0 d
- Duration: 2,000 d
- # of Steps: 100
- Step Generation Method: Linear
- Time Increment: 20 d
- Save Steps Every: 1
- Fixed Elapsed Times: 810; 1,180; 1,550;

Materials

FFT 1 Solute

- Diffusion Function: Add-In Diff Coefficient
- Adsorption Function: Adsorption vs concentration
- Longitudinal Dispersivity: 0.004 m
- Transverse Dispersivity: 0.003 m
- Decay Half-Life: 0 d
- Dry Density: 0 g/m³
- Activation Concentration: 650 g/m³

Water Solute

- Diffusion Function: Diffusion in water
- Adsorption Function: Adsorption vs concentration
- Longitudinal Dispersivity: 1 m
- Transverse Dispersivity: 1 m
- Decay Half-Life: 0 d
- Dry Density: 0 g/m³
- Activation Concentration: 380 g/m³

FFT 2 Solute

- Diffusion Function: Add-In Diff Coefficient

- Adsorption Function: Adsorption vs concentration
- Longitudinal Dispersivity: 0.004 m
- Transverse Dispersivity: 0.003 m
- Decay Half-Life: 0 d
- Dry Density: 0 g/m³
- Activation Concentration: 650 g/m³

FFT 3 Solute

- Diffusion Function: Add-In Diff Coefficient
- Adsorption Function: Adsorption vs concentration
- Longitudinal Dispersivity: 0.004 m
- Transverse Dispersivity: 0.003 m
- Decay Half-Life: 0 d
- Dry Density: 0 g/m³
- Activation Concentration: 600 g/m³

FFT 4 Solute

- Diffusion Function: Add-In Diff Coefficient
- Adsorption Function: Adsorption vs concentration
- Longitudinal Dispersivity: 0.004 m
- Transverse Dispersivity: 0.003 m
- Decay Half-Life: 0 d
- Dry Density: 0 g/m³
- Activation Concentration: 600 g/m³

FFT 5 Solute

- Diffusion Function: Add-In Diff Coefficient
- Adsorption Function: Adsorption vs concentration
- Longitudinal Dispersivity: 0.004 m
- Transverse Dispersivity: 0.003 m
- Decay Half-Life: 0 d
- Dry Density: 0 g/m³
- Activation Concentration: 600 g/m³

Boundary Conditions

Bottom Cl

- Category: Contaminant
- Kind: Solute Concentration 600 g/m³

Changing Cl

- Category: Contaminant
- Kind: Solute Concentration

Contaminate Concentration Vs Time Function: Cl Changing geochem water cover

- Contaminant Adsorption Functions
- Adsorption vs concentration
- Model: Spline Data Point Function
- Function: Adsorption vs. Concentration
- Curve Fit to Data: 100 %
- Segment Curvature: 100 %
- Y-Intercept: 0 g/g
- Data Points: Concentration (g/m³), Adsorption (g/g)

Contaminant Boundary Functions

Cl Changing geochem

- Model: Spline Data Point Function
- Function: Concentration vs. Time
- Curve Fit to Data: 32 %
- Segment Curvature: 40 %
- Y-Intercept: 546.95376 g/m³
- Data Points: Time (d), Concentration (g/m³)

Contaminant Diffusion Functions

Diffusion in water

- Model: Spline Data Point Function
- Function: Diffusion Coefficient vs. Volumetric Water Content
- Curve Fit to Data: 100 %
- Segment Curvature: 100 %

- Y-Intercept: 0.000125 m²/d
- Data Points: Volumetric Water Content, Diffusion Coefficient (m²/d)
- Data Point: (0.1, 0.000125)
- Data Point: (2, 0.000125)

Add-In Diff Coefficient

- Model: Add-In Function
- Function: TestInterpolateList
- Assembly: Interpolate Diffusion Coefficient
- Function: TestInterpolateList
- Field csvFileLocation: C:\Users\djf160\Documents\MSc\Transport Models\P1 Add In\P1Function.csv

P1C Boron Transient Seepage

Report generated using GeoStudio 2018 R2. Copyright © 1991-2018 GEOSLOPE International Ltd.

Project Settings

- Unit System: International System of Units (SI)

Analysis Settings

- Transient Seepage
- Description: Establish upward pore water movement
- Kind: SEEP/W
- Parent: Steady-State Seepage
- Method: Transient

Physics

Water Transfer

- Free convection: thermal effects: No
- Free convection: solute effects: No
- Vapor transfer: isothermal: No
- Vapor transfer: thermal: No

Water Settings

- Initial PWP Conditions from: Parent Analysis
- Maximum Number of Iterations: 500
- Maximum Difference: 0.005
- Significant Digits: 2
- Max # of Reviews: 10

Under-Relaxation Criteria

- Initial Rate: 1
- Minimum Rate: 0.1
- Rate Reduction Factor: 0.65
- Reduction Frequency (iterations): 10
- Unit Weight of Water: 9.807 kN/m³
- Bulk Modulus of Pore-Fluid: 2,083,333.3 kPa

Settings

- Dimension: 1D
- Exclude cumulative values: No

Time

- Starting Time: 1 d
- Duration: 2,000 d
- # of Steps: 200
- Step Generation Method: Linear
- Time Increment: 10 d
- Save Steps Every: 1

Materials

FFT 1

- Hydraulic
- Model: Saturated Only
- Sat Kx: 1 m/d
- Ky'/Kx' Ratio: 1
- Rotation: 0 °

- Volumetric Water Content: 0.86
- Compressibility: 0 /kPa

Water

- Hydraulic
- Model: Saturated Only
- Sat Kx: 1 m/d
- K_y'/K_x' Ratio: 1
- Rotation: 0 °
- Volumetric Water Content: 1
- Compressibility: 0 /kPa

FFT 2

- Hydraulic
- Model: Saturated Only
- Sat Kx: 1 m/d
- K_y'/K_x' Ratio: 1
- Rotation: 0 °
- Volumetric Water Content: 0.85
- Compressibility: 0 /kPa

FFT 3

- Hydraulic
- Model: Saturated Only
- Sat Kx: 1 m/d
- K_y'/K_x' Ratio: 1
- Rotation: 0 °
- Volumetric Water Content: 0.84
- Compressibility: 0 /kPa

FFT 4

- Hydraulic
- Model: Saturated Only
- Sat Kx: 1 m/d

- Ky'/Kx' Ratio: 1
- Rotation: 0 °
- Volumetric Water Content: 0.83
- Compressibility: 0 /kPa

FFT 5

- Hydraulic
- Model: Saturated Only
- Sat Kx: 1 m/d
- Ky'/Kx' Ratio: 1
- Rotation: 0 °
- Volumetric Water Content: 0.82
- Compressibility: 0 /kPa

Boundary Conditions

Head at Top

- Category: Hydraulic
- Kind: Water Pressure Head 10 m
- Flow in bottom
- Category: Hydraulic
- Kind: Water Flux
- Seep Water Unit Flux Function: P1C
- Review: No

Hydraulic Boundary Functions

- P1C
- Model: Spline Data Point Function
- Function: Water Flux vs. Time
- Curve Fit to Data: 100 %
- Segment Curvature: 100 %
- Y-Intercept: 0.0036 m³/d/m²
- Data Points: Time (d), Water Flux (m³/d/m²)

CTRW/W Analysis

Report generated using GeoStudio 2018 R2. Copyright © 1991-2018 GEOSLOPE International Ltd.

Project Settings

- Unit System: International System of Units (SI)

Analysis Settings

- CTRAN/W Analysis
- Kind: CTRAN/W
- Parent: Transient Seepage
- Method: Transient

Physics

Solute Transfer

- Advection-dispersion with water transfer: Yes
- Water Settings
- Results from: Parent Analysis
- Solute Settings
- Initial Concentrations from: (none)
- Maximum Number of Iterations: 25
- Maximum Difference: 1e-05
- Significant Digits: 2

Settings

- Dimension: 1D
- Exclude cumulative values: No

Time

- Starting Time: 0 d
- Duration: 2,000 d
- # of Steps: 100
- Step Generation Method: Linear
- Time Increment: 20 d
- Save Steps Every: 5
- Fixed Elapsed Times: 810; 1,180; 1,550;

Materials

FFT 1 Solute

- Diffusion Function: P1 Add In Function
- Adsorption Function: Adsorption vs concentration
- Longitudinal Dispersivity: 0.004 m
- Transverse Dispersivity: 0.003 m
- Decay Half-Life: 0 d
- Dry Density: 0 g/m³
- Activation Concentration: 1.1 g/m³

Water Solute

- Diffusion Function: Diffusion in water
- Adsorption Function: Adsorption vs concentration
- Longitudinal Dispersivity: 1 m
- Transverse Dispersivity: 1 m
- Decay Half-Life: 0 d
- Dry Density: 0 g/m³
- Activation Concentration: 380 g/m³

FFT 2 Solute

- Diffusion Function: P1 Add In Function
- Adsorption Function: Adsorption vs concentration
- Longitudinal Dispersivity: 0.004 m
- Transverse Dispersivity: 0.003 m
- Decay Half-Life: 0 d
- Dry Density: 0 g/m³
- Activation Concentration: 1.1 g/m³

FFT 3 Solute

- Diffusion Function: P1 Add In Function
- Adsorption Function: Adsorption vs concentration
- Longitudinal Dispersivity: 0.004 m
- Transverse Dispersivity: 0.003 m

- Decay Half-Life: 0 d
- Dry Density: 0 g/m³
- Activation Concentration: 1 g/m³

FFT 4 Solute

- Diffusion Function: P1 Add In Function
- Adsorption Function: Adsorption vs concentration
- Longitudinal Dispersivity: 0.004 m
- Transverse Dispersivity: 0.003 m
- Decay Half-Life: 0 d
- Dry Density: 0 g/m³
- Activation Concentration: 1 g/m³

FFT 5 Solute

- Diffusion Function: P1 Add In Function
- Adsorption Function: Adsorption vs concentration
- Longitudinal Dispersivity: 0.004 m
- Transverse Dispersivity: 0.003 m
- Decay Half-Life: 0 d
- Dry Density: 0 g/m³
- Activation Concentration: 1 g/m³

Boundary Conditions

Bottom boron

- Category: Contaminant
- Kind: Solute Concentration 1 g/m³

Top Boron

- Category: Contaminant
- Kind: Solute Concentration 0 g/m³

Contaminant Adsorption Functions

Adsorption vs concentration

- Model: Spline Data Point Function
- Function: Adsorption vs. Concentration

- Curve Fit to Data: 100 %
- Segment Curvature: 100 %
- Y-Intercept: 0 g/g
- Data Points: Concentration (g/m³), Adsorption (g/g)

Contaminant Diffusion Functions

P1 Add In Function

- Model: Add-In Function
- Function: TestInterpolateList
- Assembly: Interpolate Diffusion Coefficient
- Function: TestInterpolateList
- FieldcsvFileLocation: C:\Users\djf160\Documents\MSc\Transport Models\P1 Add In\P1Function.csv

P1C CH₄ Normalized Transient Seepage

Report generated using GeoStudio 2018 R2. Copyright © 1991-2018 GEOSLOPE International Ltd.

Project Settings

- Unit System: International System of Units (SI)

Analysis Settings

- Transient Seepage
- Description: Establish upward pore water movement
- Kind: SEEP/W
- Parent: Steady-State Seepage
- Method: Transient

Physics

Water Transfer

- Free convection: thermal effects: No
- Free convection: solute effects: No
- Vapor transfer: isothermal: No
- Vapor transfer: thermal: No

Water Settings

- Initial PWP Conditions from: Parent Analysis
- Maximum Number of Iterations: 500
- Maximum Difference: 0.005
- Significant Digits: 2
- Max # of Reviews: 10

Under-Relaxation Criteria

- Initial Rate: 1
- Minimum Rate: 0.1
- Rate Reduction Factor: 0.65
- Reduction Frequency (iterations): 10
- Unit Weight of Water: 9.807 kN/m³
- Bulk Modulus of Pore-Fluid: 2,083,333.3 kPa

Settings

- Dimension: 1D
- Exclude cumulative values: No

Time

- Starting Time: 1 d
- Duration: 2,500 d
- # of Steps: 100
- Step Generation Method: Linear
- Time Increment: 25 d
- Save Steps Every: 2
- Fixed Elapsed Times: 810; 1,180; 1,550; 2,280;

Materials

FFT 1

- Hydraulic
- Model: Saturated Only
- Sat Kx: 1 m/d
- Ky'/Kx' Ratio: 1
- Rotation: 0 °

- Volumetric Water Content: 0.86
- Compressibility: 0 /kPa

Water

- Hydraulic
- Model: Saturated Only
- Sat Kx: 1 m/d
- Ky'/Kx' Ratio: 1
- Rotation: 0 °
- Volumetric Water Content: 1
- Compressibility: 0 /kPa

FFT 2

- Hydraulic
- Model: Saturated Only
- Sat Kx: 1 m/d
- Ky'/Kx' Ratio: 1
- Rotation: 0 °
- Volumetric Water Content: 0.85
- Compressibility: 0 /kPa

FFT 3

- Hydraulic
- Model: Saturated Only
- Sat Kx: 1 m/d
- Ky'/Kx' Ratio: 1
- Rotation: 0 °
- Volumetric Water Content: 0.84
- Compressibility: 0 /kPa

FFT 4

- Hydraulic
- Model: Saturated Only
- Sat Kx: 1 m/d

- Ky'/Kx' Ratio: 1
- Rotation: 0 °
- Volumetric Water Content: 0.83
- Compressibility: 0 /kPa

FFT 5

- Hydraulic
- Model: Saturated Only
- Sat Kx: 1 m/d
- Ky'/Kx' Ratio: 1
- Rotation: 0 °
- Volumetric Water Content: 0.82
- Compressibility: 0 /kPa

Boundary Conditions

Head at Top

- Category: Hydraulic
- Kind: Water Pressure Head 10 m

Flow in bottom

- Category: Hydraulic
- Kind: Water Flux
- Seep Water Unit Flux Function: P1C
- Review: No

Hydraulic Boundary Functions

P1C

- Model: Spline Data Point Function
- Function: Water Flux vs. Time
- Curve Fit to Data: 100 %
- Segment Curvature: 100 %
- Y-Intercept: 0.003378243 m³/d/m²
- Data Points: Time (d), Water Flux (m³/d/m²)

P1C CH₄ Normalized CTRAN/W Analysis

Report generated using GeoStudio 2018 R2. Copyright © 1991-2018 GEOSLOPE International Ltd.

Project Settings

- Unit System: International System of Units (SI)

Analysis Settings

- CTRAN/W Analysis
- Description: Establish concentrations in tailings (and water)
- Kind: CTRAN/W
- Parent: Transient Seepage
- Method: Transient

Physics

Solute Transfer

- Advection-dispersion with water transfer: Yes

Water Settings

- Results from: Parent Analysis

Solute Settings

- Initial Concentrations from: (none)
- Maximum Number of Iterations: 25
- Maximum Difference: 1e-05
- Significant Digits: 2

Settings

- Dimension: 1D
- Exclude cumulative values: No

Time

- Starting Time: 0 d
- Duration: 2,500 d
- # of Steps: 100
- Step Generation Method: Linear
- Time Increment: 25 d

- Save Steps Every: 2
- Fixed Elapsed Times: 810; 1,180; 1,550; 2,280;

Materials

FFT 1 Solute

- Diffusion Function: P1 Add In Function
- Adsorption Function: Adsorption vs concentration
- Longitudinal Dispersivity: 0.004 m
- Transverse Dispersivity: 0.003 m
- Decay Half-Life: 0 d
- Dry Density: 0 g/m³
- Activation Concentration: 1 g/m³

Water Solute

- Diffusion Function: Diffusion in water
- Adsorption Function: Adsorption vs concentration
- Longitudinal Dispersivity: 1 m
- Transverse Dispersivity: 1 m
- Decay Half-Life: 0 d
- Dry Density: 0 g/m³
- Activation Concentration: 0 g/m³

FFT 2 Solute

- Diffusion Function: P1 Add In Function
- Adsorption Function: Adsorption vs concentration
- Longitudinal Dispersivity: 0.004 m
- Transverse Dispersivity: 0.003 m
- Decay Half-Life: 0 d
- Dry Density: 0 g/m³
- Activation Concentration: 1 g/m³

FFT 3 Solute

- Diffusion Function: P1 Add In Function
- Adsorption Function: Adsorption vs concentration

- Longitudinal Dispersivity: 0.004 m
- Transverse Dispersivity: 0.003 m
- Decay Half-Life: 0 d
- Dry Density: 0 g/m³
- Activation Concentration: 1 g/m³

FFT 4 Solute

- Diffusion Function: P1 Add In Function
- Adsorption Function: Adsorption vs concentration
- Longitudinal Dispersivity: 0.004 m
- Transverse Dispersivity: 0.003 m
- Decay Half-Life: 0 d
- Dry Density: 0 g/m³
- Activation Concentration: 1 g/m³

FFT 5 Solute

- Diffusion Function: P1 Add In Function
- Adsorption Function: Adsorption vs concentration
- Longitudinal Dispersivity: 0.004 m
- Transverse Dispersivity: 0.003 m
- Decay Half-Life: 0 d
- Dry Density: 0 g/m³
- Activation Concentration: 1 g/m³

Boundary Conditions

CH₄ production

- Category: Contaminant
- Kind: Solute Concentration 1 g/m³

Top C

- Category: Contaminant
- Kind: Solute Concentration 0 g/m³

Coupled Anaerobic CH₄ Oxidation

- Category: Contaminant

- Kind: Solute Mass Flux -0.0005 g/d/m²

Contaminant Adsorption Functions

- Adsorption vs concentration
- Model: Spline Data Point Function
- Function: Adsorption vs. Concentration
- Curve Fit to Data: 100 %
- Segment Curvature: 100 %
- Y-Intercept: 0 g/g
- Data Points: Concentration (g/m³), Adsorption (g/g)

Contaminant Diffusion Functions

P1 Add In Function

- Model: Add-In Function
- Function: TestInterpolateList
- Assembly: Interpolate Diffusion Coefficient
- Function: TestInterpolateList
- FieldcsvFileLocation: C:\Users\djf160\Documents\MSc\Transport Models\P1 Add In\P1Function.csv

P2NE CH₄ Normalized Transient Seepage

Report generated using GeoStudio 2018 R2. Copyright © 1991-2018 GEOSLOPE International Ltd.

Project Settings

- Unit System: International System of Units (SI)

Analysis Settings

- Transient Seepage
- Description: Establish upward pore water movement
- Kind: SEEP/W
- Parent: Steady-State Seepage
- Method: Transient

Physics

Water Transfer

- Free convection: thermal effects: No
- Free convection: solute effects: No
- Vapor transfer: isothermal: No
- Vapor transfer: thermal: No

Water Settings

- Initial PWP Conditions from: Parent Analysis
- Maximum Number of Iterations: 500
- Maximum Difference: 0.005
- Significant Digits: 2
- Max # of Reviews: 10

Under-Relaxation Criteria

- Initial Rate: 1
- Minimum Rate: 0.1
- Rate Reduction Factor: 0.65
- Reduction Frequency (iterations): 10
- Unit Weight of Water: 9.807 kN/m³
- Bulk Modulus of Pore-Fluid: 2,083,333.3 kPa

Settings

- Dimension: 1D
- Exclude cumulative values: No

Time

- Starting Time: 1 d
- Duration: 2,500 d
- # of Steps: 100
- Step Generation Method: Linear
- Time Increment: 25 d
- Save Steps Every: 1
- Fixed Elapsed Times: 810; 1,180; 1,550; 2,280;

Materials

FFT 1

- Hydraulic
- Model: Saturated Only
- Sat Kx: 1 m/d
- K_y'/K_x' Ratio: 1
- Rotation: 0 °
- Volumetric Water Content: 0.95
- Compressibility: 0 /kPa

Water

- Hydraulic
- Model: Saturated Only
- Sat Kx: 1 m/d
- K_y'/K_x' Ratio: 1
- Rotation: 0 °
- Volumetric Water Content: 1
- Compressibility: 0 /kPa

FFT 2

- Hydraulic
- Model: Saturated Only
- Sat Kx: 1 m/d
- K_y'/K_x' Ratio: 1
- Rotation: 0 °
- Volumetric Water Content: 0.95
- Compressibility: 0 /kPa

FFT 3

- Hydraulic
- Model: Saturated Only
- Sat Kx: 1 m/d
- K_y'/K_x' Ratio: 1
- Rotation: 0 °
- Volumetric Water Content: 0.84

- Compressibility: 0 /kPa

FFT 4

- Hydraulic
- Model: Saturated Only
- Sat Kx: 1 m/d
- Ky'/Kx' Ratio: 1
- Rotation: 0 °
- Volumetric Water Content: 0.83
- Compressibility: 0 /kPa

FFT 5

- Hydraulic
- Model: Saturated Only
- Sat Kx: 1 m/d
- Ky'/Kx' Ratio: 1
- Rotation: 0 °
- Volumetric Water Content: 0.82
- Compressibility: 0 /kPa

Boundary Conditions

Head at Top

- Category: Hydraulic
- Kind: Water Pressure Head 10 m

Flow in bottom

- Category: Hydraulic
- Kind: Water Flux
- Seep Water Unit Flux Function: P2NE
- Review: No

Hydraulic Boundary Functions

- P2NE
- Model: Spline Data Point Function
- Function: Water Flux vs. Time

- Curve Fit to Data: 100 %
- Segment Curvature: 100 %
- Y-Intercept: 0.00577 m³/d/m²
- Data Points: Time (d), Water Flux (m³/d/m²)
- Mesh Properties
- View: 2D
- Element Thickness: 0.25 m

P2NE CH₄ Normalized CTRAN/W Analysis

Report generated using GeoStudio 2018 R2. Copyright © 1991-2018 GEOSLOPE International Ltd.

Project Settings

- Unit System: International System of Units (SI)

Analysis Settings

- CTRAN/W Analysis
- Description: Establish concentrations in tailings (and water)
- Kind: CTRAN/W
- Parent: Transient Seepage
- Method: Transient

Physics

- Solute Transfer
- Advection-dispersion with water transfer: Yes

Water Settings

- Results from: Parent Analysis

Solute Settings

- Initial Concentrations from: (none)
- Maximum Number of Iterations: 25
- Maximum Difference: 1e-05
- Significant Digits: 2

Settings

- Dimension: 1D

- Exclude cumulative values: No

Time

- Starting Time: 0 d
- Duration: 2,500 d
- # of Steps: 100
- Step Generation Method: Linear
- Time Increment: 25 d
- Save Steps Every: 2
- Fixed Elapsed Times: 810; 1,180; 1,550; 2,280;

Materials

FFT 1 Solute

- Diffusion Function: P2 Add In Function
- Adsorption Function: Adsorption vs concentration
- Longitudinal Dispersivity: 0.004 m
- Transverse Dispersivity: 0.003 m
- Decay Half-Life: 0 d
- Dry Density: 0 g/m³
- Activation Concentration: 1 g/m³

Water Solute

- Diffusion Function: Diffusion vs water content
- Adsorption Function: Adsorption vs concentration
- Longitudinal Dispersivity: 1 m
- Transverse Dispersivity: 1 m
- Decay Half-Life: 0 d
- Dry Density: 0 g/m³
- Activation Concentration: 0 g/m³

FFT 2 Solute

- Diffusion Function: P2 Add In Function
- Adsorption Function: Adsorption vs concentration
- Longitudinal Dispersivity: 0.004 m

- Transverse Dispersivity: 0.003 m
- Decay Half-Life: 0 d
- Dry Density: 0 g/m³
- Activation Concentration: 1 g/m³

FFT 3 Solute

- Diffusion Function: P2 Add In Function
- Adsorption Function: Adsorption vs concentration
- Longitudinal Dispersivity: 0.004 m
- Transverse Dispersivity: 0.003 m
- Decay Half-Life: 0 d
- Dry Density: 0 g/m³
- Activation Concentration: 1 g/m³

FFT 4 Solute

- Diffusion Function: P2 Add In Function
- Adsorption Function: Adsorption vs concentration
- Longitudinal Dispersivity: 0.004 m
- Transverse Dispersivity: 0.003 m
- Decay Half-Life: 0 d
- Dry Density: 0 g/m³
- Activation Concentration: 1 g/m³

FFT 5 Solute

- Diffusion Function: P2 Add In Function
- Adsorption Function: Adsorption vs concentration
- Longitudinal Dispersivity: 0.004 m
- Transverse Dispersivity: 0.003 m
- Decay Half-Life: 0 d
- Dry Density: 0 g/m³
- Activation Concentration: 1 g/m³

Boundary Conditions

Bottom Cl

- Category: Contaminant
- Kind: Solute Concentration 1 g/m³

Top C

- Category: Contaminant
- Kind: Solute Concentration 0 g/m³

Contaminant Adsorption Functions

Adsorption vs concentration

- Model: Spline Data Point Function
- Function: Adsorption vs. Concentration
- Curve Fit to Data: 100 %
- Segment Curvature: 100 %
- Y-Intercept: 0 g/g
- Data Points: Concentration (g/m³), Adsorption (g/g)

Contaminant Diffusion Functions

Diffusion vs water content

- Model: Spline Data Point Function
- Function: Diffusion Coefficient vs. Volumetric Water Content
- Curve Fit to Data: 95 %
- Segment Curvature: 22 %
- Y-Intercept: 6.1999999e-05 m²/d
- Data Points: Volumetric Water Content, Diffusion Coefficient (m²/d)

P2 Add In Function

- Model: Add-In Function
- Function: TestInterpolateList
- Assembly: Interpolate Diffusion Coefficient
- Function: TestInterpolateList
- Field csvFileLocation: C:\Users\djf160\Documents\MSc\Transport Models\P2 Add In\P2Function.csv

P3SW CH₄ Normalized Transient Seepage

Report generated using GeoStudio 2018 R2. Copyright © 1991-2018 GEOSLOPE International Ltd.

Project Settings

- Unit System: International System of Units (SI)

Analysis Settings

- Transient Seepage
- Description: Establish upward pore water movement
- Kind: SEEP/W
- Parent: Steady-State Seepage
- Method: Transient

Physics

Water Transfer

- Free convection: thermal effects: No
- Free convection: solute effects: No
- Vapor transfer: isothermal: No
- Vapor transfer: thermal: No

Water Settings

- Initial PWP Conditions from: Parent Analysis
- Maximum Number of Iterations: 500
- Maximum Difference: 0.005
- Significant Digits: 2
- Max # of Reviews: 10

Under-Relaxation Criteria

- Initial Rate: 1

- Minimum Rate: 0.1
- Rate Reduction Factor: 0.65
- Reduction Frequency (iterations): 10
- Unit Weight of Water: 9.807 kN/m³
- Bulk Modulus of Pore-Fluid: 2,083,333.3 kPa

Settings

- Dimension: 1D
- Exclude cumulative values: No

Time

- Starting Time: 1 d
- Duration: 2,500 d
- # of Steps: 100
- Step Generation Method: Linear
- Time Increment: 25 d
- Save Steps Every: 3

Materials

FFT 1

- Hydraulic
- Model: Saturated Only
- Sat Kx: 1 m/d
- Ky'/Kx' Ratio: 1
- Rotation: 0 °
- Volumetric Water Content: 0.86
- Compressibility: 0 /kPa

Water

- Hydraulic
- Model: Saturated Only
- Sat Kx: 1 m/d
- Ky'/Kx' Ratio: 1
- Rotation: 0 °
- Volumetric Water Content: 1
- Compressibility: 0 /kPa

FFT 2

- Hydraulic
- Model: Saturated Only
- Sat Kx: 1 m/d
- Ky'/Kx' Ratio: 1
- Rotation: 0 °
- Volumetric Water Content: 0.85
- Compressibility: 0 /kPa

FFT 3

- Hydraulic
- Model: Saturated Only
- Sat Kx: 1 m/d
- Ky'/Kx' Ratio: 1
- Rotation: 0 °
- Volumetric Water Content: 0.84
- Compressibility: 0 /kPa

FFT 4

- Hydraulic
- Model: Saturated Only
- Sat Kx: 1 m/d
- K_y'/K_x' Ratio: 1
- Rotation: 0 °
- Volumetric Water Content: 0.83
- Compressibility: 0 /kPa

FFT 5

- Hydraulic
- Model: Saturated Only
- Sat Kx: 1 m/d
- K_y'/K_x' Ratio: 1
- Rotation: 0 °
- Volumetric Water Content: 0.82
- Compressibility: 0 /kPa

Boundary Conditions

Head at Top

- Category: Hydraulic
- Kind: Water Pressure Head 10 m

P3 Constant flow

- Category: Hydraulic
- Kind: Water Flux 0.00055 m/d
- Review: No

P3SW CH₄ Normalized CTRAN/WAnalysis

Report generated using GeoStudio 2018 R2. Copyright © 1991-2018 GEOSLOPE International Ltd.

Project Settings

- Unit System: International System of Units (SI)

Analysis Settings

- CTRAN/WAnalysis
- Description: Establish concentrations in tailings (and water)
- Kind: CTRAN/W
- Parent: Transient Seepage
- Method: Transient

Physics

Solute Transfer

- Advection-dispersion with water transfer: Yes

Water Settings

- Results from: Parent Analysis

Solute Settings

- Initial Concentrations from: (none)
- Maximum Number of Iterations: 25
- Maximum Difference: 1e-05
- Significant Digits: 2

Settings

- Dimension: 1D

- Exclude cumulative values: No

Time

- Starting Time: 0 d
- Duration: 2,500 d
- # of Steps: 100
- Step Generation Method: Linear
- Time Increment: 25 d
- Save Steps Every: 1
- Fixed Elapsed Times: 810; 1,180; 1,550; 2,280;

Materials

FFT 1 Solute

- Diffusion Function: Add-In Diff Coefficient
- Adsorption Function: Adsorption vs concentration
- Longitudinal Dispersivity: 0.004 m
- Transverse Dispersivity: 0.003 m
- Decay Half-Life: 0 d
- Dry Density: 0 g/m³
- Activation Concentration: 1 g/m³

Water Solute

- Diffusion Function: Diffusion in water
- Adsorption Function: Adsorption vs concentration
- Longitudinal Dispersivity: 1 m
- Transverse Dispersivity: 1 m
- Decay Half-Life: 0 d

- Dry Density: 0 g/m³
- Activation Concentration: 0 g/m³

FFT 2 Solute

- Diffusion Function: Add-In Diff Coefficient
- Adsorption Function: Adsorption vs concentration
- Longitudinal Dispersivity: 0.004 m
- Transverse Dispersivity: 0.003 m
- Decay Half-Life: 0 d
- Dry Density: 0 g/m³
- Activation Concentration: 1 g/m³

FFT 3 Solute

- Diffusion Function: Add-In Diff Coefficient
- Adsorption Function: Adsorption vs concentration
- Longitudinal Dispersivity: 0.004 m
- Transverse Dispersivity: 0.003 m
- Decay Half-Life: 0 d
- Dry Density: 0 g/m³
- Activation Concentration: 1 g/m³

FFT 4 Solute

- Diffusion Function: Add-In Diff Coefficient
- Adsorption Function: Adsorption vs concentration
- Longitudinal Dispersivity: 0.004 m
- Transverse Dispersivity: 0.003 m
- Decay Half-Life: 0 d

- Dry Density: 0 g/m³
- Activation Concentration: 1 g/m³

FFT 5 Solute

- Diffusion Function: Add-In Diff Coefficient
- Adsorption Function: Adsorption vs concentration
- Longitudinal Dispersivity: 0.004 m
- Transverse Dispersivity: 0.003 m
- Decay Half-Life: 0 d
- Dry Density: 0 g/m³
- Activation Concentration: 1 g/m³

Boundary Conditions

Bottom Cl

- Category: Contaminant
- Kind: Solute Concentration 1 g/m³

Top C

- Category: Contaminant
- Kind: Solute Concentration 0 g/m³

Coupled Anaerobic CH₄ Oxidation

- Category: Contaminant
- Kind: Solute Mass Flux -0.0005 g/d/m²

Contaminant Adsorption Functions

Adsorption vs concentration

- Model: Spline Data Point Function
- Function: Adsorption vs. Concentration

- Curve Fit to Data: 100 %
- Segment Curvature: 100 %
- Y-Intercept: 0 g/g
- Data Points: Concentration (g/m³), Adsorption (g/g)

Contaminant Diffusion Functions

Diffusion in water

- Model: Spline Data Point Function
- Function: Diffusion Coefficient vs. Volumetric Water Content
- Curve Fit to Data: 100 %
- Segment Curvature: 100 %
- Y-Intercept: 0.000125 m²/d
- Data Points: Volumetric Water Content, Diffusion Coefficient (m²/d)

Add-In Diff Coefficient

- Model: Add-In Function
- Function: TestInterpolateList
- Assembly: Interpolate Diffusion Coefficient
- Function: TestInterpolateList